Study of ^{208}Po Populated via β^{+}/EC Decay

Matthew Brunet

Supervisor: Zsolt Podolyák

Co-Supervisor: Daniel Doherty

Department of Physics,

University of Surrey

Guildford, GU2 7XH

October 2021

Abstract

Data collected during a decay spectroscopy experiment at the ISOLDE Decay Station (IDS) in 2016, were used to investigate the structure of ^{208}Po populated via the β^+/EC decay of ^{208}At. This decay, and resulting structure, was most recently studied in experiments which took place in the 1980s. Thus, the aim of this analysis was to take advantage of improvements in detector technology and radioactive beam production to establish an expanded level scheme below Q_{EC} = 4999(9) keV. From this work a total of 170 transitions and 58 states were observed, including 27 newly-observed states. Ninety-three of the transitions identified in this analysis differ from prior decay studies. These consist of 43 newly-observed transitions; 33 previously-observed ^{208}Po γ rays placed in the level scheme through this analysis; and 17 transitions moved from previous placements. Spin-parities were assigned through a combination of γ-ray placements, previously-measured α_K values, and restrictions resulting from β and γ decay selection rules. In addition, electron conversion coefficients were calculated for all transitions below 1 MeV, and $\log ft$ values were determined for all populated states using intensity imbalances. From this analysis, $\sim$46% of the decays were found to be first-forbidden, a significant increase from the $\sim$37% measured in the 1980s. It is suggested that the high first-forbidden proportion of ^{208}At and surrounding β^+/EC-decaying nuclei could provide a testing ground for models of first-forbidden decay. These can then be incorporated into larger β-decay studies in the region which lack relevant data points, such as models of r-process nucleosynthesis. In addition, a low-lying 3^- state at 1995 keV, which had been previously assigned (2^-,3^-), was identified. Through comparisons with shell model calculations and considering the underlying shell structure, it was concluded that the low energy of the state was the result of configuration mixing of an abundance of 3^- states. In particular, the strength of $f_{7/2}i_{13/2}$ contributions to the octupole from both proton particle and neutron hole excitations results in stronger mixing for

3^- states in ^{208}Po with dominant $f_{7/2}i_{13/2}$ configurations. Strong octupole collectivity in the region, and observed, low-energy, core-excited states in neighbouring nuclei suggest collective character for the 1995 keV state. Although no evidence of this was found in this analysis, it is anticipated that a high statistics Coulex experiment could provide further detail into the nature of the 1995 keV state.

Acknowledgements

I would like to start by thanking the Surrey Physics Department for giving me the opportunity to pursue my doctorate. I am also grateful to STFC for supporting my research, including my long-term attachment at GSI, which proved to be an unparalleled learning experience both academically and socially.

As part of my doctorate I've collaborated with researchers from institutions around the world, each providing their own knowledge and guidance to my research. In particular I would like to thank my co-supervisor Dan Doherty and the members of the Surrey nuclear physics department for their unwavering support and for providing multiple opportunities to take part in their experiments and social gatherings. I'd also like to give a special mention Phil Walker for being one of the kindest people I know, who's help and patience helped me settle in to life as a researcher. I'm grateful to the whole of the DESPEC group at GSI, specifically Magda Górska and Jürgen Gerl, who gave me the freedom and encouragement to excel on my placement. Lastly, to everyone who's been part of my academic journey, from a night shift on an experiment that's gone wrong, to a celebratory drink after an experiment gone right, thank you.

My PhD colleagues, past and present, have been an endless source of support both socially and (occasionally) academically. So, to Tom and Callum for teaching me everything I now know about football (and some physics too); to Andrew for all our meaningless and meaningful conversations; to Jess and Vicky for being the greatest housemates I could've asked for and my dearest friends; and to everyone I've shared a slightly too long coffee break with, you're all incredible people and I'm glad you've been, and are, a part of my life.

Most importantly, I'd like to thank my supervisor Zsolt Podolyák who's knowledge, patience, support, and confidence in me have been invaluable.

Lastly, I'd like to thank my family and my boyfriend for their unwavering love and support.

Contents

Abstract **i**

Acknowledgements **iii**

1 Introduction **1**

2 Theory **4**
- 2.1 Nuclear Structure 4
  - 2.1.1 The Shell Model 5
  - 2.1.2 Configuration Mixing 10
  - 2.1.3 The Collective Model 13
  - 2.1.4 Structure of ^{208}Po 18
- 2.2 Nuclear Decay 18
  - 2.2.1 Gamma Decay 18
  - 2.2.2 β^- Decay 22
  - 2.2.3 β^+ Decay 23
- 2.3 Radiation Detection 30
  - 2.3.1 Germanium Detectors 30
  - 2.3.2 Interactions of γ rays with Matter 32
  - 2.3.3 β Decay Detection 34

3 Scientific Motivation **36**
- 3.1 The Near ^{208}Pb Mass Region 36
  - 3.1.1 Octupole Collectivity 36
  - 3.1.2 Competition Between Allowed and First-forbidden β Decay 39
  - 3.1.3 Other Features of Interest in ^{208}Po 41

4 Experimental Details **42**
- 4.1 ISOLDE 42
  - 4.1.1 Beam Production 43
  - 4.1.2 Production of ^{208}Po 45
- 4.2 The ISOLDE Decay Station 46
  - 4.2.1 Resident IDS Germanium Detectors 46
  - 4.2.2 Auxiliary Detectors 47
  - 4.2.3 Electronics and Data Collection 48

5 Analysis and Results **49**
- 5.1 Data Sorting 49
- 5.2 Data Calibrations 50
  - 5.2.1 Energy Calibration 50

5.2.2 Efficiency Calibration 50
5.3 Dataset 51
5.3.1 Statistics 51
5.3.2 Contaminants 52
5.3.3 Electron Conversion Coefficients 53
5.4 ^{208}Po Level Scheme 54
5.5 Establishing States and Transitions 65
5.5.1 Confirmed States 65
5.5.2 The 2223 keV State 67
5.5.3 The 2438 keV State 72
5.5.4 The 3276 keV State 74
5.6 1995 keV State Spin-Parity Determination 76
5.7 Unplaced Transitions From Prior Analysis 79
5.8 Measurement of Isomer Half-life 81

6 Discussion **85**
6.1 Shell Model Calculations 85
6.1.1 Shell Model Calculations (82<Z<114, 100<N<126) 85
6.1.2 Shell Model Calculations (82<Z,N<126) 87
6.1.3 logft Comparison 91
6.1.4 Unresolved logft Values 92
6.2 Beta Decay States 93
6.2.1 The Pandemonium Effect 94
6.2.2 Proportion of First-Forbidden Decays 96
6.2.3 Implications for r-process Nucleosynthesis 100
6.3 $\mathbf{3^-}$ State Implications 100
6.3.1 Octupole Collectivity 108

7 Conclusion **110**

Appendices **116**

A ^{208}Po Transitions Table **116**

B Table of Branching Ratios **121**

C List of Publications & Conference Talks **123**

Chapter 1

Introduction

The structure of the atomic nucleus has been a subject of rigorous study since its discovery just over a century ago. Over time the understanding of nuclear structure has grown considerably, but despite this many open questions remain. The constituent elements of the nucleus are well understood, comprised of varying numbers of protons and neutrons interacting via fundamental forces, however the complexity of the system increases with the number of interacting bodies. Simulating nuclear structure is computationally intensive and implausible for the vast majority of nuclei. Consequently, experimental observations are crucial for expanding knowledge in this field, as they provide data upon which theoretical models can be fitted, tested, and refined.

One theoretical model that has been highly successful in describing nuclear behaviour is the shell model [1]. Significant simplification is achieved through reducing the model space by placing the majority of nucleons into non-interacting, closed shells, thus minimising the number of interacting bodies. As a consequence however, its accuracy rapidly deteriorates as the number of nucleons outside of these shells increases. As shown in Figure 1.1 ^{208}Po lies close to the doubly-closed shell nucleus of ^{208}Pb, and can therefore be well described by shell-model calculations.

The region around ^{208}Po is also notable for the presence of highly collective octupole phonon

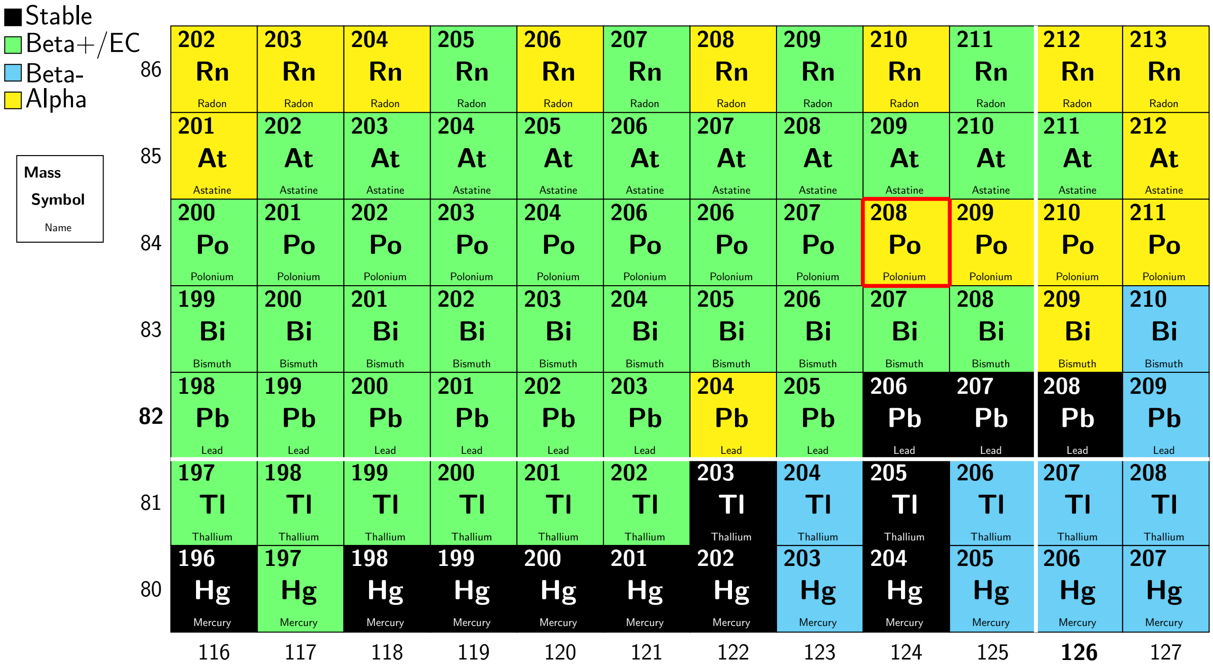

■ Stable
🟩 Beta+/EC
🟦 Beta-
🟨 Alpha

Mass
Symbol
Name

	116	117	118	119	120	121	122	123	124	125	**126**	127
86	🟨 202 Rn Radon	🟨 203 Rn Radon	🟨 204 Rn Radon	🟩 205 Rn Radon	🟨 206 Rn Radon	🟩 207 Rn Radon	🟨 208 Rn Radon	🟩 209 Rn Radon	🟨 210 Rn Radon	🟩 211 Rn Radon	🟨 212 Rn Radon	🟨 213 Rn Radon
85	🟨 201 At Astatine	🟩 202 At Astatine	🟩 203 At Astatine	🟩 204 At Astatine	🟩 205 At Astatine	🟩 206 At Astatine	🟩 207 At Astatine	🟩 208 At Astatine	🟩 209 At Astatine	🟩 210 At Astatine	🟩 211 At Astatine	🟨 212 At Astatine
84	🟩 200 Po Polonium	🟩 201 Po Polonium	🟩 202 Po Polonium	🟩 203 Po Polonium	🟩 204 Po Polonium	🟩 206 Po Polonium	🟩 206 Po Polonium	🟩 207 Po Polonium	🟨 208 Po Polonium	🟨 209 Po Polonium	🟨 210 Po Polonium	🟨 211 Po Polonium
83	🟩 199 Bi Bismuth	🟩 200 Bi Bismuth	🟩 201 Bi Bismuth	🟩 202 Bi Bismuth	🟩 203 Bi Bismuth	🟩 204 Bi Bismuth	🟩 205 Bi Bismuth	🟩 206 Bi Bismuth	🟩 207 Bi Bismuth	🟩 208 Bi Bismuth	🟨 209 Bi Bismuth	🟦 210 Bi Bismuth
82	🟩 198 Pb Lead	🟩 199 Pb Lead	🟩 200 Pb Lead	🟩 201 Pb Lead	🟩 202 Pb Lead	🟩 203 Pb Lead	🟨 204 Pb Lead	🟩 205 Pb Lead	■ 206 Pb Lead	■ 207 Pb Lead	■ 208 Pb Lead	🟦 209 Pb Lead
81	🟩 197 Tl Thallium	🟩 198 Tl Thallium	🟩 199 Tl Thallium	🟩 200 Tl Thallium	🟩 201 Tl Thallium	🟩 202 Tl Thallium	■ 203 Tl Thallium	🟦 204 Tl Thallium	■ 205 Tl Thallium	🟦 206 Tl Thallium	🟦 207 Tl Thallium	🟦 208 Tl Thallium
80	■ 196 Hg Mercury	🟩 197 Hg Mercury	■ 198 Hg Mercury	■ 199 Hg Mercury	■ 200 Hg Mercury	■ 201 Hg Mercury	■ 202 Hg Mercury	🟦 203 Hg Mercury	■ 204 Hg Mercury	🟦 205 Hg Mercury	🟦 206 Hg Mercury	🟦 207 Hg Mercury

Figure 1.1: Section of the nuclear Segrè chart with primary decay modes given. The Z=82 and N=126 magic numbers are highlighted along with the position of ^{208}Po.

excitations [2], most notably in the first excited state of ^{208}Pb [3]. Such states are of particular interest to nuclear structure as efforts to reproduce them in theoretical calculations have had limited success. Although no such behaviour has been observed in ^{208}Po during prior studies, its proximity to other collective nuclei would strongly suggest the presence of as yet unobserved collective states.

The work presented in this thesis analyses data taken at the ISOLDE Decay Station (IDS) at the CERN-ISOLDE facility using γ-ray spectroscopy. The aim being to broaden understanding of the underlying structure of the two-proton-particle, two-neutron-hole nucleus of ^{208}Po populated via the β^+/EC decay of ^{208}At. These data also allow for investigation into the decay of ^{208}At. Specifically, the proportion of decays which proceed via paths with higher degrees of forbiddenness, a phenomenon which is prevalent for decays in this mass region. As explored in Section 3.1.2, this proportion can have significant implications for r-process nucleosynthesis calculations, and understanding of β decays more generally. Lastly, as previously mentioned, ^{208}Po lies in a region notable for high octupole collectivity. As such, these data allows for the exploration of both shell and collective structures, something which no current single theory can replicate. The decay of ^{208}At was most recently studied in the early 1980s [4, 5], Thus, given the technological improvements over the past four decades, this analysis offers the opportunity to significantly broaden understanding of both ^{208}Po and the β^{+}/EC decay itself.

From this investigation an expanded level scheme for ^{208}Po was established using $\gamma - \gamma$ coincidences. Electron conversion coefficients were calculated for all low energy ($E_{\gamma} < 1$ MeV) γ rays. Where possible, spin parities and $\log ft$ values were determined using known information regarding the transitions from each level. The structure and branching ratios were compared with shell model calculations to further understanding of the composition of certain states.

Chapter 2

Theory

2.1 Nuclear Structure

Accurate models are an invaluable resource for research as they allow predictions to be made regarding the behaviour of a given system and thus can both direct and inform analysis. For nuclear physics, models can predict the existence of energy levels as well as if and how a given nucleus would decay. Nuclei consist of many interacting nucleons which, though their individual interactions are well described, the number of bodies involved presents difficulties for computational modelling. Consequently the modelling of nuclear structure depends heavily on experimental observations, and as such is significantly limited, particularly for heavy, complex isotopes. The physical behaviour of nuclei is heavily dependent on the type of nucleus being described. As a result of this variance, a unified model has yet to be developed and instead nuclear physics relies on two types of simplified models: the shell model and the collective model, as a basis to describe different regions of the nuclide chart. These models have produced reliable predictions when applied to given mass regions and both are relevant to the study of ^{208}Po, thus they are outlined in greater details in the following sections.

2.1.1 The Shell Model

The shell model was first proposed in 1932 by Ivanenko and Gapon [6, 7], and since then it has undergone a series of adaptations and refinements, in particular by Goeppert-Mayer in 1950 [1, 8, 9], to become the nuclear model used today. The central concept of the shell model approach utilises the Pauli exclusion principle to place the protons and neutrons into discrete shells described by given quantum numbers [10], and in this regard it bears similarities to electron shells in atomic physics [11]. One of many key differences however is that unlike electron shells, nuclei contain two different particles; protons and neutrons, both of which are described by different quantum numbers. Consequently both protons and neutrons are described by distinct shell structures as opposed to a single unified structure for both.

The advantage of this approach is that by consolidating large numbers of protons and neutrons into non-interacting, filled shells the remaining nucleons can be treated as interacting with one another in a central potential generated by the nucleus. This drastically simplifies the problem by reducing the number of interacting bodies, however as the number of nucleons outside these non-interacting shells (valence nucleons) increases, the simplification breaks down and becomes less predictive.

Nuclei, like most physical systems, will gravitate towards the most stable structure. As such, by facilitating a nucleus to change its structure by adding or removing nucleons the energy needed to do this can be viewed as a measure of stability. Given this approach, the following are two values which can be used to quantify nuclear stability: nucleon capture cross section and nucleon-pair separation energy. Nucleon pairs are used to avoid pairing effects [12] between nucleons obscuring trends in stability. Figure 2.1 shows how nucleon-pair separation energy varies with increasing neutron number, for various isotopes and isotones. From this graph we can observe multiple proton and neutron numbers with high separation energies, corresponding to greater stability. These numbers (2, 8, 20, 28, 50, and 126) are referred to as the "magic numbers"[13].

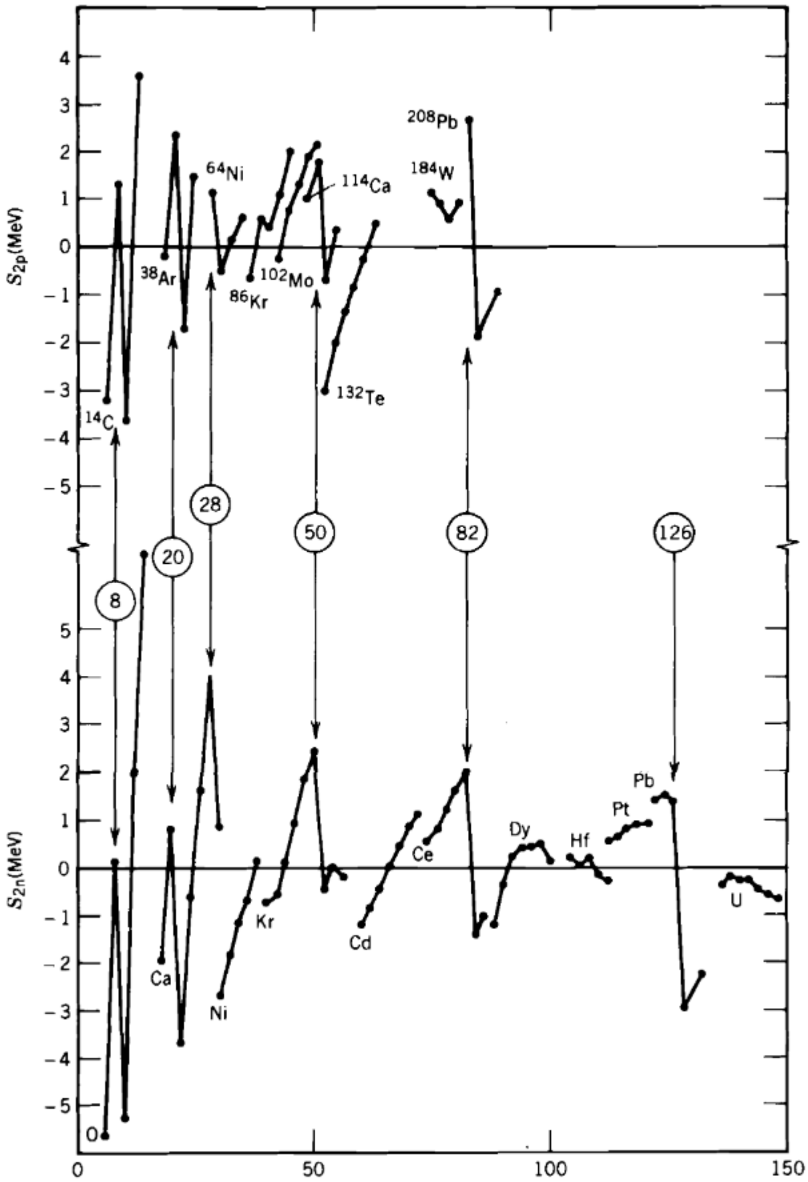

Figure 2.1: The discrepancy between experimental 2-proton and 2-neutron separation energies, and their theoretical values calculated with the semi-empirical mass formula. The top graph shows proton-pair separation energy varies for sequences of isotones. The lower graph displays the same information for neutrons and sequences of isotopes [14]. Neutron number is given on the x-axis for both graphs.

Additional evidence for the existence of these values includes the prevalence of stable isotopes/isotones for nuclei with magic proton/neutron numbers. This further signifies a greater stability as the proton to neutron ratio is able to deviate further before becoming unstable. Furthermore, nuclei with proton/neutron numbers close to magic numbers exhibit larger nucleon capture cross-sections than their neighbouring nuclei. The first model to adequately explain this phenomenon was the shell model where the abnormal stability is attributed to shell closures.

Shell Model Potential

The two main components of the shell model are the central and spin-orbit potentials. While the parameters that describe the individual nucleons are well established, one of the most common approximations for the mean-field is the Woods-Saxon potential.

The Woods-Saxon Potential

When considering a nucleus with a varying number of nucleons, and hence of varying size, the potential of that system should be at least partly dependent on those factors. The Woods-Saxon potential [15], given in equation 2.1 and shown in Figure 2.2, describes the potential in terms of the mean nuclear radius ($R = r_0 A^{\frac{1}{3}}$),

$$V(r) = \frac{-V_0}{1 + \exp(\frac{r-R}{a})} \tag{2.1}$$

where V_0 is the depth of the potential, R is the mean nuclear radius, r is the radial distance inside the potential, and a is the surface diffuseness parameter that dictates the surface thickness of the nucleus.

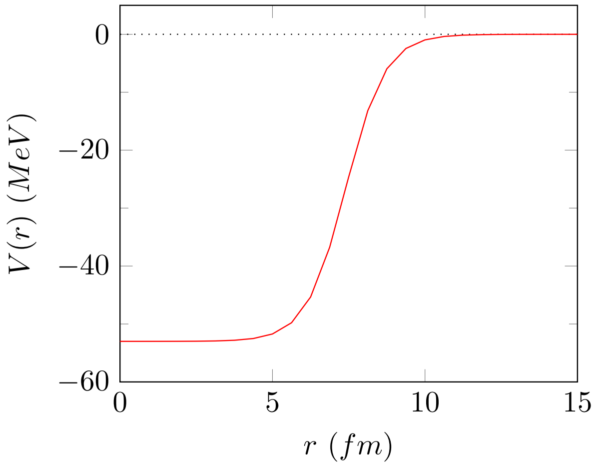

Figure 2.2: The Woods-Saxon potential for an A=208 nucleus with V_0 =53 MeV and a=0.65 fm.

Any given solution for the shell model potential can be verified by determining whether the magic numbers arise from it. In this respect the Woods-Saxon potential produces the expected spacing for the first three magic numbers (2, 8, and 20), as shown on the left of Figure 2.3, but at higher energies predicts energy gaps which are not observed experimentally. The Woods-Saxon potential features a flat, inner potential and sharp drop-off at the surface which recreates the effects of the homogenous density of the nucleus and short-range strong force of the nucleons respectively. In addition, the core assumption of the potential (being based on the size of the nucleus) remains justified, but it requires additional factors and considerations in order to recreate the full set of magic numbers observed experimentally. For this the effect of the spin-orbit interaction must be considered.

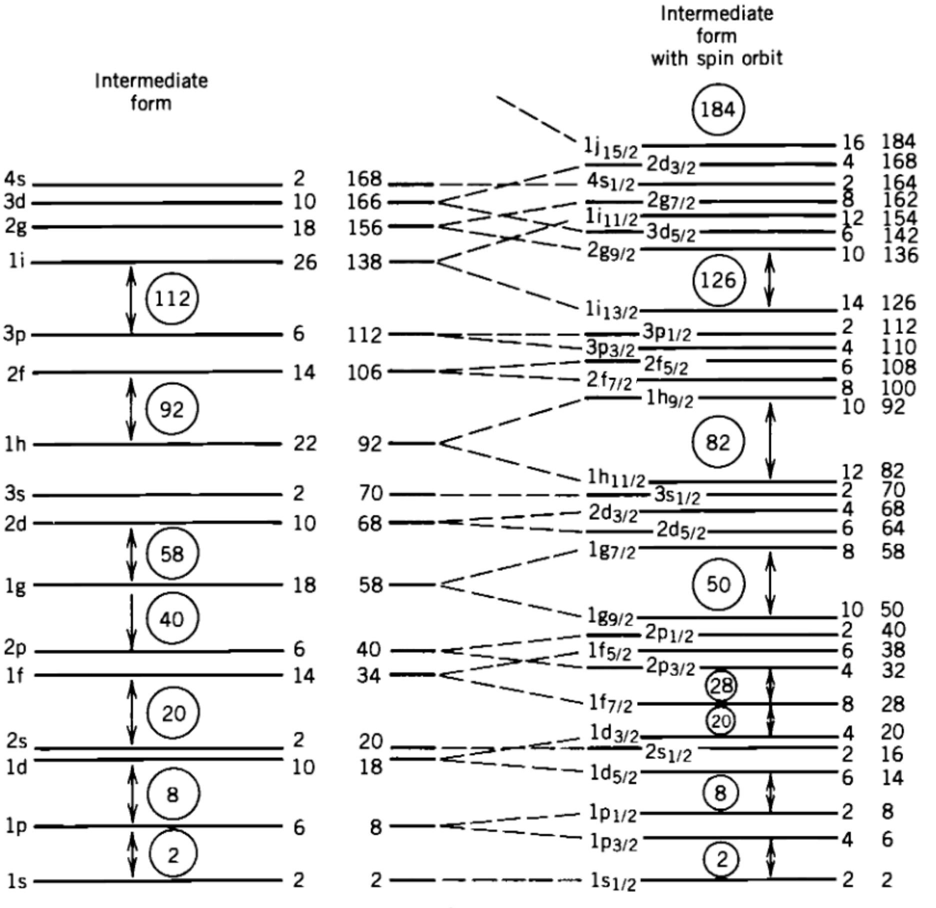

Figure 2.3: The energy levels generated with the Woods-Saxon potential are shown on the left. The right-hand side shows the energy levels calculated with a potential that considers spin-orbit coupling [14].

The Spin-Orbit Potential

Proton and neutron orbitals have quantised orbital angular momentum described by the orbital angular momentum quantum number $\boldsymbol{l}$, as well as a spin angular momentum of $\pm\frac{1}{2}$. The orbital angular momentum quantum number dictates the number of degenerate magnetic substates ($\boldsymbol{m_l}$) contained within a level, given by $2\boldsymbol{l}$ + 1. Each of these substates also has two possible spin states $+\frac{1}{2}$ and $-\frac{1}{2}$, making the total degeneracy of a given energy level $2(2\boldsymbol{l}$ + 1).

The spin-orbit potential accounts for the interaction between a nucleon's orbital angular momentum and its spin angular momentum. The effect of this is a reduction in the energy of the state when the spin acts in parallel to the orbit, and an increase when the values oppose each other, resulting in energy level splitting. The energy difference caused by this effect is dependent on $\boldsymbol{l}$ as shown in equation 2.2.

$$\Delta E \propto \frac{1}{2}(2\boldsymbol{l}+1)\hbar^2 \tag{2.2}$$

Energy splitting increases as $\boldsymbol{l}$ increases, resulting in more significant effects for $\boldsymbol{l} > 2$. As shown in Figure 2.3, this level splitting results in energy gaps which exactly correspond to the magic numbers observed experimentally.

Incorporating spin-orbit coupling into the Woods-Saxon potential, despite reproducing the magic numbers, remains a relatively rudimentary description of shell model potentials. Work continues in this field to optimise parameters and replicate experimental observations by incorporating factors such as nuclear deformation [16] into the potential.

Due to this combination of angular momentum terms the split energy levels are denoted by three values; n which is the radial quantum number, the orbital angular momentum quantum number l in spectroscopic notation (s, p, d, f, g... etc. for 0, 1, 2, 3, 4... etc.), and a total angular momentum quantum number, $\boldsymbol{j}$. The total angular momentum, $\boldsymbol{j}$, is calculated as the modular sum of the angular momentum variables, $\boldsymbol{j} = |\boldsymbol{l} + s|$, or more simply, as s, the spin quantum number, can only be $\pm\frac{1}{2}$, $\boldsymbol{j} = \boldsymbol{l} \pm \frac{1}{2}$.

The total angular momentum quantum number is a useful quantity for determining certain properties of a given energy level. The degeneracy of an energy level (and thus the number of like nucleons that can occupy it) is given by ($2\boldsymbol{j} + 1$). It is also important to note that paired nuclei will predominantly have opposing values of $\boldsymbol{m_j}$ resulting in no overall spin. As a result of this phenomenon the total angular momentum of a nucleus only needs to consider unpaired nucleons. Parity of a given state is determined by $\boldsymbol{l}$, where parity is given by $\pi = (-1)^{\boldsymbol{l}}$. All these quantum numbers are presented in the form $\boldsymbol{l_j}$ for shell model orbitals (e.g $s_{1/2}$, $p_{3/2}$, and $h_{9/2}$) and as J^π for nuclear states (e.g $0^+, 5^-, 8^+$).

Comprising solely of single particles interacting with each other within a mean-field potential, the shell model is extremely effective at describing nuclei that closely resemble this rudimentary approximation, such as nuclei adjacent to closed shell structures. However this accuracy deteriorates rapidly as more valence nucleons are added and nucleon-nucleon interactions can no longer be considered negligible. In order to more accurately model nuclear structures that deviate further from closed shell structures it is crucial to further explore the internal interactions of the nucleons.

2.1.2 Configuration Mixing

Nuclear states rarely result from the contribution of a single configuration or wavefunction as inside a nucleus states are not independent of one another. Instead, most states arise from the linear combination of multiple configurations of the same spin-parity. Interactions between these states govern the extent to which configurations are mixed [12].

To explore this phenomenon further the following discusses configuration mixing for a pair of initially unperturbed states, with energies E_1 and E_2 where $E_1 > E_2$ and V is the interaction energy between the two states. The Hamiltonian of this system would be,

$$H = \begin{pmatrix} E_1 & V_{12} \\ V_{12} & E_2 \end{pmatrix} \tag{2.3}$$

The eigenstates for this system (Φ_1 and Φ_2) are described in equations 2.4 and 2.5 respectively,

$$\Phi_1 \; = \; \alpha\phi_1 \; + \; \beta\phi_2 \tag{2.4}$$

$$\Phi_2 \; = \; -\beta\phi_1 \; + \; \alpha\phi_2 \tag{2.5}$$

$$\epsilon_{12} = \bar{E} \pm \sqrt{\Delta E^2 + V_{12}^2} \tag{2.6}$$

where $\bar{E} = \frac{E_1+E_2}{2}$ and $\Delta E = \frac{E_1-E_2}{2}$. This system is shown in Figure 2.4.

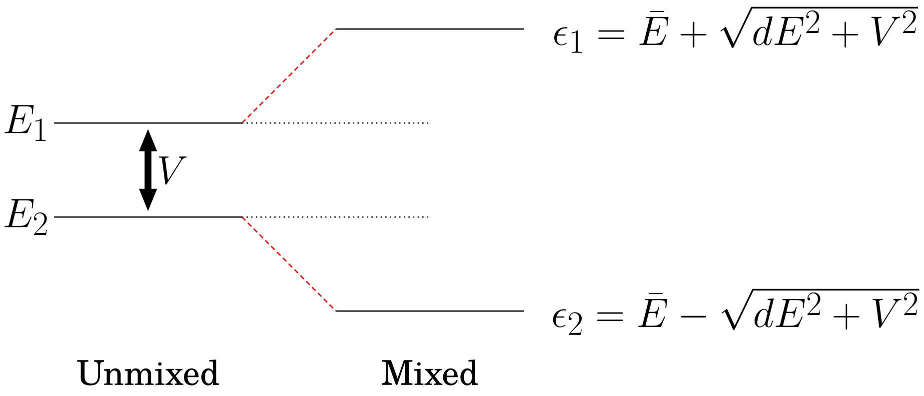

Figure 2.4: Energy shift due to two-state configuration mixing with unmixed stateson the left, and mixed, shifted states on the right. The equations for the eigenenergies of each state are given.

Configuration mixing can also occur between more than two states, extending the matrix equation for n states gives the following:

$$H = \begin{pmatrix} E_1 & V_{12} & & \\ V_{12} & E_2 & & \\ & & \dots & \\ & & & E_n \end{pmatrix} \tag{2.7}$$

In this instance the wave functions of the final states (Φ) are linear combinations of the individual configurations (ϕ_i). In multistate mixing the lowest-energy state undergoes the largest shift in energy while the remaining states only experience a small increase from their unperturbed energies. This phenomenon is shown graphically in Figure 2.5.

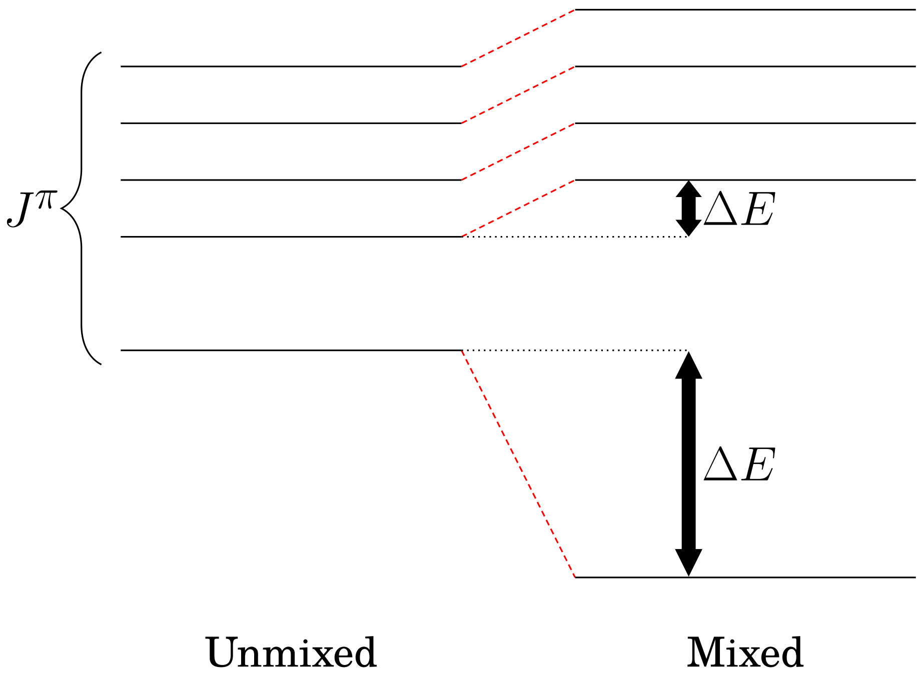

Figure 2.5: Energy shift due to multistate configuration mixing with unmixed states with shared spin-parity J^π on the left, and mixed, shifted states on the right.

A large number of states with the same spin-parity will result in a low-lying state with wave function contributions from each of the individual states. The collective shift upwards of the higher energy states is comparatively smaller.

Configuration mixing is the method by which low-lying states in nuclei with few valence nucleons are explained using shell orbitals. For some nuclei however, these states can also be described as an excitation of the nucleus as a whole, known as a collective excitation. This behaviour is thought to be the origin of the low-lying octupole vibrational states in the A=208 region, and is therefore important for both this work and understanding collective structure more generally.

2.1.3 The Collective Model

For high-mass even-even nuclei all the nucleons are paired, therefore shell model excited states in these nuclei would require the breaking of a nucleon pair to move a single nucleon to a higher energy level. The energy required to break nucleon pairs is ∼2 MeV [17] and hence, according to the shell model, the lowest excited states of these nuclei should be of the order of a few MeV. However this is not observed experimentally, with only a handful of exceptions every even-Z, even-N nucleus features a 2^+ excited state significantly below 2 MeV. This phenomenon, as well as anomalously low-lying states in other nuclei are instead described using collective excitations.

Vibrational States

For many high mass nuclei, certain excited states cannot be attributed to a single nucleon transferring to a higher energy level as the angular momenta and energy of these states do not support this. Instead, the nucleus acts as a single fluid mass and begins to oscillate akin to a water droplet. These vibrational states have a given energy associated with them, and are able to account for a number of the excited states of many nuclei. Figure 2.6 shows the first four vibrational modes along with their λ values which denote the order of the vibration.

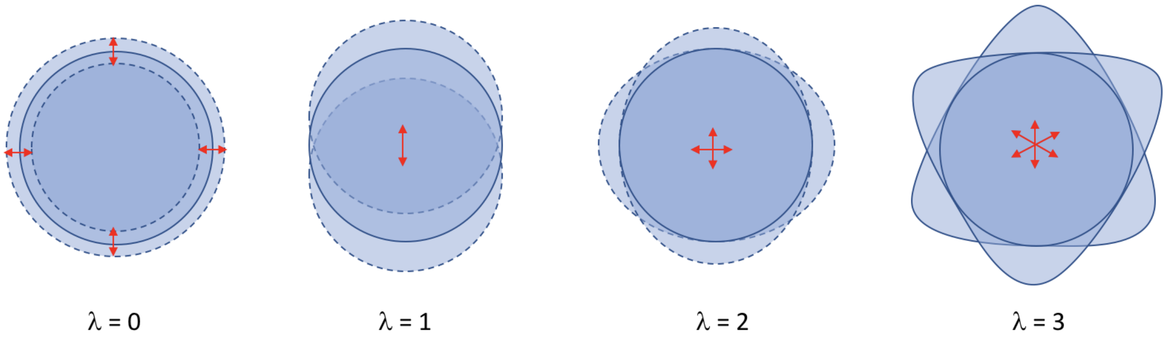

Figure 2.6: Diagrams showing monopole, dipole, quadrupole and octupole vibrational modes, (the red arrows show the direction of the vibrations)

The angular momentum, λ, also dictates the spin of the resulting vibrational state, with parity given by $(-1)^{\lambda}$. The energies of vibrational states are described using phonons, where a phonon is a quantum of vibrational energy, thus a single unit of a $\lambda = 2$ vibration is a quadrupole phonon. It is important to note that in Figure 2.6 the $\lambda = 1$ has a net translation of the centre of mass of the nucleus, and thus cannot be the result of internal interactions and is instead described as an collective electric dipole excitation.

Vibrational states are an example of collective behaviour which is most prevalent in high mass nuclei as well as nuclei with a large number of valence nucleons. The most notable example of a vibrational state is the first excited state of ^{208}Pb at 2614.5 keV [3] which is the result of a collective octupole vibration.

Rotational States

Rotational states describe the rotation of a nucleus which, like vibrational states, are a form of collective excitation. Rotational states only occur in nuclei with high numbers of valence nucleons as these have sufficient deformation for a rotational mode to result in a change in charge distribution, and hence an energy state. For nuclei with such a deformation, rotational states are able to provide low-energy excitation levels.

In classical mechanics, the kinetic energy of a rigid rotating object is $\frac{1}{2}\mathcal{J}\omega^2$, where $\mathcal{J}$ is the moment of inertia. Using these parameters the angular momentum is $L = \mathcal{J}\omega$, which gives the following equation for the rotational energy of a given state:

$$\Delta E_{rot} = \frac{\hbar^2}{2\mathcal{J}} I(I+1) \tag{2.8}$$

From this the energy ratios between two rotational states can be inferred, for example $E(4^+)/E(2^+)$ would be $\frac{20}{6}$ or 3.33. Though equation 2.8 is rudimentary, this ratio is remarkably consistent amongst heavy deformed nuclei, as shown in Figure 2.7.

This calculation of rotational state energy is not perfect however, as there are discrepancies between it and the energies observed experimentally. These discrepancies are minimal however and, as demonstrated, the ratios for rotational energy states have very good agreement for

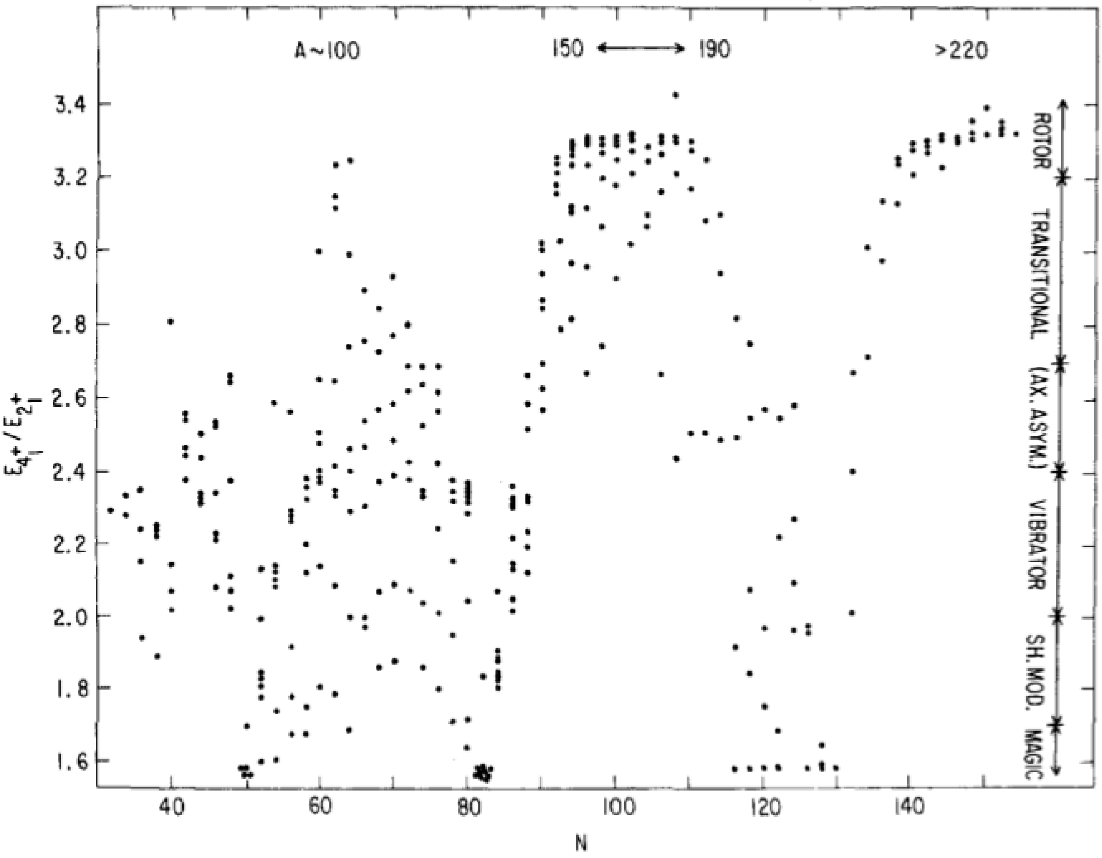

Figure 2.7: Ratio between the lowest 4+ and 2+ states for even-Z, even-N nuclei [12].

heavily deformed nuclei. The error is most likely the result of equation 2.8 assuming the nucleus to be a rigid object, when in reality it most likely exhibits characteristics akin to a rotating fluid with a varying moment of inertia.

Deformed nuclei also present difficulties for the shell model, as any deformation would have an effect on the mean-field potential of that nucleus. As the shell model assumes the potential to be spherical, a correction must be made to account for this. One of the most successful corrections is that of the deformed shell or Nilsson model.

The Nilsson Model

In 1955 S.G. Nilsson was the first person to solve the Schrödinger equation for a deformed potential [18], and thus determine the wave function for deformed states. The model uses a deformation parameter β, shown in equation 2.9 [14],

$$\beta = \frac{4}{3}\sqrt{\frac{\pi}{5}}\frac{\Delta R}{R_{av}} \tag{2.9}$$

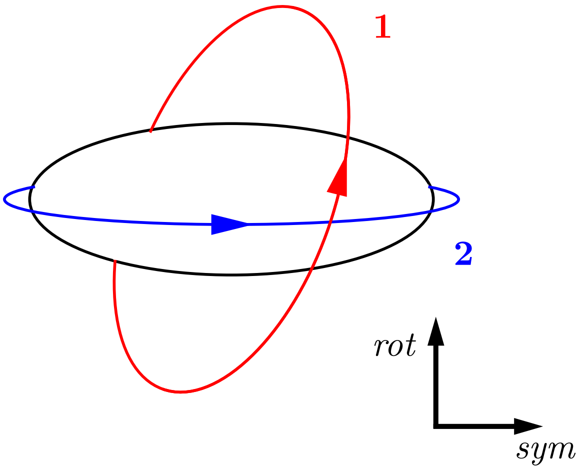

Figure 2.8: A graphical representation of an oblate nucleus with two orbitals with the same *j* component. Orbital 1 in red and orbital 2 in blue represent low and high Ω (*j* projection along the symmetry axis shown above) components for orbitals respectively.

to describe the shape of the nucleus and thus the shape of the potential.

A perfectly spherical nucleus has a deformation parameter of zero; as β increases the nucleus becomes elongated and more prolate; and as β decreases below zero, the nucleus squashes to form an oblate shape. For a deformed nucleus with a deformed potential the energy of a particle in a given state is now dependent not only on the angular momentum of that state, but its projection along the symmetry axis (Ω). This is due to certain orbits lying closer to the nuclear matter for more of their orbit as shown in Figure 2.8; this results in degenerate states for a given level no longer being equivalent in energy and thus must be referred to individually. Prolate deformations will cause the energies of states with a lower component of Ω to decrease as they will interact more with the nucleus, whereas oblate nuclei will produce the same effect for higher Ω components. The red and blue paths in Figure 2.8 demonstrate low and high j orbitals around an oblate nucleus. If these energy levels were solely dependent on the deformation parameter, each level would be a straight line with a gradient dependent on their orientation to the deformed nucleus; this however is not the case as this would allow levels with the same quantum numbers to occupy the same energy level. Instead levels with the same quantum numbers will repel each other, generating the curves visible in Figure 2.9 below.

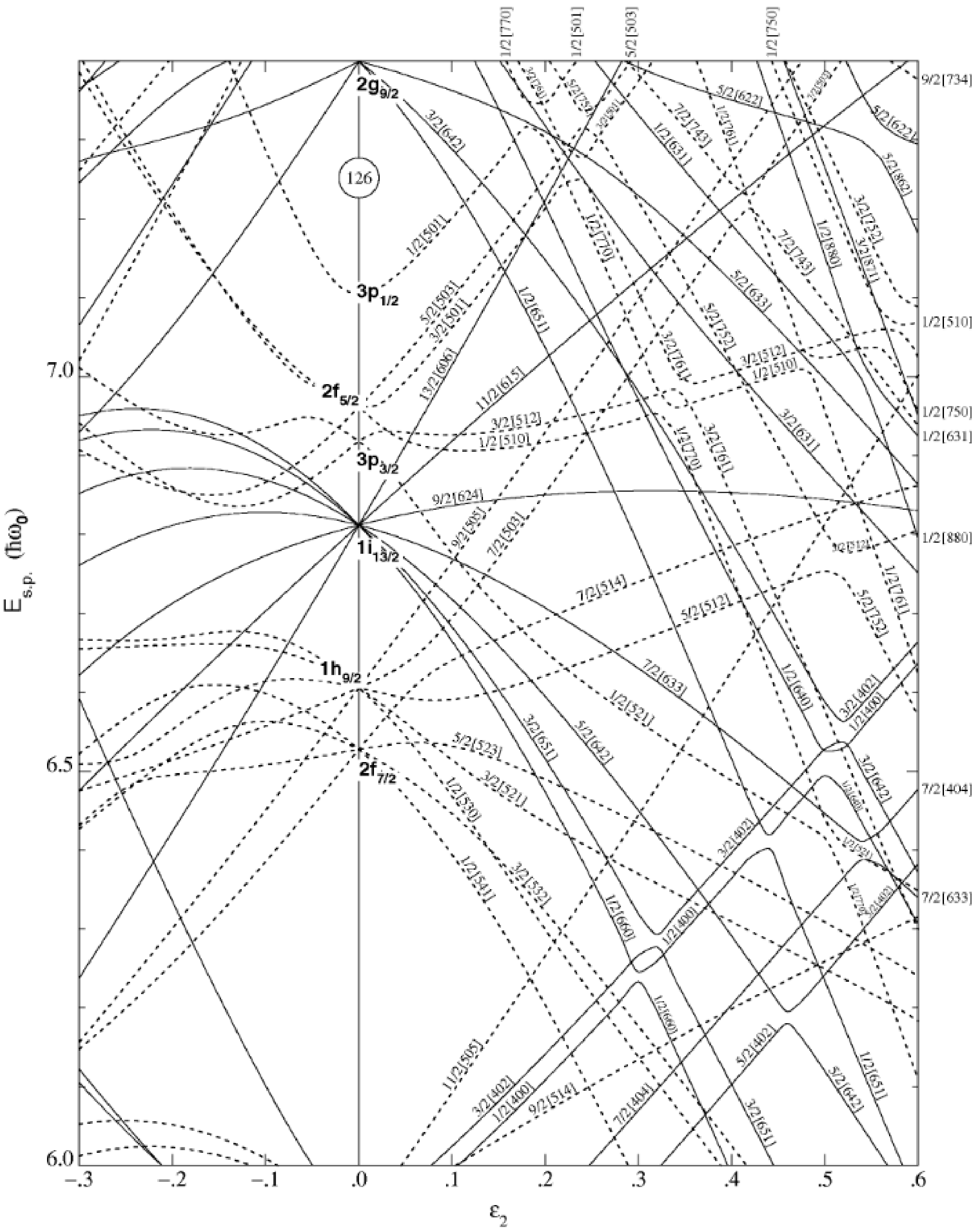

Figure 2.9: Nilsson diagram for neutrons $82 < N < 120$ [19].

The Nilsson model was constructed to determine single particle states for deformed nuclei, and is very accurate for these configurations.

2.1.4 Structure of ^{208}Po

Polonium-208 nuclei consist of 84 protons (two valence proton particles), and 124 neutrons (two valence neutron holes), and thus is considered a near-magic nucleus. Consequently ^{208}Po exhibits little to no deformation and as such its collectivity is limited to vibrational states. As mentioned previously, ^{208}Pb exhibits strong octupole collectivity, and the same is true for other nuclei in the same mass region as such states are the result of the collective behaviour of multiple $\Delta l = \Delta j = 3$ excitations across shell gaps (explored in Section 3.1.1). Consequently, understanding vibrational states, in particular octupole states, could be crucial to understanding low-lying states in ^{208}Po. In addition to this, four valence nucleons allows for a large number of particle states, however given the density of states possible with this number of valence nuclei, factors such as configuration mixing are also key considerations.

2.2 Nuclear Decay

Essential to the understanding of nuclear states and nuclear structure as a whole, is understanding how nuclei transition both internally between excited states and when changing proton and/or neutron number. Nuclear levels exist at different energies and thus interactions must take place such that energy, as well as spin and parity, are conserved in the system. When nuclei transition to lower energy systems this energy is released in some form to the surroundings. Measurement of these decay emissions can provide insight into the structures that produced them.

2.2.1 Gamma Decay

Transitions between energy states of the same nucleus only require an exchange of energy, thus when nuclei decay or de-excite to lower energy states this energy is emitted in the form of γ-ray photons.

Internal Electron Conversion

An excited state inside a nucleus also has the potential to decay via internal conversion, which is a process which competes directly with γ emission. In internal conversion, the nuclear field interacts with an atomic electron and expels it with kinetic energy equal to the transition energy minus the separation energy. This process is followed by the emission of an X-ray as a higher energy electron fills the empty orbital.

The extent to which a decay occurs via internal conversion is dictated by both the energy and multipolarity of the transition. As the effect also scales with proton number, for ^{208}Po it is important to account for this reduction in order to gain a full understanding of decay branches within the nucleus. This is achieved through an internal conversion coefficient, given by $\alpha = I_e/I_\gamma$. Equations 2.10 and 2.11 give estimates for the conversion coefficient for electric and magnetic transitions of order L,

$$\alpha(EL) \approxeq \frac{Z^3}{n^3}\frac{L}{L+1}\alpha_{fs}^4\left(\frac{2m_ec^2}{E}\right)^{L+5/2} \tag{2.10}$$

$$\alpha(ML) \approxeq \frac{Z^3}{n^3}\alpha_{fs}^4\left(\frac{2m_ec^2}{E}\right)^{L+3/2} \tag{2.11}$$

where α_{fs} is the fine structure constant ($\approx \frac{1}{137}$).

These equations show how the values are dependent on multiple factors, and are higher for low-energy, high-mass (specifically high-proton-number) nuclei, and both magnetic and high multipolarities. The curves which result from these equations are given in Figure 2.10 (for a Z=85 nucleus).

Detecting conversion electrons is extremely difficult given their resemblance to electrons emitted via β decay. Thus the effect of internal conversion is a reduction in the number of measured counts for all transitions by a factor relating to both the multipolarity and energy of the transition. Internal conversion intensity (I_e) is therefore accounted for using the internal conversion coefficient (α) as follows $I_{tot} = I_\gamma + I_e = I_\gamma(1+\alpha)$.

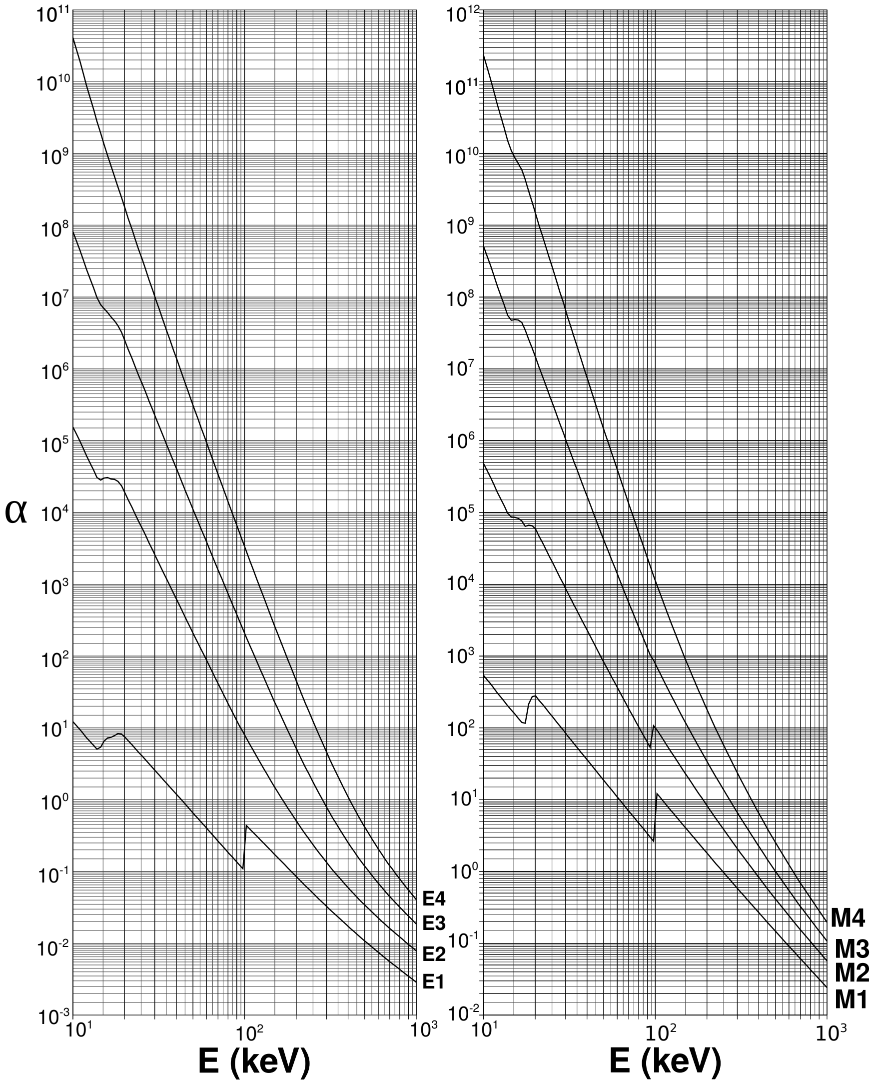

Figure 2.10: Total internal conversion coefficients with respect to energy for different multipolarities (for a Z=85 nucleus). From ref. [20].

Transition Multipolarity

The probability of γ-ray transitions between states in a given nucleus is primarily dictated by differences between the initial and final states; specifically the energy and spin-parity difference. Gamma-ray transitions tend to favour large energy gaps and low spin-parity changes. To gain a deeper understanding of nuclear transitions however, it's important to understand how these γ rays can be classified by both the order and type of multipolarity.

When a nucleus undergoes a decay between states, the initial and final states have defined angular momentum (I_i and I_f respectively). Therefore as angular momentum must be conserved by the angular momentum of the emitted photon, ***l*** must be given by equation 2.12:

$$|(I_i - I_f)| \leq l \leq (I_i + I_f) \tag{2.12}$$

Multipole radiation is classified as either electric or magnetic depending on whether the radiation is due to a shift in charge or current distribution. This is represented by E***l*** and M***l*** respectively, where ***l*** denotes the units of angular momentum and hence the order of the multipole (dipole (***l*** = 1), quadropole (***l*** = 2), octupole (***l*** = 3), etc.). For transitions such as these, parity must also be conserved. Electric and magnetic multipole radiations possess opposite parity for the same values of ***l***, these relations between angular momentum and parity (π) are shown in equations 2.13 and 2.14:

$$\pi_{electric} = (-1)^l \tag{2.13}$$

$$\pi_{magnetic} = (-1)^{l+1} \tag{2.14}$$

Based on equation 2.12 for states with greater angular momentum there will be multiple values for the photon angular momentum, as such it is important to calculate which transitions are most likely. To accomplish this, transition rate estimates are calculated using a simple single particle shell model, these values are shown in Figure 2.11.

From these estimates we can see clearly that lower order multipoles are highly favourable, and thus most observed transitions have multipolarity E1, M1 or E2 particularly for lower energies. In rare instances states are unable to decay to lower-lying levels via short-half-life transitions due to unfavourable energy and/or spin-parity differences. This results in the nucleus remaining in an excited state for longer. Such states are referred to as isomeric and feature in the structure of ^{208}Po [3].

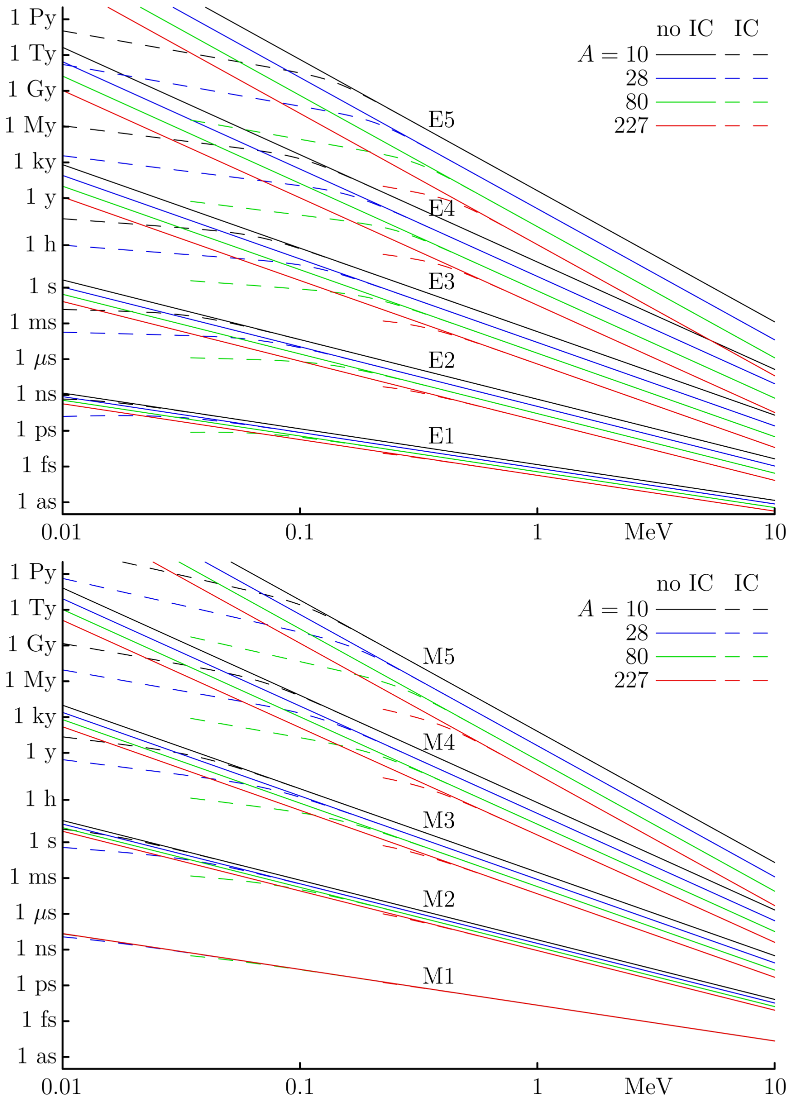

Figure 2.11: Weisskopf lifetime estimates for the lowest order electric and magnetic multipolarities; with dashed lines denoting the estimated effect of electron conversion [20].

2.2.2 β^- Decay

Beta- decay occurs in nuclei where instability is caused by an abundance of neutrons relative to the number of protons. In order to return to stability, the nucleus undergoes the decay process outlined in equations 2.15 and 2.16:

$$^A_Z X_N \rightarrow ^A_{Z+1} Y_{N-1} + e^- + \bar{\nu}_e \tag{2.15}$$

$$n \rightarrow p + e^- + \bar{\nu}_e \tag{2.16}$$

In this decay process a neutron inside the nucleus is converted into a proton, with an electron and anti-electron neutrino released to conserve charge and lepton number. Depending on the Q value and spin-parity of the parent nucleus, the resulting daughter nucleus is often in an excited state, the exact energy and spin-parity of which is dictated by the selection rules outlined later in Section 2.2.3. It is also worth noting that β^- decay is the process by which nuclei generated in the *r*-process, return to stability.

2.2.3 β^+ Decay

As its name suggests, in many ways β^+ decay functions as the reverse of β^- decay, and is the result of proton abundance within a nucleus. Equations 2.17 and 2.18,

$$ {}^{A}_{Z}X_N \rightarrow {}^{A}_{Z-1} Y_{N+1} + e^+ + \nu_e + e^- \tag{2.17} $$

$$ p \rightarrow n + e^+ + \nu_e \tag{2.18} $$

, show the process by which β^+ decay occurs in terms of nuclei and particles respectively.

As shown in these equations, β^+ decay is a process in which one of the abundant protons is converted into a neutron. As a result of this conversion a positron and electron neutrino pair are released to ensure that both charge and lepton number are conserved in the process. beta+ decay facilitates a decay path for proton rich nuclei to return to stability.

Electron Capture

Electron capture competes directly with β^+ decay. The decay process for EC decay is shown in equations 2.19 and 2.20,

$$ {}^{A}_{Z}X_N + e^- \rightarrow {}^{A}_{Z-1} Y_{N+1} + \nu_e \tag{2.19} $$

$$p + e^- \rightarrow n + \nu_e \tag{2.20}$$

Although both decay processes result in the conversion of a proton to a neutron, there are a few key differences which become apparent through comparison with equations 2.17 and 2.18. Electron capture results from an atomic electron being absorbed into the nucleus, which facilitates the conversion of one of the protons into a neutron. Unlike β^+ decay, there is no charge imbalance, and thus only an electron neutrino is required to balance the lepton number.

Electron capture, β^+, and β^- decay all typically occur when the parent nucleus is in its ground state, as is the case for ^{208}At. It is possible for a nucleus to decay from an isomeric state, but the half-life of the isomer would need to be comparable or longer than the β-decay half-life.

Q Value of β^+ and Electron Capture Decays

Another way in which electron capture and β^+ decay differ is in their Q values. The Q value for a given decay is determined by the difference in mass excesses between the parent atom and its daughter. This calculation is outlined in equations 2.21 and 2.22.

$$Q_{\beta^+} = [m(^AX) - m(^AY) - 2m_e]c^2 \tag{2.21}$$

$$Q_{EC} = [m(^AX) - m(^AY)]c^2 \tag{2.22}$$

, where $m(^AX)$ and $m(^AY)$ denote the atomic masses of the parent and daughter atoms. Atomic masses are used so that the binding energy of the electrons can be ignored. These equations demonstrate that for a given nuclear decay Q_{EC} will always exceed Q_{β^+} by $2m_ec^2$ ($\sim$1 MeV) [21].

beta decays of even mass nuclei result in an interesting sequence of Q values as the decay causes a switch between an even-even and an odd-odd nucleus (or vice versa). As a consequence, the pairing term of the semi-empirical mass formula switches sign which results in two distinct mass excess parabolas such as those shown in Figure 2.12 for A=208. Thus for even-even/odd-odd beta decay chains such as A=208, the Q_{β} value oscillates between high values for decays to even-even, and low for decays to odd-odd. This phenomenon is demonstrated by the gradient of the arrows in Figure 2.12.

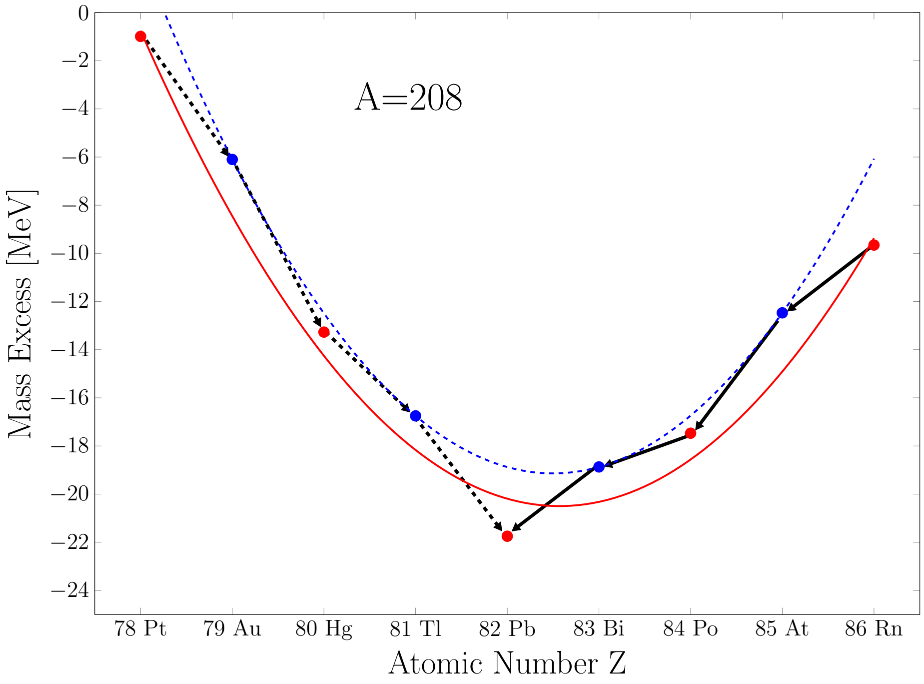

Figure 2.12: Mass excess for A=208. Red ● are the experimental values for even-even nuclei, with the blue ● indicating the same data for odd-odd nuclei [22]. The red, solid, and blue, dashed parabolas show the lines of best fit for both datasets. beta minus decays are shown by the dashed arrows, with β^{+}/EC decays shown by the solid arrows.

.

1

Selection Rules

Like γ decay, β decay and electron capture follow selection rules to determine which levels in the daughter nucleus are most favourable to decay to. As with γ decay, these rules are determined by the relative spin-parities and energy difference of the initial and final states. The selection rules for beta decay and electron capture also follow the general rule that lower spin-parity changes result in more favourable paths.

A nucleus cannot decay to a state with energy that exceeds the Q-value of the decaying nucleus. The difference between Q_{β} and Q_{EC} is the main component in determining the branching ratio between the two competing processes. If the energy difference is less than $2m_ec^2$ ($\sim$1 MeV) then β^+ decay cannot occur as there is insufficient energy with which to decay, thus for these transitions electron capture is the sole decay path. As the energy difference increases the branching ratio becomes increasingly favourable towards β^+ decay, however for ^{208}At, $\lambda_\beta/\lambda_{EC} \leq$0.15. This is crucial for the analysis presented in this report as although the states are still populated, electron capture has no emission which can be detected efficiently using the ISOLDE set-up, therefore the statistics in β coincidence spectra will be notably lower.

Any change in the state of the nucleus must be accounted for by the energy, but also the spin and angular momentum, of the emitted particles. When angular momentum laws are applied to the emitted particles the result is varying degrees of "forbiddenness" (decay likelihood) dependent on their orbital angular momentum. This relation is laid out in equation 2.23,

$$\vec{I}_i = \vec{I}_f + \vec{L} + \vec{S} \tag{2.23}$$

where I_i and I_f represent the spin of the initial and final nuclear states, and L and S represent the total orbital and spin angular momentum of the emitted particles.

Following this, for L=0 any change in I must be accounted for entirely by S. As both emitted particles have spin=$\frac{1}{2}$ their respective orientations can account for ΔI = 0,±1 with no parity change as parity is determined by L. Decays where L=0 are collectively referred to as allowed decays. Within this classification, Fermi decay refers to when the emitted particles are anti-parallel ($S = 0$), and Gamow-Teller decay occurs when the spins are parallel ($S = \pm1$). These L=0 transitions are usually dominant, but higher order transitions are also observed and are called L$^{\text{th}}$ forbidden transitions. First-forbidden transitions for example will result in ΔI = 0,±1, ±2 as well as a parity change. For second-forbidden transitions ΔI =±2 or ±3 with no parity change. Forbidden decays become more strongly suppressed as L increases, as such higher order transitions (above first-forbidden) are physically possible, but are significantly suppressed and are therefore rarely observed. The pattern of ΔI and $\Delta\pi$ change for the lowest-forbidden decays are outlined in Table 2.1.

Table 2.1: Summary of spin and parity changes for β decays with lowest levels of forbiddeness.

Transition	Type	Spin Change	Parity Change
Allowed	Fermi	0	No
	Gamow-Teller	0,±1	
First-forbidden	non-unique	0, ±1	Yes
	unique	±2	
Second-forbidden	non-unique	±2	No
	unique	±3	

log*ft* Values

The extent to which a given state in a daughter nucleus is populated through β decay is often expressed via the *ft* value shown in equation 2.24,

$$ft_{\frac{1}{2}} = \ln 2 \frac{2\pi^3\hbar^7}{g^2 m_e^5 c^4 |M_{fi}|^2} \tag{2.24}$$

, where g is a β decay strength constant; M_{fi} is the nuclear matrix element; $t_{\frac{1}{2}}$ is the half-life of the β decay; and f is the Fermi integral which is dependent on the proton number of the daughter nucleus and the maximum electron energy. The Fermi integral is vital as it accounts for the effect of the daughter nucleus' Coulomb field on the transitions. The relation between *ft* and $|M_{fi}|$ is such that it can be used as a simple metric for how populated a given state will be in the daughter nucleus. Typically, $\log_{10}$*ft* is used due to the wide range of values *ft* can take. Table 2.2 gives the observed upper and lower $\log ft$ limits for given decay types, while Figure 2.13 shows how these log*ft* values are distributed for varying degrees of forbiddenness.

Table 2.2: Summary of logft limits taken from ref. [23]. * indicates limits specific to even A nuclei.

Transition	Min. logft	Max. logft
$^{*}\Delta J = 0, \Delta\pi =$no	4.1	10.6
$^{*}\Delta J = 1, \Delta\pi =$no	3.0	10.0
$^{*}\Delta J = 0, \Delta\pi =$yes	5.1	11.0
$^{*}\Delta J = 1, \Delta\pi =$yes	5.2	19.1
$\Delta J = 2, \Delta\pi =$yes	7.5	12.8
$\Delta J = 2, \Delta\pi =$no	10.6	14.2

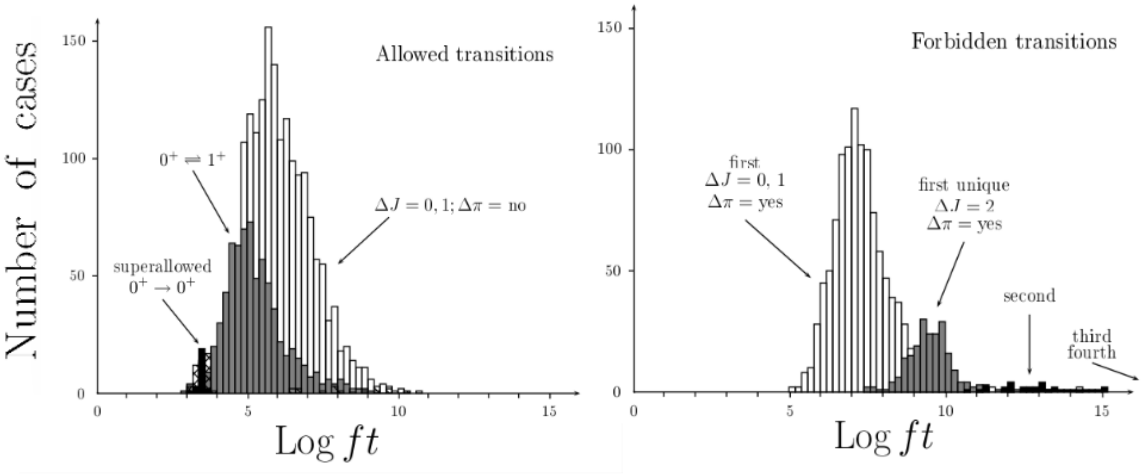

Figure 2.13: Distribution of logft values for both allowed and forbidden transitions of well-defined β decays [24]

.

Both clearly demonstrate the lower distributions of allowed decays. The significant overlap of distributions such as $0^+ \to 1^+$ and ΔI=0,1; $\Delta\pi$=no, can cause difficulties in inferring a final state's parity from its logft value, but they can still provide insight in this regard.

β^+/EC Decay of ^{208}At

Astatine-208 undergoes β^+/EC decay from its ground state, with $J^{\pi} = 6^+$ and $Q_{EC} = 4999(9)$ keV [22] to a number of excited states in ^{208}Po. These possible decay paths are determined primarily by the beta selection rules outlined above, however other factors specific to the structures of ^{208}At and ^{208}Po also affect potential populated states.

The valence protons in ^{208}At lie in the $h_{9/2}$ level above the Z=82 shell closure. Protons can decay from higher lying states in ^{208}At, however only the $f_{7/2}$ and $i_{13/2}$ states above the Z=82 shell closure are feasible. Furthermore, protons can decay from states below Z=82, but this is also less likely as these protons are in fully occupied shells, making their decay less energetically favourable. Figures 2.14a and 2.14b show the possible EC/β^+ decay paths with single particle energies taken from ^{207}Tl, ^{209}Bi, ^{207}Pb, and ^{209}Pb [25, 26].

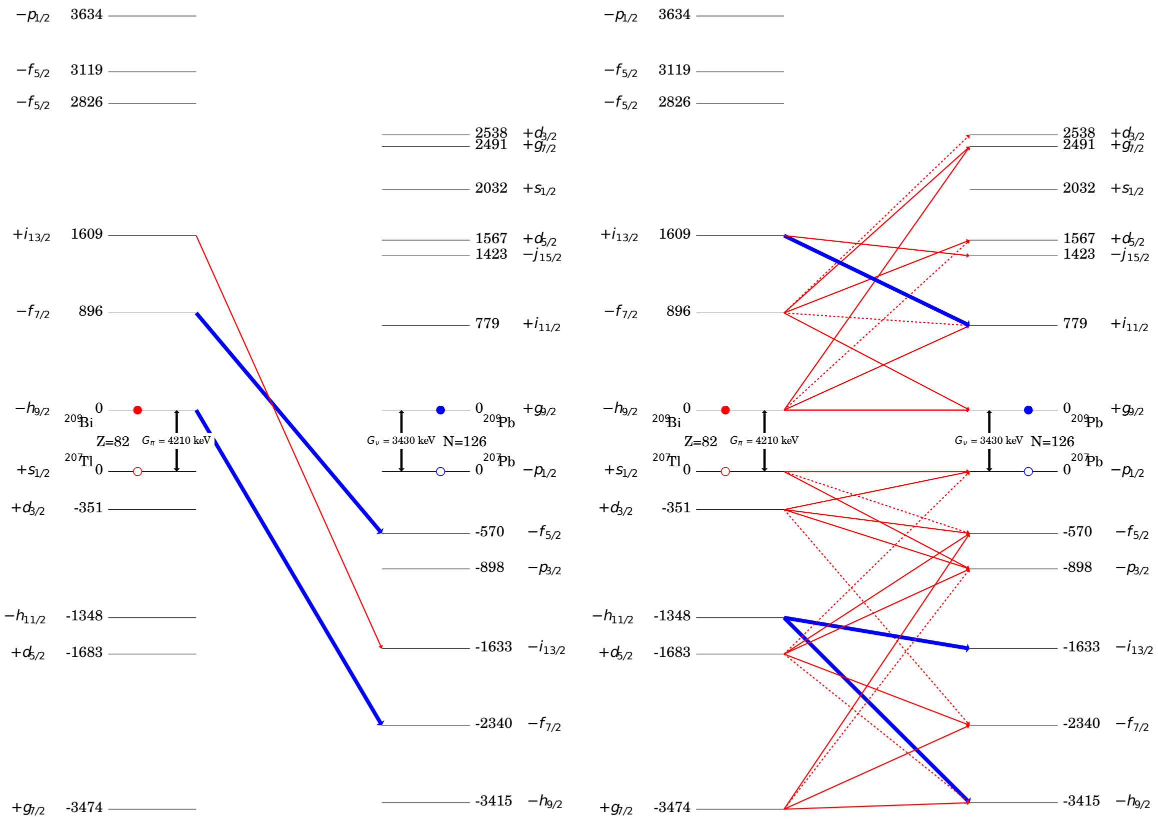

(a) (b)

Figure 2.14: Scheme for potential EC/β^+ decays, with energies taken from single particle states. Spin-parity is given beside each state. Thick arrows represent allowed decays, thin arrows are first-forbidden decays, thin dashed arrows are first unique decays. Red and blue circles are used to indicated proton and neutron particles and holes. (a) Potential EC/β^+ decays with no excitation across the shell gap. (b) Potential EC/β^+ decays with a single excitation across the shell gap.

Although it is possible for ^{208}At to decay to final states in ^{208}Po with any number of particle-hole excitations, states with more than one-particle-one-hole are not possible as the value of Q$_{EC}$ is less than the excitation energy of the lowest energy two-particle-two-hole excitations. The Q$_{EC}$ value also prevents a super-allowed $\pi h_{9/2} \rightarrow \nu h_{9/2}$ decay, as the main strength of the

$\nu(h_{9/2}^{-1}f_{5/2}^{-1})_{6^+}$ and $\nu(h_{9/2}^{-1}p_{3/2}^{-1})_{6^+}$ states exceed the Q_{EC} value (around 5 MeV [27] in ^{206}Pb).

Figure 2.14a only shows three possible decay paths where additional energy is not needed to overcome the shell gap. Due to this limitation we would expect to see very few low-energy states populated by ^{208}At, as the majority of decays require shell breaking, see Figure 2.14b. The other conclusion which can be drawn from Figure 2.14b is the abundance of first-forbidden decays. Although these transitions are still suppressed, the lack of possible allowed decays will result in a greater proportion of populated states which require a change in parity. Astatine-208 decays from its 6^+ ground state, thus we would anticipate a large number of populated $5^-, 6^-$, and 7^- states. Decays to 4^- and 8^- states are also possible, however these require first-unique decay and are thus more heavily suppressed.

2.3 Radiation Detection

2.3.1 Germanium Detectors

Germanium detectors are one of the most widely used γ-ray detectors as they make use of semiconductor properties to provide an exceptionally good energy resolution; which is crucial to a wide range of experiments. The detection medium consists of a charge-carrier-abundant region (valence band), and a charge-carrier-deficient region (conduction band). In semiconductor detectors, a depletion region with no charge carriers must also be present in the conduction band.

The detection process for a germanium detector is as follows. Incoming γ rays excite electrons from the valence band to the conduction band leaving a relative positive charge or 'hole' in the valence band, referred to as an electron-hole pair. An electric field then causes the equal and opposite charges to drift towards the electric contacts, producing a current. The number of electron-hole pairs produced is proportional to the energy deposited by the γ ray, thus the current produced by these pairs is proportional to the energy of the incoming γ ray. In order to achieve these measurements for γ-ray energies a high depletion region thickness, d, is required, the equation for which is given in equation 2.25[28],

$$d = \left(\frac{2\epsilon V}{eN} \right)^{1/2} \tag{2.25}$$

where ϵ is the dielectric constant, V is the reverse bias voltage, e is the charge of an electron, and N is the net impurity concentration. Thus, for a given voltage, depletion region thickness is purely affected by N; the level of impurity in the material.

To achieve a high purity, germanium crystals undergo a refinement process called zone refining. During this process, a region of germanium is melted and moved along the crystal, collecting and carrying impurities within it to one end of the crystal. After this procedure is carried out multiple times, a low-impurity (as few as 10^9 atoms/cm^3) germanium crystal is achieved, often referred to as a high-purity germanium or HPGe. For typical operating voltages, HPGe crystals can achieve a depletion region thickness of a few centimetres.

Before the introduction of zone refining methods, germanium crystals were doped with lithium to counteract residual impurities. Although comparable to HPGe detectors of the same size, Ge(Li) crystals must be kept cool in order to maintain their properties as lithium dopants will drift out of the detector if it is allowed to warm. This makes them considerably less operationally convenient than HPGes which only require cooling during operation and can be allowed to warm.

Cooling

Germanium detectors have a very low band gap (E$_{gap}$=0.67 eV [29]) and as such are susceptible to thermal generation of charge carriers at room temperatures destroying their energy resolution. The probability of this occurring is given by equation 2.26,

$$p(T) = CT^{3/2}e^{-E_{gap}/2kT} \tag{2.26}$$

where T is the absolute temperature, C is a proportionality constant characteristic of the material, E_{gap} is the band gap energy, and k is the Boltzmann constant[28]. To combat this, germanium detectors are cooled below 100 K, such that only γ-ray interactions can induce an electron-hole pair. Typically this cooling is achieved using liquid nitrogen in a vacuum sealed cryostat mounted such that the coolant is in thermal contact with the crystal.

2.3.2 Interactions of γ rays with Matter

Gamma rays are not limited to exciting charge carriers in the germanium crystals, and in fact undergo three interactions which can impact the resulting spectra; Compton scattering, pair production, and the photoelectric effect. Their prevalence is dependent on both the energy of incoming photons and the proton number of the absorber as shown in Figure 2.15.

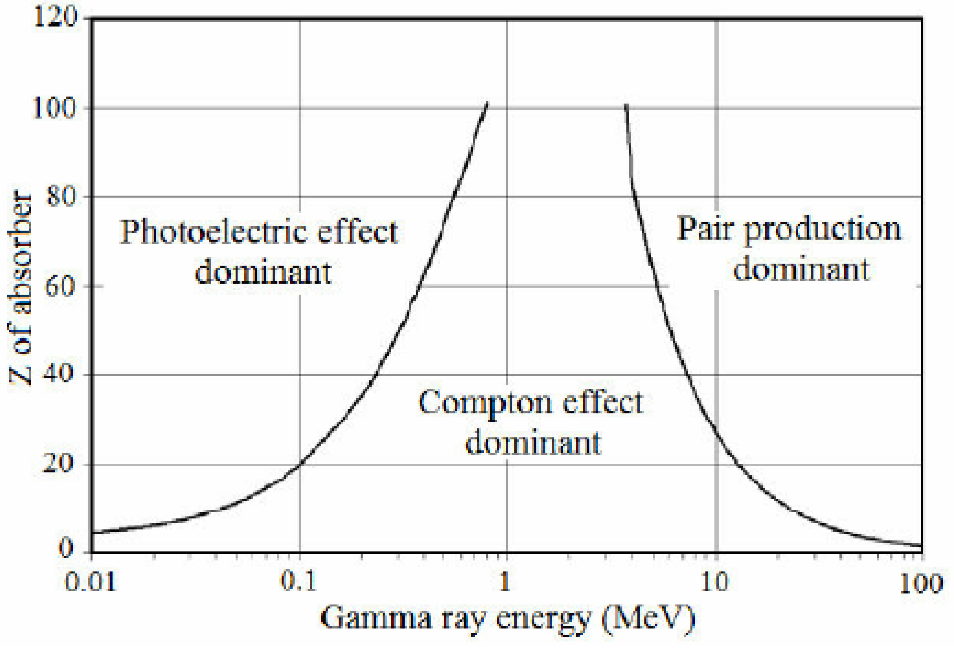

Figure 2.15: Dominance of the three main γ-ray interactions with matter in relation to absorber proton number and photon energy. Figure taken from ref. [28].

.

Compton Scattering

Compton scattering is the inelastic scattering of a photon with a charged particle. For decay spectroscopy this interaction takes place between an incoming γ ray and atomic electrons inside the detection medium and is the most dominant of the three interactions for energies ranging from 0.1-4 MeV [30]. This effect causes significant inefficiencies for germanium detectors as only a portion of the photon's energy is deposited within the detector. After which the photon scatters to either be fully absorbed, scatter again, or exit the detector unmeasured. For the spectrum, counts which are the result of Compton scattering can obscure lower-energy, lower-intensity γ rays and are therefore impractical for analysis of gamma-ray spectra.

One method by which the Compton effect is mitigated is by summing γ rays that occur in adjacent detectors at around the same time; this is known as an 'add-back' correction, and is common in γ spectroscopy. Although add-back increases overall detection efficiency occasionally, high intensity peaks will randomly fulfil the conditions of the add-back correction resulting in false peaks at the sum of their energies. These false peaks are significantly less detrimental than Compton scattering however due to their known energies, and thus add-back correction is used for the analysis in this report.

Pair Production

Pair production refers to the process by which a photon with energy greater than twice the rest mass of an electron ($2 \times 0.511 = 1.022$ MeV) will spontaneously produce an electron-positron pair. When this occurs, excess energy is transferred as kinetic energy to the electron and positron, the latter of which annihilates with an atomic electron generating two 511 keV photons. The resultant γ rays are subsequently absorbed by, or escape the detector which produce a 511 keV or a 1022 keV sum peak in the spectrum respectively. Pair production is more prevalent at higher energies, and is dominant above $\sim$5 MeV.

Photoelectric Effect

The photoelectric effect refers to the process by which an incoming photon is absorbed by an atomic electron resulting in it being emitted from the surface of the material. In this interaction, the energy of the emitted electron (E_e) is equal to the photon energy (E_γ) minus the electron's binding energy (E_b); $E_e = E_\gamma - E_b$. An X-ray is subsequently released due to the de-excitation of outer electrons to fill the vacancy left by the emitted (typically K-shell) electron. The photoelectric effect is most prevalent at lower energies below a few hundred keV and for high-mass nuclei, consequently its effect is minimal for gamma-ray spectroscopy.

2.3.3 β Decay Detection

The detection of β^+ radiation is achieved using a scintillator material in conjunction with a set of PhotoMultiplier Tubes (PMTs), the schematic for which is shown in Figure 2.16. Plastic scintillators are preferred to other higher-mass scintillation materials as their low mass reduces the effects of back-scattering and reduces the number of interactions between the positron and the scintillation medium. The detection process is instigated when incoming, high-energy positrons excite electrons in the scintillator, which subsequently de-excite, releasing photons. These photons strike the photocathodes of the PMTs producing an electron inside the PMT, which is focused onto a dynode by a focusing electrode. The electron signal is then directed onto a series of dynodes of increasing voltage, the result of which is a cascade of electrons which is then detected as an electronic signal at the end of the PMT. This process is demonstrated in Figure 2.16.

Nuclei which undergo β^+ decay can also decay via electron capture; for ^{208}At this is the primary decay process. It is important therefore to note that scintillation detectors can only efficiently detect charged particles such as electrons and positrons. Thus the neutrally-charged electron neutrinos produced through electron capture will not be observed. X-rays emitted through EC decay can be detected, however the efficiency of this is substantially lower than

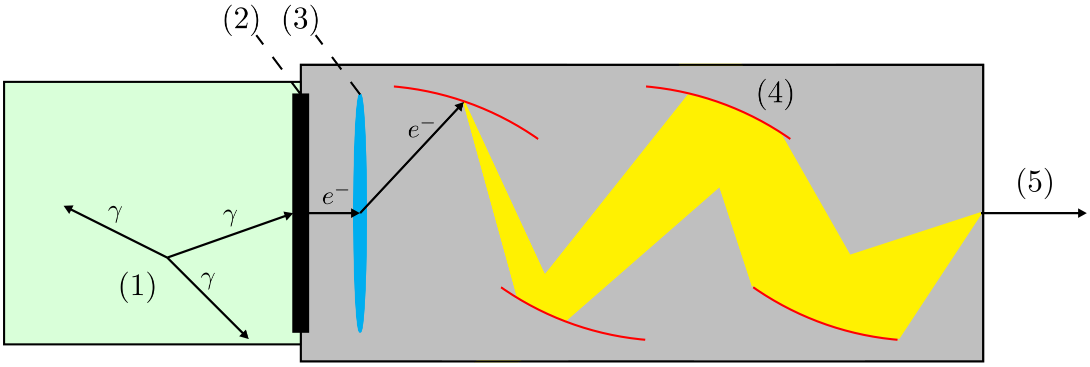

Figure 2.16: Scintillator and Photomultiplier tube internal mechanism. (1) Initial interaction between the charged particle and the plastic releasing visible photons. (2) Photons hit the photocathode of the PMT releasing an electron. (3) The electron is focused onto the dynode with an focussing electrode. (4) The dynodes amplify the number of electrons into a cascade. (5) The electrons are measured as a signal.

charged particle detection. As a consequence, only a fraction of decays will be measured, which could substantially impact subsequent analysis and β-coincidence spectra.

Chapter 3

Scientific Motivation

3.1 The Near ^{208}Pb Mass Region

With closed neutron and proton shells ($N = 126$ and $Z = 82$) ^{208}Pb is the heaviest, stable, doubly-magic nucleus and has been studied extensively as a result. From these investigations the structure of ^{208}Pb was found to contain no low-energy rotational states, and thus the spherical shape, assumed by the lack of valence nucleons, was confirmed. This spherical nature can be extended to the four-valence-nucleon nucleus of ^{208}Po. The closed proton and neutron shells also present challenges for single-particle excited states, as excitation across the shell gap is required. Consequently such states are only observed above ∼3 MeV, including the 3475.1 keV 4^- state with configuration $\nu g_{9/2} p_{1/2}^{-1}$ observed in ^{208}Pb [3].

3.1.1 Octupole Collectivity

The most notable feature in the structure of ^{208}Pb is its lowest-energy excited state; a 3^- state at 2614.5 keV. This state does not arise from a single particle-hole excitation, but is instead the result of the collective behaviour of multiple $\Delta l = \Delta j = 3$ excitations across the shell gaps. These excitations are shown in Figure 3.1 for pairs close to the shell closures.

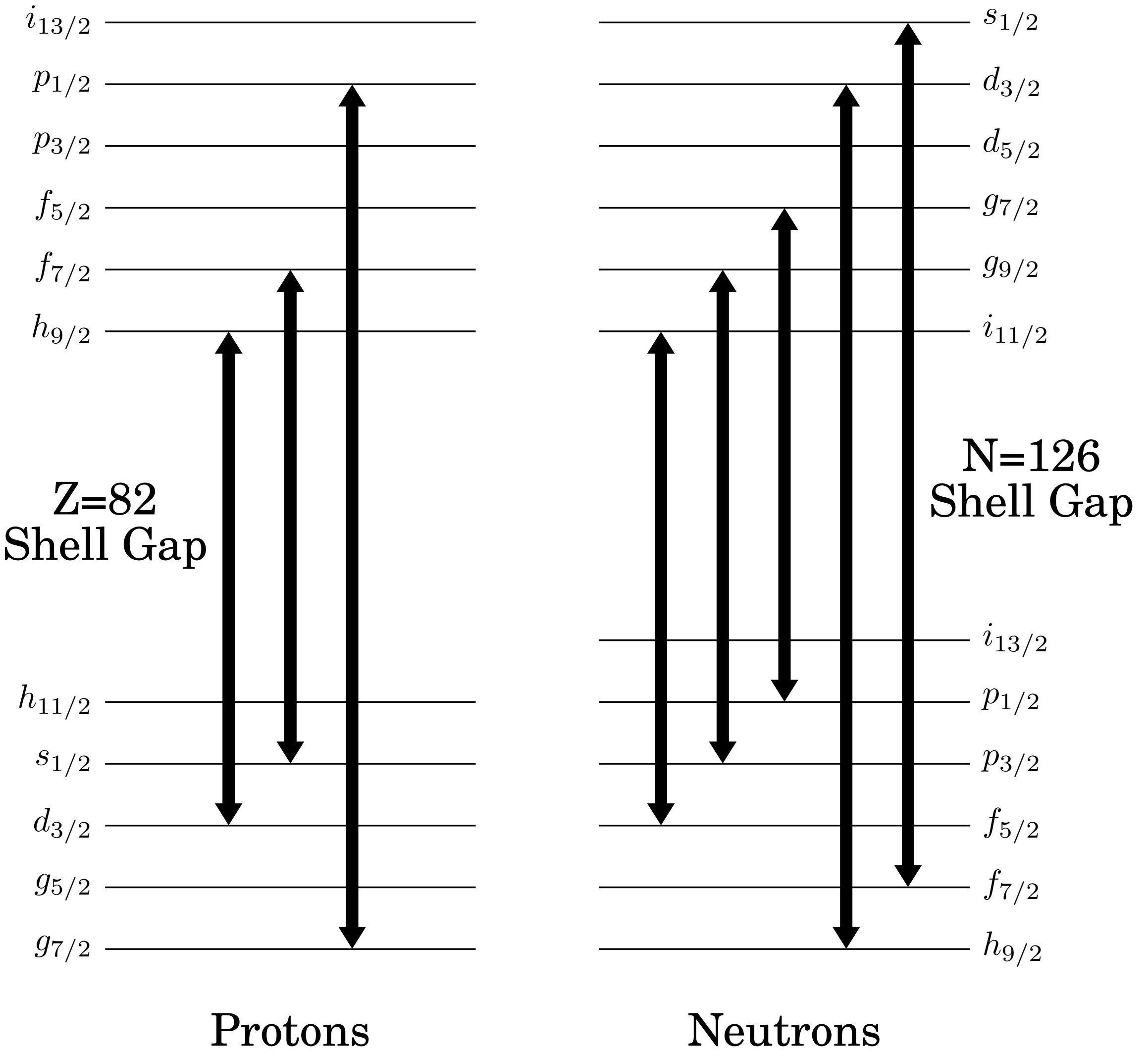

Figure 3.1: Excitations across the proton and neutron shell gaps Z=82 and N=126 for orbital pairs in ^{208}Pb with $\Delta l = \Delta j = 3$. Orbital state energies not to scale.

The majority of these shell gap transitions are also possible in the nuclei close to ^{208}Pb. As such, octupole collectivity has been observed in many nuclei close to ^{208}Pb including ^{206}Pb, ^{207}Pb, and ^{209}Bi [25–27]. Due to the many components involved from all the contributing orbitals, accurately simulating collective states is extremely difficult. Therefore, investigating such states experimentally can improve understanding of the contribution strengths of the state, as well as collective phenomena more generally.

The following details the current understanding of the octupole states of: ^{208}Pb (closed shells), ^{206}Pb (two valence neutron holes), ^{210}Po (two valence proton particles), and ^{208}Po (two valence neutron holes and two valence proton particles).

^{208}Pb

The 2614.5 keV first-excited state of ^{208}Pb de-excites via a 2614.5 keV transition to the ground state with B(E3)=33.8(6) W.u. [31]. This high transition strength is indicative of a highly collective nature. As the octupole phonon is coupled to the ground state of a doubly-magic nucleus, the 2614.5 keV transition provides a point of comparison for other octupole collectivity in the region.

A 2318 keV E3 transition was observed to de-excite to the 6743 keV ($\nu j_{15/2} i^{-1}_{13/2}$) 14$^-$ state, the octupole character was later confirmed using angular distribution measurements [2].

States resulting from multiple octupole phonons are also present in the structure of ^{208}Pb. gamma-gamma coincidence measurements were used to identify a transition from the 5241 keV 0$^+$ double-octupole state to the 2614.5 keV first-excited state [3].

^{206}Pb

Similar to ^{208}Pb, a strong B(E3) value (20 W.u) was determined for the 2648 keV transition from the 3$^-$ state to the ground state [31]. In the case of ^{206}Pb however, there are a number of excited states below the octupole state. An E3 transition with energy 2559 keV is tentatively assigned to de-excite an octupole vibration on the 2658 keV 9$^-$ state (configuration $\nu i^{-1}_{13/2} f^{-1}_{5/2}$). An tentatively assigned octupole vibration on the 4027 keV 12$^+$ state (configuration $\nu i^{-2}_{13/2}$) is de-excited by a 2403 keV transition. This was determined from data taken in a ^{204}Hg($\alpha, 2n$) experiment [32].

^{210}Po

A 2767 keV transition populates the 1557 keV 8$^+$ ($\pi h^2_{9/2}$) from the 4324 keV 11$^-$ state [33]. This transition is tentatively assigned to have collective octupole character, however this is yet to be confirmed experimentally.

^{208}Po

Despite lying close the ^{208}Pb mass region, no substantial evidence of octupole collectivity currently exists for ^{208}Po.

3.1.2 Competition Between Allowed and First-forbidden β Decay

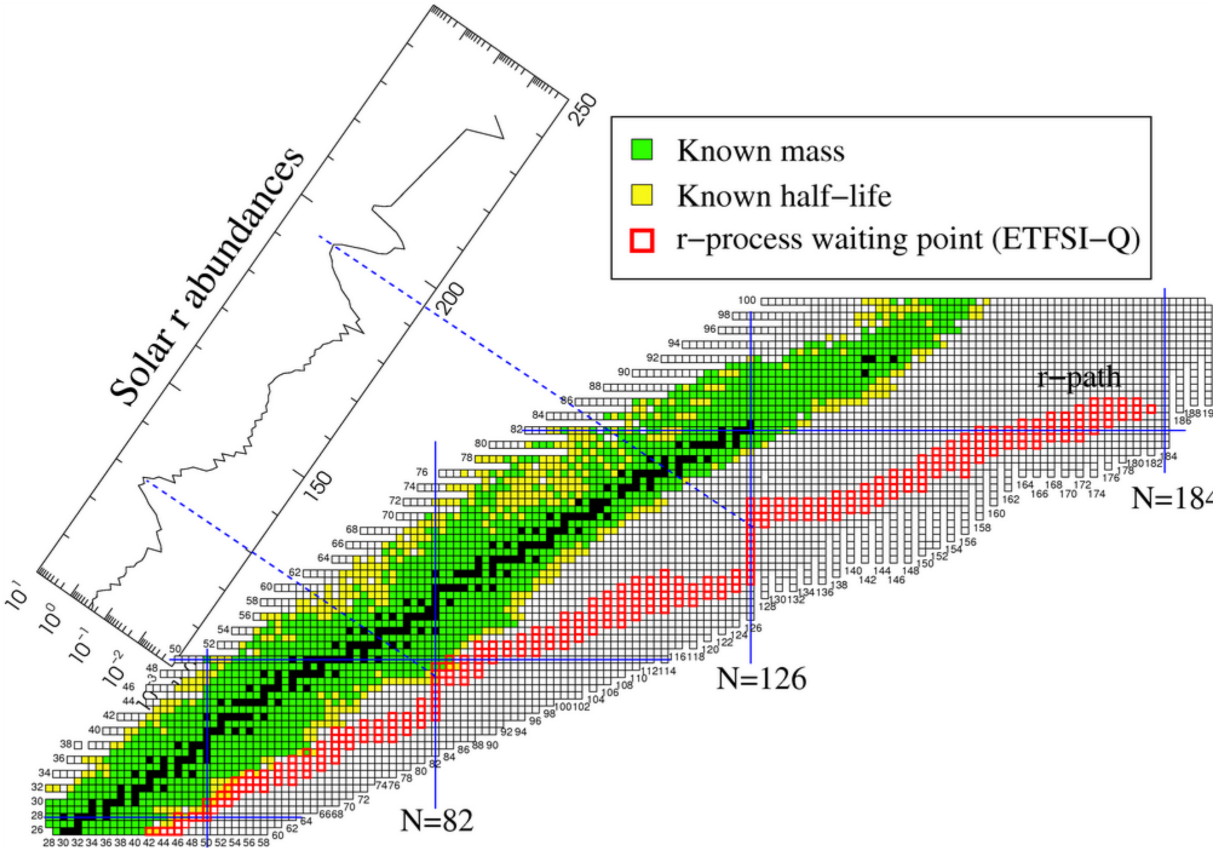

Figure 3.2: Segrè chart excerpt showing *r*-process waiting point nuclei. The secondary graph shows solar abundances in the r-process with peaks at A∼130 and A∼195. These peaks correspond to the increased density of waiting point nuclei which result from the N=82, and N=126 magic numbers respectively [34].

Neutron rich N=126 nuclei and those in the region around them are of particular importance to the *r*-process [35–37], as their stability, by virtue of the neutron shell closure, results in an abundance peak at A∼195 (shown in Figure 3.2). These waiting point nuclei lie far from stability and are thus experimentally unreachable [38, 39]. As such, understanding of nucleosynthesis in this region is heavily reliant on theoretical calculations. Models of the *r*-process are dependent on multiple factors including: neutron capture cross sections, half-lives, Q values, and decay paths. These fundamental properties are difficult to calculate, and the predictions that have been made vary significantly [35, 36, 40–45]. A number of global calculations which cover regions of interest for the *r*-process have been published [35, 40, 45]. These global calculations all use mean-field approaches as shell model calculations are infeasible when dealing with nuclei so far from closed shells.

Typically first-forbidden decays are ignored for β decay simulations as their contributions to the decay rate are negligible. However, the influence of first-forbidden decays increases with nuclear radius and Q value. Consequently, around N=126 the contribution exceeds 50%, as is shown in Figure 3.3. The first-forbidden contribution also becomes increasingly important for nuclei near stability, as allowed decay paths becomes more scarce and suppressed. Despite it being well established that first-forbidden decays play a key role in the determination of β decay rates in the N=126 mass region, calculating first-forbidden decays remains notoriously difficult.

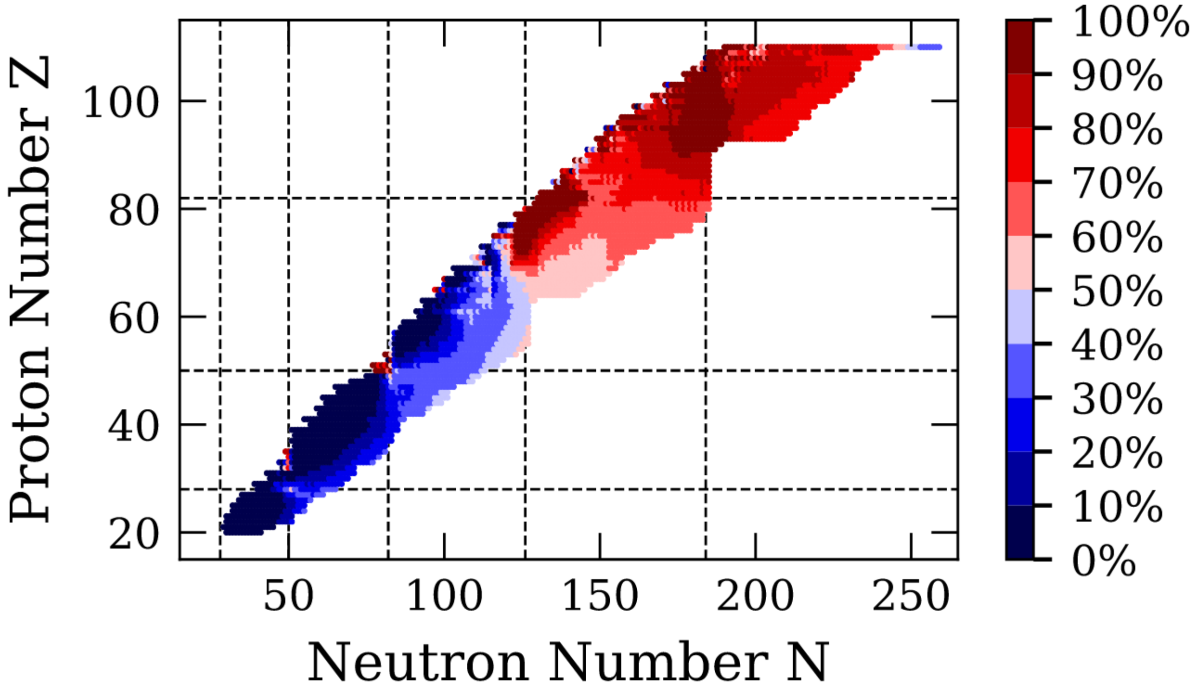

Figure 3.3: First-forbidden contribution to decay rates. Magic numbers are indicated by dashed lines [40].

Competition between first-forbidden and allowed decays is also prevalent for N$\sim$126 nuclei on the proton-rich side of the nuclide chart. However unlike the waiting point nuclei, they are more easily reached experimentally. Although β^- and β^+ decays are fundamentally different, conclusions drawn regarding first-forbidden competition in β^+ decay will provide insight for β^- decay. As such, experiments studying β^+/EC decays in this region can provide experimental data with which to broaden understanding of first-forbidden decays. In addition to this they provide a testing ground of experimental data with which to test the validity of theoretical calculations.

3.1.3 Other Features of Interest in ^{208}Po

In addition to the octupole collectivity and high first-forbidden decay proportion, analysis of a high statistics decay spectroscopy experiment also offers opportunities to expand upon prior work. Specifically, the structure of ^{208}Po features a long-lived isomeric state at 1528 keV ($t_{1/2} = 350(20)$ ns [3]), in addition to a number of unconfirmed states and unplaced transitions [4, 5, 46, 47] which can all be studied in greater detail through analysis of this dataset.

Chapter 4

Experimental Details

4.1 ISOLDE

The Isotope mass Separator On-Line facility (ISOLDE) at CERN has been performing nuclear physics experiments with radioactive beams for over fifty years, making it one of the oldest facilities at CERN. The proton beam that facilitates ISOLDE's own beams uses a combination of a linear accelerator (LINAC2) and the Proton-Synchrotron (PS) Booster, which is composed of four synchrotron rings. A full schematic of the accelerator layout at CERN including LINAC2, the PS, the PS Booster, and ISOLDE is shown in Figure 4.1.

The PS Booster takes protons from LINAC2 at 50 MeV and fires them into the proton synchrotron at 1.4 GeV [48, 49] in cycles, where each cycle is made up of $\sim$30 pulses which occur every 1.2 s. This set-up is designed primarily to supply high-energy protons to the PS however, the intensity of these cycles is such that as many as half of the protons supplied by the PS booster can be redirected to ISOLDE. These redirected pulses correspond to a maximum proton current of $\sim 2\ \mu$A at ISOLDE.

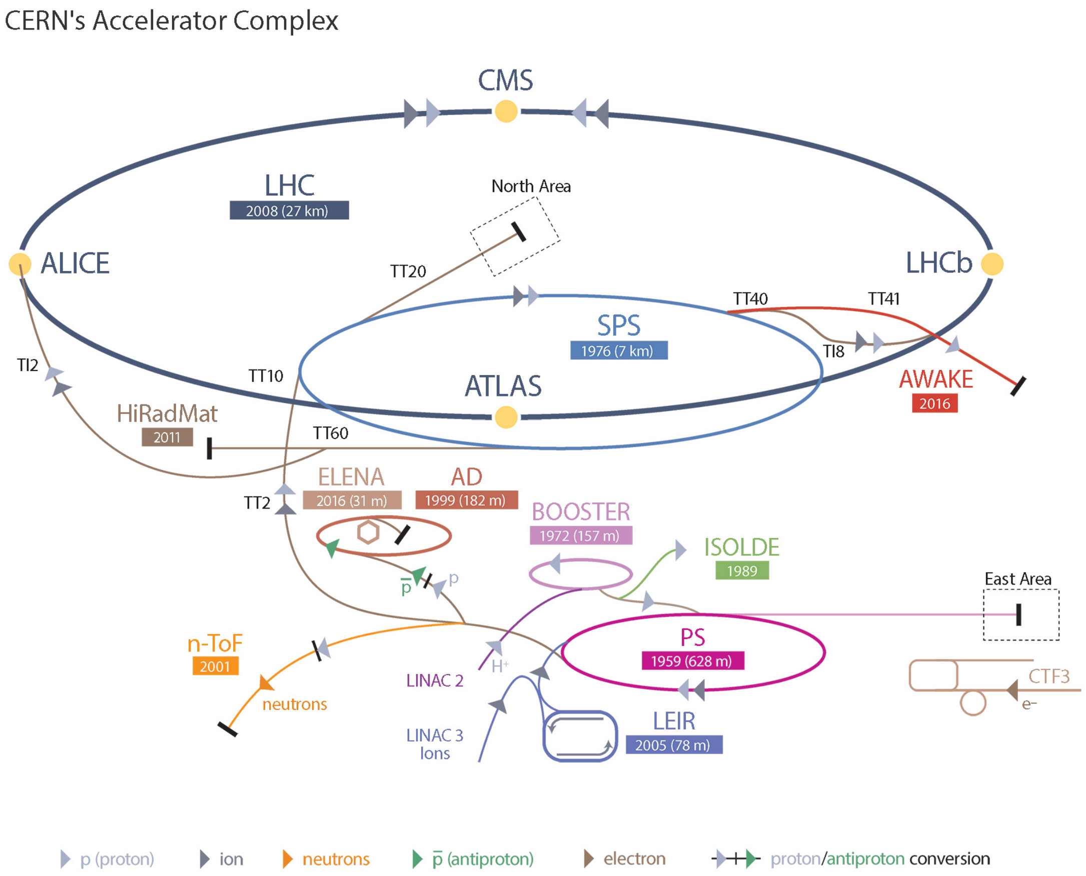

Figure 4.1: CERN layout showing how the LINAC2 and PSB work in combination to supply protons to ISOLDE. Image take from cds.cern.ch.

4.1.1 Beam Production

At ISOLDE the pulsed proton beam is incident on a target, for the purposes of the ^{208}Po experiment a molten lead target was used in conjunction with a VD5 FEBIAD (Forced Electron Beam Induced Arc Discharge) [50] ion source. The protons collide inelastically with the lead atoms; the products from these interactions then diffuse to the surface where they are extracted and ionised. A labelled cross section of this set-up can be seen in Figure 4.2.

ISOLDE's primary radioactive ion beam is extracted at 30-50 keV and fed to one of the two mass separators: the High-Resolution Separator (HRS) and the General Purpose Separator (GPS). The GPS consists of a single bending magnet making it simple to operate, but due to this set-up it is only able to achieve a mass resolution power of $M/\Delta M \sim 1000$ [52]. By comparison the HRS, which consists of two bending magnets, is able to provide a higher mass resolution

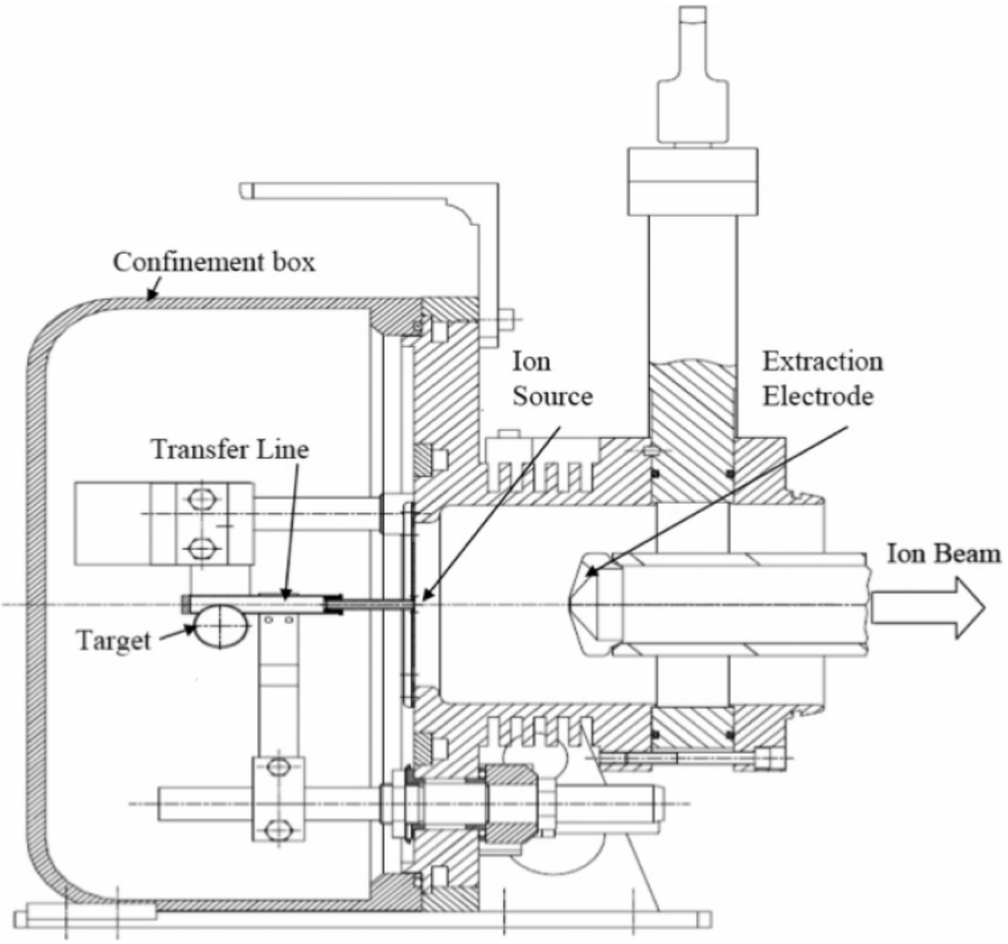

Figure 4.2: Cross section of the ISOLDE target, from ref. [51].

power of $M/\Delta M < 5000$, however this restricts the beam and results in lower yields which can be severely detrimental for many experiments. The disparity in mass resolution becomes significantly smaller for higher mass isotopes, thus for this experiment the GPS was selected as the higher yields justified a slightly lower resolution. This low-energy, primary radioactive ion beam can be redirected along multiple secondary beam lines for different experimental set-ups at ISOLDE including: Penning-trap mass spectrometry at ISOLTRAP; laser spectroscopy at CRIS (Collinear Resonance Ionisation Spectroscopy); re-acceleration with HIE-ISOLDE; and the ISOLDE Decay Station (IDS) used for this experiment.

4.1.2 Production of ^{208}Po

The original intent of the experiment was to measure decays of ^{208}Hg ($t_{1/2} = 135(10)$ s [53]. However, an unexpectedly high yield of ^{208}At at $\sim 5 \times 10^4$ pps was observed in the beam. Consequently a fraction of the data collected were also used to investigate the β-population of its daughter nucleus, ^{208}Po.

The decay of ^{208}At is outlined in Section 2.2.3. Astatine-208 decays from its ground state ($J^\pi = 6^+$, $Q_{EC} = 4999(9)$ keV [22]) consequently, the observed states are restricted to relatively low-energy ($<Q_{EC}$) and low-spin states by virtue of beta-decay selection rules (see Section 2.2.3). These restrictions offer an opportunity to observe these states more exclusively than other production methods such as those used in a number of low-mass projectile experiments investigating ^{208}Po [54–56].

Three protons must be gained by nuclei in the lead target in order to produce ^{208}At (which has 85 protons and 123 neutrons). Furthermore for the most abundant isotope in the lead target (^{208}Pb) three neutrons must be lost, resulting in a net change of six nucleons. This significant change in nucleons means that a high-energy, pulsed, proton beam incident on a molten lead target will not typically result in a high yield of ^{208}At. Consequently, the production process which resulted in an abundance of ^{208}At in the spectrum is somewhat unclear. The most likely explanation is through protons interacting with ^{209}Bi contaminants within the lead target, these reactions are described below in equations 4.1–4.3:

$$^{209}\mathrm{Bi}(p, \pi^- xn)^{210-x}\mathrm{At} \tag{4.1}$$

$$^{209}\mathrm{Bi}(^3\mathrm{He}, xn)^{212-x}\mathrm{At} \tag{4.2}$$

$$^{209}\mathrm{Bi}(^4\mathrm{He}, xn)^{213-x}\mathrm{At} \tag{4.3}$$

and explored in greater detail in refs. [57, 58].

Although equation 4.1 is the only reaction capable of producing ^{208}At solely from a proton beam; the interactions shown in 4.2 and 4.3 must also be considered due to the thickness of the target material.

4.2 The ISOLDE Decay Station

The ISOLDE Decay Station (IDS) has provided a permanent experimental area to perform decay spectroscopy experiments since 2014. The experimental area is set up at the end of the beam line with a shell-like structure which houses a vacuum-sealed chamber containing a length of aluminised Mylar tape. Radioactive ions implant onto the tape and decay, releasing radiation which is measured by the surrounding detectors. The IDS also utilises an automatic pulley system such that implanted sections of tape can be moved away from the detectors to avoid radiation from undesired decays and contaminants obscuring spectra. The decays are measured by the surrounding, resident, High-Purity, Germanium (HPGe) detectors, in addition, the IDS is equipped to allow for auxiliary detectors to be installed for each experiment.

4.2.1 Resident IDS Germanium Detectors

The permanent detector set-up at the IDS consists of four backwards-angle, germanium clover detectors [59]. Each detector consists of four cylindrical High Purity Germanium (HPGe) crystals, which are cooled by liquid nitrogen through a central nozzle. Each crystal measures 50x50x70 mm, tapered to a bevelled rectangle to allow for narrow and precise spacing between crystals within the detector. The detectors are placed at an angle of 125° with respect to the vector of the beam line, with 70° between adjacent, and 110° between opposite clover faces. This is shown graphically in Figure 4.3.

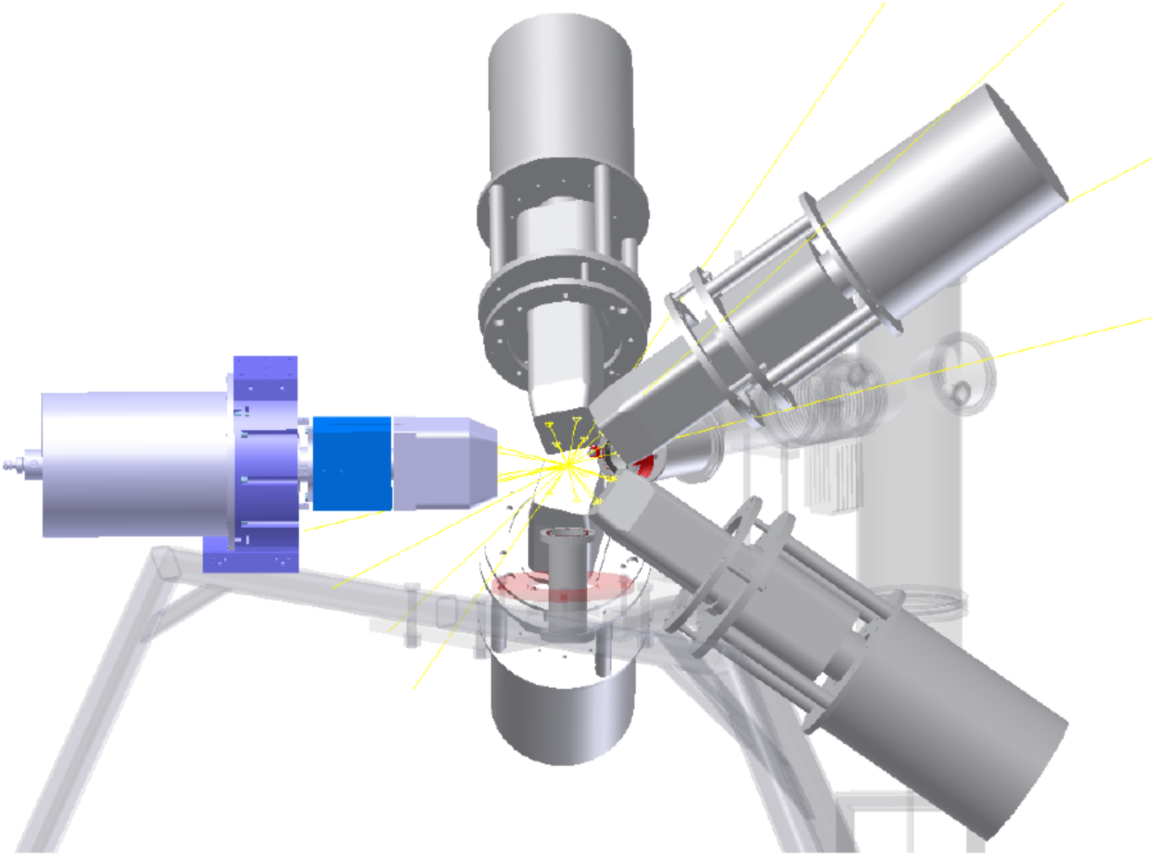

Figure 4.3: Schematic of the IDS set-up, including the four resident IDS detectors and the fifth TIGRESS detector as positioned during the experiment.

4.2.2 Auxiliary Detectors

To increase angular coverage and detection efficiency a fifth HPGe detector was placed off-axis in the horizontal plane of the beamline (shown in blue in Figure 4.3). The TIGRESS detector provided by IFIN-HH Bucharest is also a four-crystal clover detector, but features slightly larger tapered cylindrical crystals (60x60x90 mm)[60]. The capacity for β particle detection was also added to the IDS set-up by way of a plastic scintillator block surrounding the central tape. Two photomultiplier tubes were placed at opposite ends of the block, providing high detection efficiency for β decays from implanted isotopes. The block was coated in a white reflective paint to minimise signal losses, this can be seen in Figure 4.4. The scintillator block allows for $\beta - \gamma$ coincidence measurements with the HPGe detectors, which are useful for reducing background and contaminants in decay spectra.

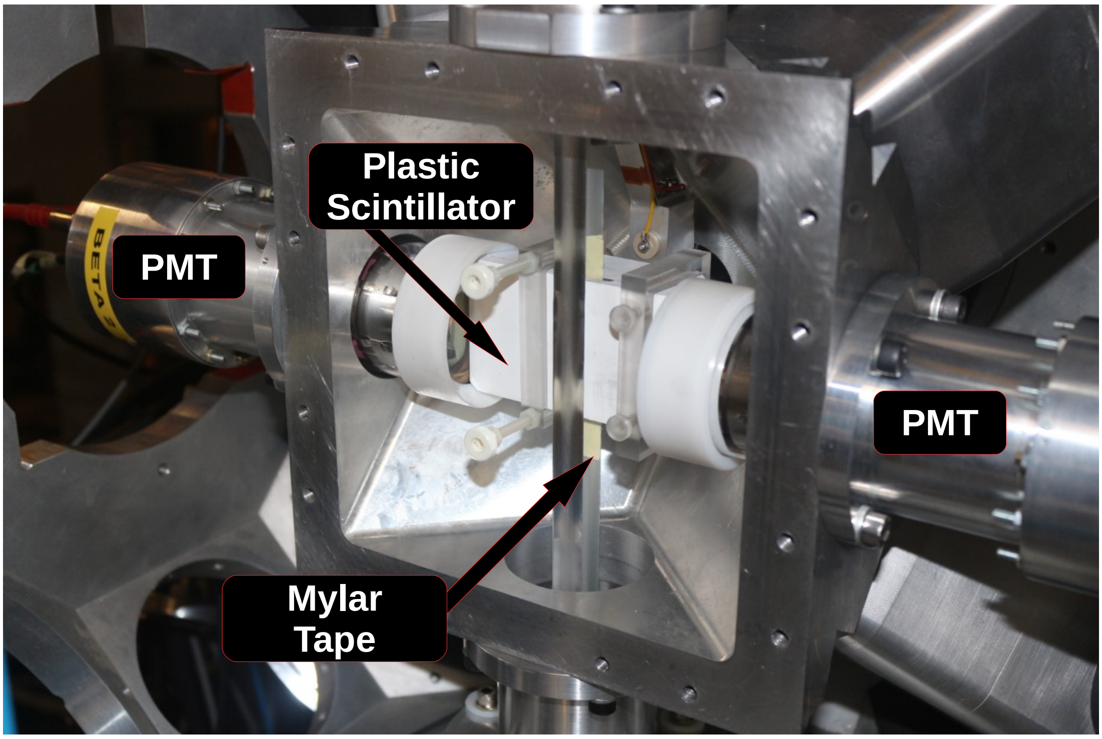

Figure 4.4: Close up of the detector set-up used in the experiment. The central scintillator block is placed surrounding the implantation region of the tape. Image taken from isolde-ids.web.cern.ch.

4.2.3 Electronics and Data Collection

Detectors in the IDS set-up send their signals through a gain and offset unit, which is then passed to a channel in the IDS Nutaq digitiser. Data acquisition and other aspects of the experiment were controlled using the IDS acquisition PC and the MIDAS (Multi Instance Data Acquisition System) software. The set-up resembles the TDR (Total Data Readout) system used at the University of Jyväskylä for the GREAT (Gamma Recoil Electron Alpha Tagging) spectrometer [61]. Parameters and processes for event identification, building, and merging for each detector are controlled within MIDAS. On-line analysis was performed using the integrated software Grain [62], and subsequent off-line analysis was conducted using GASPWare and ROOT [63].

Chapter 5

Analysis and Results

5.1 Data Sorting

In list mode, the MIDAS run files consist of single measurements with an amplitude, channel ID, and timestamp, which are combined in later analysis to construct coincidence events. These files are sorted offline by Grain [62] using sort codes into histograms specified by the users. During the sort, energy calibrations and configurations are applied which include conditional parameters such as coincidence time gates. For these data a γ coincidence time gate of 1 μs was used for all events, triggering on all detector channels. Add-back, as described in Section 2.3.2, was implemented for all germanium detectors which mitigated the effects of Compton scattering and increased efficiency, particularly for high energy γ rays. For the GASPWare analysis, sort codes were used to generate 1D (γ singles), 2D ($\gamma - \gamma$) and ($\beta - \gamma$), and 3D ($\beta - \gamma - \gamma$ and $\gamma - \gamma - \delta t$) histograms. These were then viewed and analysed using GASPWare software [64].

5.2 Data Calibrations

5.2.1 Energy Calibration

The energy calibration was performed using a 15 kBq ^{152}Eu source run lasting 1.46 hours. A total of 12 peaks were used from this spectrum (121.8, 244.7, 344.3, 411.1, 444.0, 778.9, 964.1, 1085.9, 1089.7, 1112.1, 1299.1, and 1408.0 keV [65]). These peaks were fitted for each of the resident HPGe crystals and the TIGRESS detector crystals. A quadratic fit was then applied to the data to determine the calibration parameters.

5.2.2 Efficiency Calibration

The efficiency calibration for this dataset was carried out using the same ^{152}Eu run. Using known information about the source and the length of the run, the total intensity of the characteristic ^{152}Eu peaks can be calculated. From this, the detector efficiency at each peak energy can be determined. These efficiencies were then plotted against energy, and fitted with the multiparameter function shown in equation 5.1 [66]:

$$\epsilon(E_\gamma) = \frac{1}{E_\gamma}(A_0 + A_1 ln(E_\gamma) + A_2 ln(E_\gamma)^2 + A_3 ln(E_\gamma)^3 + A_4 ln(E_\gamma)^5) \tag{5.1}$$

This function was selected as it reproduces both the rapid drop off of detection efficiency below $\sim$100 keV, as well as the steady decline with increasing energy. The strong ^{152}Eu peaks are only found below 1.5 MeV, as such, using these peaks for efficiency calibrations results in substantially lower accuracy at higher energies due to the lack of data points. Therefore, a well-studied, high energy peak is necessary to limit this effect. The 583 keV and 2614.5 keV peaks in ^{208}Pb which are emitted following the β^- decay of ^{208}Tl fulfil these requirements. Thus, using data collected for A=208, the known peak ratio of these γ rays was used to extend the calibration up to 2.6 MeV. The values used for the calibration, as well as the efficiency fit for the detector array can be seen in Figure 5.1.

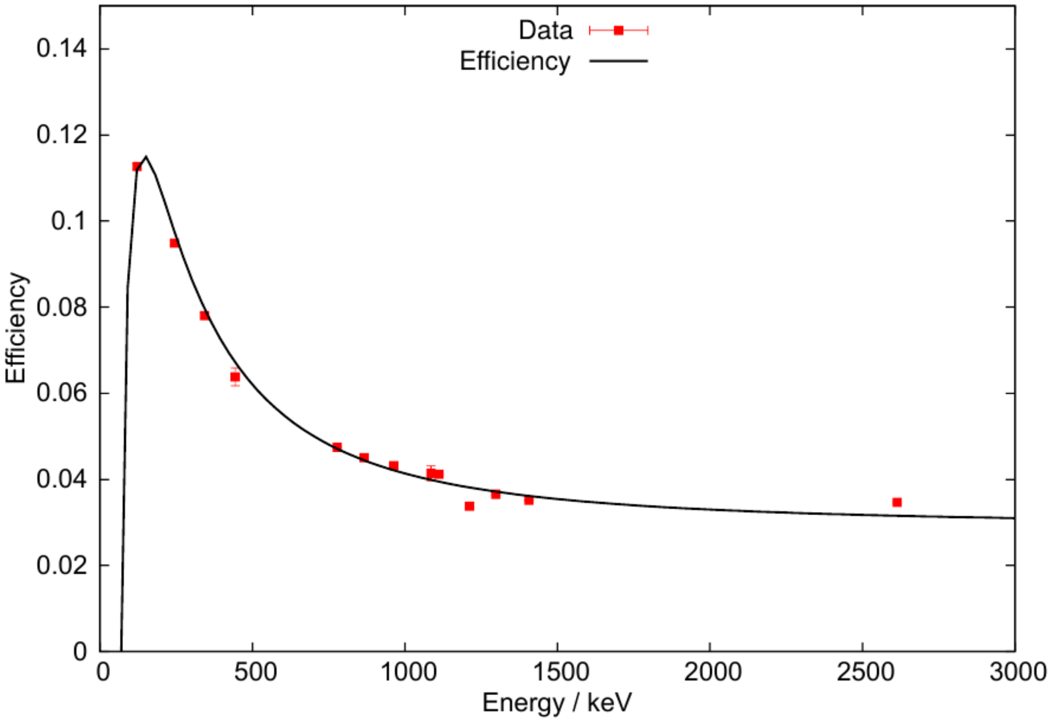

Figure 5.1: Full γ-ray energy peak detection efficiency, including add-back, for the HPGe detectors using data from the ^{152}Eu decay run and the 2614.5 keV ^{208}Pb peak.

5.3 Dataset

5.3.1 Statistics

The clarity of γ-coincidence spectra is dependent on a number of factors including detector resolution, overlap with similar peak energies, accuracy of background subtraction, and, most crucially, number of counts in the gated peak. Despite the limitations of the data collected, a $\gamma - \gamma$ matrix with a high level of statistics was generated. The full projection of this $\gamma - \gamma$ matrix is presented in Figure 5.2.

The majority of visible peaks in the spectrum are the result of internal decays in ^{208}Po, following the β^+/EC decay of ^{208}At [3]. Due to their high intensity, many of the peaks visible in the full $\gamma - \gamma$ projection have been observed in previous decay studies. There are however a number of γ rays visible in Figure 5.2 which, although observed in prior experiments, were not placed into the ^{208}Po level scheme due to insufficient statistics. Unsurprisingly, the vast

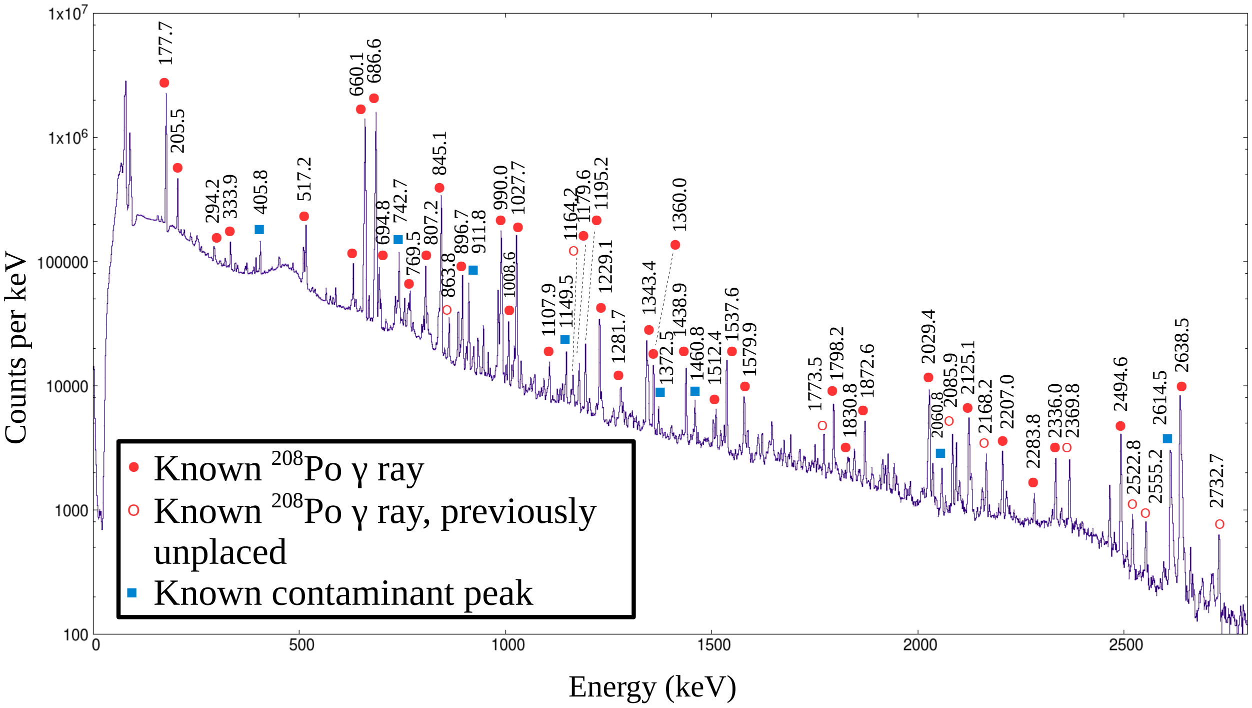

Figure 5.2: Full $\gamma - \gamma$ projection (1μs coincidence window) for all A=208 data collected. Peak energies are given for known ^{208}Po γ rays (filled red circle), known ^{208}Po but previously unplaced γ rays (unfilled red circle), and known contaminant peaks (filled blue square). The contaminant peaks featured result from decays in ^{207}Bi, as well as strong background peaks (^{40}K at 1460.8 keV and ^{208}Tl at 2614.5 keV).

majority of the unplaced transitions visible in the full $\gamma - \gamma$ projection are $>$2 MeV, as γ-ray detection efficiency is much lower at these energies. The large HPGe cluster detectors in place at the IDS have better detection efficiency than the smaller Ge(Li) used in the previous ^{208}At β^+ decay experiment [5] which provides greater statistics for higher energy photons ($\sim 10^3$ counts).

5.3.2 Contaminants

The general purpose separator was selected over the high resolution separator as it allowed for greater statistics with a minimal loss in mass resolution due to the high mass involved. As a consequence the A=208 radioactive beam features several A$\sim$208 contaminants, the decays of which can complicate coincidence analysis if left unidentified. The most abundant beam contaminant observed in this analysis is ^{207}Po which EC/β^+ decays to ^{207}Bi and is prevalent enough to be visible in the full projection in Figure 5.2. This decay can be attributed to the majority of labelled contaminant peaks in Figure 5.2 (405.8, 742.7, 911.8, 1148.5, 1372.5, and 2060.8 keV [25]). Transitions that result from the subsequent decay of ^{207}Bi were also observed in gated spectra. The two other labelled contaminant peaks visible in the full projection, 1460.8 keV and 2614.5 keV, can be attributed to decays of ^{40}K and ^{208}Tl respectively [67]. These peaks are typical for γ spectra in this mass region, and although only the 2614.5 keV peak is visible in Figure 5.2, other γ rays from the ^{208}Tl decay chain will also feature in the dataset in gated spectra. gamma rays which result from internal decays of ^{208}Tl following the β^- decay of ^{208}Hg can also be observed in some gated spectra.

5.3.3 Electron Conversion Coefficients

Electron conversion coefficients are inversely related to γ-ray energy (see equations 2.10 and 2.11). Consequently, conversion coefficients were only considered for transitions with energies $<$1 MeV. The only exception to this being the 1028 keV transition as its high intensity makes the effect of conversion electrons non-negligible. A large proportion of internal conversion coefficients of transitions in ^{208}Po have been measured in previous analysis. This includes a number of transitions identified as decays of ^{208}Po but not placed in the level scheme [4, 46, 68]. These coefficients were incorporated into this analysis to calculate $I_{\gamma+IC,rel}$ values for relevant transitions. Where experimental values were not available, theoretical internal conversion coefficients were determined using the BrIcc code [69]. Electron conversion coefficients are dependent on multipolarity, transitions with energies below 1 MeV are unlikely to have multipolarity of order greater than E2 with the exception of isomers. Consequently, where multipolarity was unknown, an average of the calculated internal conversion coefficients for E1, M1, and E2 was used, with sufficient uncertainty to cover all three possibilities.

5.4 ^{208}Po Level Scheme

Figure 5.3 shows the final level scheme presented in this work, with a full list of levels and transitions given in Table 5.1. This level scheme was compiled using energy gating on $\gamma - \gamma$ coincidence spectra, with $\gamma - \gamma - \delta t$ matrices utilised to identify transitions to the 1528 keV isomeric state ($t_{1/2}$ = 377(9) ns [70]). beta-gamma-gamma spectra were also generated but due to the lower detection efficiency of scintillator detectors for EC decays (the process by which ^{208}At predominantly decays) these spectra had insufficient statistics to provide insight beyond that of the $\gamma - \gamma$ spectra. Therefore, no β-coincident $\gamma - \gamma$ gated spectra appear in these results.

The relative intensities, shown by the arrow thickness in Figure 5.3 for the highest intensity γ rays and detailed in Table 5.1, were obtained from analysis of the peaks. For lower intensity transitions this was determined through coincidence relationships and comparison with other peaks of known intensity. From this, relative intensities ranging from 0.01-100 were measured. Due to the large spin change between the ground states of ^{208}At and ^{208}Po, a gamma-normalisation factor of 1.0 can be applied to obtain photon intensities per 100 β^+/EC decays. Spin-parities were determined through a combination of γ-ray placements and multipolarities, and restrictions resulting from β decay selection rules and logft limits [23]. For transitions with no measured α_K value, E1, M1, and E2 multipolarities were considered, with M2 and E3 transitions for high energies (>1 MeV). The latter of which is justified by the strong octupole collectivity in the region.

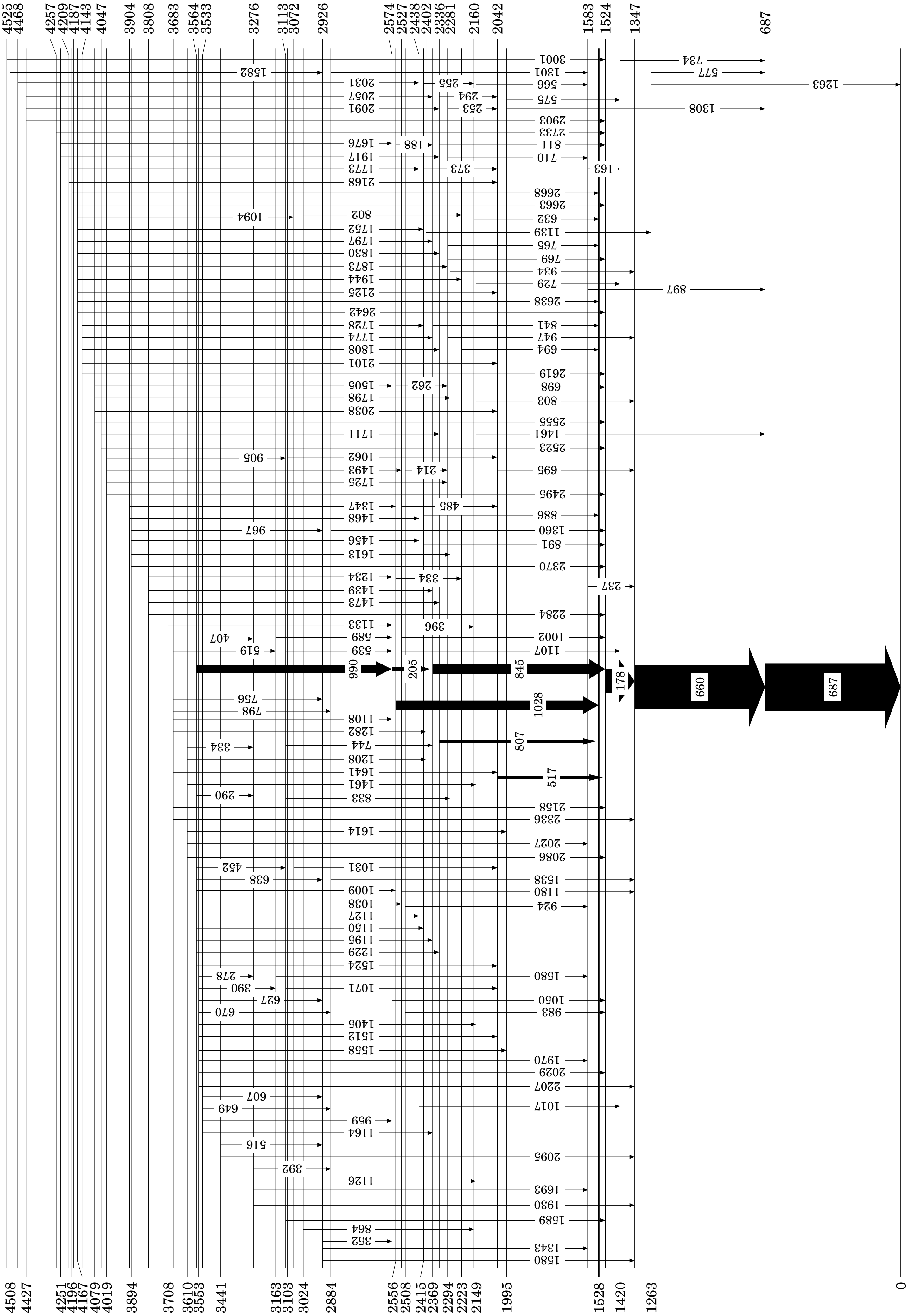

Figure 5.3: Level scheme for ^{208}Po observed in this work. Energies of levels and transitions are given in keV. Relative intensities of the most intense transitions are indicated by arrow thickness.

Table 5.1: Full list of levels and transitions observed in ^{208}Po in this analysis. New states are indicated in bold. New, assigned, and (re)assigned gamma rays are indicated by x, y, and z superscripts respectively. The energies and spin-parities of the intial and final states ($E_{i/f}$ and $J^{\pi}_{i/f}$) are given. In addition E_γ is the measured energy of the transition. Multipolarities, where possible, have been taken from ref. [3], which are based on previous conversion electron coefficient measurements from refs. [4, 46, 68]. When spin-parities are not firmly established from experimental considerations, the assignment favoured by shell model calculations is shown in bold. References to Nucl. Data Sheet compilations (ref. [3]) are provided for the spin-parities of states which have been observed in non-beta-decay studies. For instances where levels have only been observed previously in beta-decay studies, all information relevant to their spin-parity assignments is provided in this table. The relative intensities ($I_{\gamma,rel.}$ and $I_{\gamma+IC,rel.}$) are are given for each γ-ray both with and without internal electron conversion, with respect to 100 for the combined intensities of γs to the ground state (with IC). The last column contains additional information needed for the spin-parity assignments.

E_i / keV	J^{π}_i	E_f / keV	J^{π}_f	E_γ / keV	σL	$I_{\gamma,rel.}$	$I_{\gamma+IC,rel.}$	Comment
686.6(2)	2^+[3]	0.0	0^+	686.6(2)	E2[3]	98(10)	100(10)	-
1263.2(3)	2^+[3]	686.6(2)	2^+	576.7(3)	M1(+E2)[3]	0.35(9)	0.38(9)	-
		0.0	0^+	1263.0(2)	E2[3]	0.15(1)	0.15(1)	
1346.7(3)	4^+[3]	686.6(2)	2^+	660.1(2)	E2[3]	92(8)	93(8)	-
1420.3(3)	3^+[3]	686.6(2)	2^+	733.7(3)	M1+E2[3]	1.4(3)	1.4(3)	-
1524.4(3)	6^+[3]	1346.7(3)	4^+	177.7(2)	E2[3]	50(3)	87(4)	-
1528.3(5)	8^+[3]	1524.4(3)	6^+	3.9(4)$^{a)}$	E2[71, 72]	-	40(2)$^{a)}$	-
1583.4(3)	4^+[3]	1420.3(3)	3^+	163.3(3)	-	0.16(4)	0.46(21)	-
		1346.7(3)	4^+	236.8(2)	M1(+E2)[3]	0.35(5)	0.69(10)	
		686.6(2)	2^+	896.6(2)	E2[3]	4.8(2)	4.8(2)	
1995.2(4)	3^-	1420.3(3)	3^+	575.3(3)	-	0.40(7)	0.41(8)	Populated from 3554 and 3610 keV 5^- states
		686.6(2)	2^+	1308.2(2)	E1(+M2)[3]	0.22(1)	0.22(1)	
2041.6(4)	6^+[3]	1524.4(3)	6^+	517.2(2)	M1(+E2)[3]	6.3(4)	7.0(4)	Populated by M1[3] 294 keV transition from 2336 keV 7^+ state
		1346.7(3)	4^+	^{z}694.8(3)	-	2.5(4)	2.5(4)	
2149.1(4)	3^+, $\mathbf{4^+}$	1583.4(3)	4^+	566.1(2)	M1+E2[3]	0.75(3)	0.80(4)	-
		1420.3(3)	3^+	^{z}729.2(3)	-	0.38(6)	0.39(6)	
		1346.7(3)	4^+	802.6(2)	-	0.40(6)	0.42(6)	
		686.6(2)	2^+	^{x}1461.5(3)	-	0.57(5)	0.57(5)	
2160.3(5)	8^+[3]	1528.3(5)	8^+	631.9(2)	M1(+E2)[3]	3.7(4)	3.9(4)	-
2222.6(4)	8^+	2160.3(5)	8^+	^{x}62.3(9)$^{a)}$	-	-	0.45(34)$^{a)}$	See text
		1528.3(5)	8^+	^{z}694.3(2)	M1*	1.9(2)	2.0(2)	
		1524.4(3)	6^+	^{z}698.2(2)	E2[3]	1.24(7)	1.27(9)	
2280.8(3)	5^+	1346.7(3)	4^+	934.1(2)	M1+E2[3]	0.95(6)	0.97(6)	Populated from 3113 keV $5^-, 6^-$ state, J^π values limited by β^+ population

Table 5.1 – *Continued.*

E_i / keV	J_i^π	E_f / keV	J_f^π	E_γ / keV	σL	$I_{\gamma,rel.}$	$I_{\gamma+IC,rel.}$	Comment
2293.8(4)	6^+[3]	2041.6(4)	6^+	252.5(2)	-	0.62(6)	0.93(24)	-
		1583.4(3)	4^+	710.5(2)	-	0.65(2)	0.66(2)	
		1528.3(5)	8^+	765.2(3)	-	0.13(7)	0.14(7)	
		1524.4(3)	6^+	769.5(2)	M1(+E2)[3]	2.1(2)	2.2(2)	
		1346.7(3)	4^+	947.0(2)	E2[3]	1.60(4)	1.61(4)	
2335.7(5)	7^+[3]	2041.6(4)	6^+	294.2(2)	M1[3]	0.99(7)	1.53(11)	-
		1528.3(5)	8^+	807.2(2)	M1(+E2)[3]	6.2(2)	6.4(2)	
		1524.4(3)	6^+	811.4(2)	M1+E2[3]	1.22(7)	1.25(7)	
2369.3(4)	7^-[3]	1528.3(5)	8^+	840.8(4)	E1[3]	3.0(3)	3.0(3)	-
		1524.4(3)	6^+	845.1(2)	E1[3]	21.1(7)	21.1(7)	
2402.1(5)	$3^-,4^+$	1263.2(3)	2^+	^{y}1139.0(4)	E1,E2[3]	0.5(2)	0.5(2)	Populated from 3610 keV 5^- state and 3683 $5^-,6^-$ state
2415.0(5)	$\mathbf{7}^+,8^+$	2160.3(5)	8^+	254.8(3)	-	0.32(4)	0.48(14)	Populated from 3565 keV 6^- state
		2041.6(4)	6^+	373.4(2)	-	0.71(4)	0.80(12)	
		1528.3(5)	8^+	886.3(2)	M1+E2[3]	2.95(9)	3.02(9)	
		1524.4(3)	6^+	^{x}890.8(3)	-	0.47(4)	0.47(4)	
2437.6(4)	5^+	1420.3(3)	3^+	^{y}1017.2(2)	E2*	0.77(6)	0.78(6)	See text
2507.7(3)	$5^+,\mathbf{6}^+$	2293.8(4)	6^+	214.1(3)	M1+E2[3]	0.28(5)	0.59(12)	-
		1583.4(3)	4^+	^{z}924.2(2)	-	0.57(5)	0.58(6)	
		1524.4(3)	6^+	983.2(2)	M1+E2[3]	4.7(2)	4.7(2)	
2526.7(4)	5^+	2041.6(4)	6^+	485.0(2)	M1[3]	0.44(5)	0.50(6)	-
		1524.4(3)	6^+	1002.2(2)	M1(+E2)[3]	0.45(2)	0.46(2)	
		1420.3(3)	3^+	^{x}1106.9(3)	-	0.30(3)	0.30(3)	
		1346.7(3)	4^+	1179.6(2)	M1(+E2)[3]	1.05(4)	1.05(4)	
2556.5(5)	7^+[3]	2369.3(4)	7^-	^{y}188.2(2)	-	0.5(2)	0.5(2)	-
		2293.8(4)	6^+	262.0(3)	M1(+E2)[3]	0.38(6)	0.62(13)	
		2222.6(4)	8^+	^{z}333.9(3)	M1(+E2)[3]	2.5(5)	2.9(9)	
		2160.3(5)	8^+	396.2(3)	M1+E2[3]	1.16(2)	1.41(4)	
		1528.3(5)	8^+	1027.7(2)	M1+E2[3]	19.4(7)	19.7(7)	
2574.8(4)	$\mathbf{6}^-,7^-$[3]	2369.3(4)	7^-	205.5(2)	M1(+E2)[3]	7.9(4)	19.4(9)	-
		1524.4(3)	6^+	^{x}1050.3(2)	-	0.26(3)	0.26(3)	
2863.0(4)	$3^-,4,5,6^+$	2402.1(5)	$3^-,4^+$	^{x}460.9(3)	-	0.23(7)	0.24(8)	Populated from 3553 and 3610 keV 5^- states
		1583.4(3)	4^+	^{y}1279.62(2)	-	0.87(7)	0.87(7)	
2884.5(3)	5^-	1583.4(3)	4^+	^{z}1301.2(3)	-	0.12(3)	0.12(3)	-
		1524.4(3)	6^+	1360.0(2)	E1[3]	0.99(1)	0.99(1)	
		1346.7(3)	4^+	1537.6(2)	E1[3]	1.52(5)	1.52(5)	

Table 5.1 – *Continued.*

E_i / keV	J_i^π	E_f / keV	J_f^π	E_γ / keV	σL	$I_{\gamma,rel.}$	$I_{\gamma+IC,rel.}$	Comment
2926.6(4)	5^-	2574.8(4)	$6^-,7^-$	^{x}351.7(4)	-	0.31(7)	0.35(11)	M1+E2 [3] (638 keV) transition from 3565 keV 6^- state
		1583.4(3)	4^+	1343.4(2)	E1[3]	2.46(8)	2.46(8)	
		1346.7(3)	4^+	^{x}1579.9(4)	-	0.4(2)	0.4(2)	
3024.2(5)	$6^+,7,8^-$	2222.6(4)	8^+	^{x}801.6(3)	-	0.48(8)	0.48(9)	J^π values limited by β^+ population
		2160.3(5)	8^+	^{y}863.8(2)	-	0.42(4)	0.42(4)	
3072.5(4)	$6^-,7^-,8^-$	2041.6(4)	6^+	^{x}1030.9(3)	-	0.32(5)	0.32(5)	M1(+E2)[3] transition from 4167 keV 7^- state
3103.8(4)	$4^-,5,6,7,8^-$	2041.6(4)	6^+	^{y}1062.2(3)	-	0.10(3)	0.10(3)	J^π values limited by β^+ population
3113.3(5)	$5^-,6^-$	2574.8(4)	$6^-,7^-$	538.6(3)	M1+E2[3]	0.30(7)	0.32(7)	-
		2369.3(4)	7^-	^{x}744.0(3)	-	0.26(7)	0.27(7)	
		2280.8(3)	5^+	^{z}832.6(7)	-	0.06(6)	0.06(6)	
		2041.6(4)	6^+	1071.4(3)	-	0.25(4)	0.25(4)	
		1524.4(3)	6^+	1588.8(2)	-	0.24(1)	0.24(1)	
3163.7(5)	$4^-,5^-,6^-$	2574.8(4)	$6^-,7^-$	^{x}588.9(4)	-	0.6(2)	0.6(2)	M1(+E2)[3] from 3554 keV 5^- state
		1583.4(3)	4^+	^{y}1580.3(4)	-	0.31(8)	0.31(8)	
3276.0(5)	$4^-,5,6,7^-$	2884.5(3)	5^-	^{x}391.6(3)	-	0.14(4)	0.16(5)	See text
		2149.1(4)	$3^+,4^+$	^{x}1126.2(5)	-	0.24(8)	0.24(8)	
		1583.4(3)	4^+	^{y}1692.8(3)	-	0.32(5)	0.32(5)	
		1346.7(3)	4^+	^{y}1929.8(4)	-	0.20(4)	0.20(4)	
3441.8(5)	$4^-,5^-,6^+$	2926.6(4)	5^-	^{x}515.5(4)	-	0.33(5)	0.35(7)	J^π values limited by β^+ population
		1346.7(3)	4^+	^{z}2094.8(2)	E1,E2[3]	0.30(4)	0.30(4)	
3533.6(4)	$5^-,6^-,7^-$	2926.6(4)	5^-	^{x}606.7(3)	-	0.12(3)	0.12(3)	-
		2884.5(3)	5^-	^{x}649.4(3)	-	0.17(3)	0.18(4)	
		2574.8(4)	$6^-,7^-$	^{y}958.9(2)	M1(+E2)[3]	0.71(8)	0.73(9)	
		2369.3(4)	7^-	^{y}1164.2(3)	-	0.37(6)	0.37(6)	
3553.9(4)	5^-	3276.0(5)	$4^-,5,6,7^-$	^{x}278.5(4)	-	0.15(7)	0.19(11)	-
		3163.7(5)	$4^-,5^-,6^-$	^{z}390.3(2)	M1(+E2)[3]	0.48(9)	0.53(13)	
		2926.6(4)	5^-	627.1(2)	M1(+E2)[3]	0.29(4)	0.31(4)	
		2884.5(3)	5^-	669.5(2)	M1(+E2)[3]	1.32(3)	1.38(5)	
		2863.0(4)	$3^-,4,5,6^+$	^{x}691.2(1)	-	0.34(2)	0.34(3)	
		2149.1(4)	$3^+,4^+$	^{x}1404.6(4)	-	0.24(6)	0.24(6)	
		2041.6(4)	6^+	^{z}1512.4(3)	E1[3]	0.24(3)	0.24(3)	
		1995.2(4)	3^-	^{x}1558.2(5)	-	0.3(2)	0.3(2)	
		1583.4(3)	4^+	1970.3(2)	-	0.12(1)	0.12(1)	
		1524.4(3)	6^+	2029.4(2)	E1[3]	1.30(6)	1.30(6)	
		1346.7(3)	4^+	2207.0(2)	E1[3]	0.41(3)	0.41(3)	

Table 5.1 – *Continued.*

E_i / keV	J_i^π	E_f / keV	J_f^π	E_γ / keV	σL	$I_{\gamma,rel.}$	$I_{\gamma+IC,rel.}$	Comment
3564.8(4)	6^-	3276.0(5)	$4^-,5,6,7^-$	^{x}289.6(10)	-	0.1(1)	0.1(1)	-
		3113.3(5)	$5^-,6^-$	451.7(4)	M1(+E2)[3]	0.6(3)	0.7(3)	
		2926.6(4)	5^-	^{z}638.1(2)	M1+E2[3]	0.34(4)	0.35(5)	
		2574.8(4)	$6^-,7^-$	990.0(2)	M1(+E2)[3]	16.3(5)	16.6(5)	
		2556.5(5)	7^+	1008.6(2)	E1[3]	1.92(6)	1.92(6)	
		2526.7(4)	5^+	1038.1(3)	(E1+M2)[3]	0.52(3)	0.52(3)	
		2437.6(4)	5^+	^{z}1126.9(4)	E1*	0.12(5)	0.12(5)	
		2415.0(5)	$7^+,8^+$	^{x}1149.5(3)	-	1.2(3)	1.2(3)	
		2369.3(4)	7^-	1195.2(2)	M1+E2[3]	1.86(4)	1.86(4)	
		2335.7(5)	7^+	1229.1(2)	E1[3]	2.5(2)	2.5(2)	
		2041.6(4)	6^+	1523.5(3)	-	0.07(2)	0.07(2)	
3610.1(4)	5^-	3276.0(5)	$4^-,5,6,7^-$	^{x}334.1(7)	-	0.2(2)	0.3(2)	-
		2863.0(4)	$3^-,4,5,6^+$	^{y}747.4(1)	-	0.62(6)	0.63(7)	
		2402.1(5)	$3^-,4^+$	^{x}1208.3(2)	-	0.21(3)	0.21(3)	
		2149.1(4)	$3^+,4^+$	^{x}1460.6(2)	-	0.70(6)	0.70(6)	
		1995.2(4)	3^-	^{x}1614.4(3)	-	0.37(9)	0.37(9)	
		1583.4(3)	4^+	^{y}2026.7(2)	E1*	0.61(4)	0.61(4)	
		1524.4(3)	6^+	^{y}2085.9(2)	E1[3]	0.55(4)	0.55(4)	
3682.6(4)	$5^-,6^-$	3276.0(5)	$4^-,5,6,7^-$	^{x}406.5(3)	-	0.4(2)	0.5(2)	-
		3163.7(5)	$4^-,5^-,6^-$	^{x}518.9(4)	-	0.4(2)	0.5(2)	
		2926.6(4)	5^-	755.5(2)	M1(+E2)[3]	1.30(2)	1.35(2)	
		2884.5(3)	5^-	798.2(2)	M1(+E2)[3]	0.75(6)	0.78(6)	
		2863.0(4)	$3^-,4,5,6^+$	^{x}820.0(4)	-	0.15(4)	0.15(4)	
		2574.8(4)	$6^-,7^-$	1107.9(3)	M1+E2[3]	0.54(8)	0.54(8)	
		2402.1(5)	$3^-,4^+$	^{z}1281.7(3)	-	0.19(3)	0.19(3)	
		2041.6(4)	6^+	1640.6(5)	E1[3]	0.12(4)	0.12(4)	
		1524.4(3)	6^+	2157.8(6)	-	0.14(5)	0.14(5)	
		1346.7(3)	4^+	2336.0(3)	-	0.38(4)	0.38(4)	
3708.0(5)	$5^-,6^-,7^-,8^-$	2574.8(4)	$6^-,7^-$	^{y}1133.2(4)	M1+E2[3]	0.36(10)	0.36(10)	-
3744.5(5)	$5^-,6,7,8^-$	2160.3(5)	8^+	^{z}1584.2(2)	-	0.07(1)	0.07(1)	J^π values limited by β^+ population
3808.4(4)	$6^-,7^-$	2574.8(4)	$6^-,7^-$	1233.9(3)	-	0.42(6)	0.42(6)	J^π values limited by β^+ population and logft
		2369.3(4)	7^-	1438.9(2)	M1+E2[3]	1.26(7)	1.26(7)	
		2335.7(5)	7^+	1472.7(6)	-	0.03(2)	0.03(2)	
		1524.4(3)	6^+	2283.8(3)	-	0.10(2)	0.10(2)	
3893.9(4)	$4^-,5,6,7^-$	2926.6(4)	5^-	^{x}967.0(4)	-	0.03(2)	0.03(2)	J^π values limited by β^+ population
		2437.6(4)	5^+	^{y}1456.3(4)	-	0.4(2)	0.4(2)	
		2280.8(3)	5^+	^{y}1613.2(3)	-	0.03(1)	0.03(1)	
		1524.4(3)	6^+	^{y}2369.8(2)	-	0.36(2)	0.36(2)	
3904.3(6)	$4^-,5,6,7,8^-$	2556.5(5)	7^+	^{x}1346.7(2)	-	0.28(2)	0.28(2)	-
		2437.6(4)	5^+	^{y}1467.9(10)	-	0.08(4)	0.08(4)	

Table 5.1 – *Continued.*

E_i / keV	J_i^π	E_f / keV	J_f^π	E_γ / keV	σL	$I_{\gamma,rel.}$	$I_{\gamma+IC,rel.}$	Comment
4018.9(5)	$5,6,7$	3113.3(5)	$5^-,6^-$	^{x}905.2(4)	-	0.5(3)	0.6(3)	J^π values limited by β^+ population and logft
		2526.7(4)	5^+	^{x}1492.8(8)	-	0.05(4)	0.05(4)	
		2293.8(4)	6^+	1725.0(2)	-	0.02(1)	0.02(1)	
		1524.4(3)	6^+	2494.6(2)	-	0.73(3)	0.73(3)	
4046.8(5)	$4^-,5,6,7,8^-$	2335.7(5)	7^+	^{x}1710.8(4)	-	0.03(1)	0.03(1)	J^π values limited by β^+ population
		1524.4(3)	6^+	^{y}2522.8(4)	-	0.12(3)	0.12(3)	
4079.4(4)	$5,6,7$	2574.8(4)	$6^-,7^-$	^{x}1504.8(3)	-	0.35(6)	0.35(6)	J^π values limited by β^+ population and logft
		2280.8(3)	5^+	^{x}1798.3(4)	-	0.02(1)	0.02(1)	
		2041.6(4)	6^+	^{y}2037.8(2)	-	0.15(1)	0.15(1)	
		1524.4(3)	6^+	^{y}2555.2(4)	-	0.12(2)	0.12(2)	
4143.2(5)	$5,6,7$	2415.0(5)	$7^+,8^+$	^{x}1728.0(3)	-	1.8(3)	1.8(3)	J^π values limited by β^+ population and logft
		2369.3(4)	7^-	^{y}1773.5(3)	-	0.34(4)	0.34(4)	
		2335.7(5)	7^+	^{x}1807.9(4)	-	0.03(1)	0.03(1)	
		2041.6(4)	6^+	^{y}2101.3(3)	-	0.04(1)	0.04(1)	
		1524.4(3)	6^+	^{y}2619.3(4)	-	0.21(3)	0.21(3)	
4166.6(5)	7^-	3072.5(4)	$6^-,7^-,8^-$	^{y}1094.4(3)	M1(+E2)[3]	0.32(5)	0.32(5)	-
		2415.0(5)	$7^+,8^+$	1751.7(4)	E1[3]	1.5(5)	1.5(5)	
		2369.3(4)	7^-	1796.9(2)	M1(+E2)[3]	0.69(1)	0.69(1)	
		2335.7(5)	7^+	1830.4(4)	-	0.03(1)	0.03(1)	
		2293.8(4)	6^+	1872.6(3)	E1[3]	0.19(3)	0.19(3)	
		2222.6(4)	8^+	^{y}1944.1(3)	-	0.12(3)	0.12(3)	
		2041.6(4)	6^+	2125.1(3)	E1[3]	0.46(5)	0.46(5)	
		1528.3(5)	8^+	2638.5(3)	-	1.70(9)	1.70(9)	
		1524.4(3)	6^+	2642.4(5)	-	0.47(4)	0.47(4)	
4187.2(4)	$4^-,5,6,7,8^-$	1524.4(3)	6^+	^{y}2662.7(3)	-	0.04(1)	0.04(1)	J^π values limited by β^+ population
4196.0(7)	$5^-,6,7,8^-$	1528.3(5)	8^+	^{z}2667.7(5)	-	0.04(1)	0.04(1)	J^π values limited by β^+ population
4209.1(4)	$5^+,6^+,7^+$	2437.6(4)	5^+	^{x}1772.5(4)	-	0.10(2)	0.10(2)	J^π values limited by β^+ population
		2041.6(4)	6^+	^{y}2168.2(2)	E2,M1[3]	0.21(1)	0.21(1)	
4251(1)	$4^-,5,6,7,8^-$	2574.8(4)	$6^-,7^-$	^{x}1675.8(5)	-	0.15(6)	0.15(6)	J^π values limited by β^+ population
		2335.7(5)	7^+	1916.8(3)	-	0.04(2)	0.04(2)	
4257.1(4)	$4^-,5,6,7,8^-$	1524.4(3)	6^+	^{y}2732.7(3)	-	0.09(1)	0.09(1)	J^π values limited by β^+ population
4426.9(6)	$5,6,7,8^-$	2369.3(4)	7^-	^{x}2057.4(6)	-	0.03(1)	0.03(1)	J^π values limited by β^+ population
		2335.7(5)	7^+	^{z}2091.3(6)	-	0.01(1)	0.01(1)	
		1524.4(3)	6^+	^{y}2902.6(4)	-	0.03(1)	0.03(1)	
4468.3(7)	$4^-,5,6,7,8^-$	2437.6(4)	5^+	^{x}2030.8(6)	-	0.10(5)	0.10(5)	J^π values limited by β^+ population
4508.2(5)	$4^-,5,6,7$	2926.6(4)	5^-	^{y}1581.5(4)	-	0.08(2)	0.08(2)	J^π values limited by β^+ population

Table 5.1 – *Continued.*

E_i / keV	J_i^π	E_f / keV	J_f^π	E_γ / keV	σL	$I_{\gamma,rel.}$	$I_{\gamma+IC,rel.}$	Comment
4524.9(6)	$4^-,5,6,7,8^-$	1524.4(3)	6^+	^{y}3000.5(5)	-	0.03(1)	0.03(1)	J^π values limited by β^+ population

[a)] This low energy γ ray was not observed directly. Its energy and intensity were determined from coincidence relationships.

[x] The gamma ray has been newly identified from this analysis.

[y] The gamma ray was observed in previous decay studies [3], and has been placed into the level scheme in this analysis.

[z] The gamma ray has been reassigned from its position in prior analysis [3].

[*] Measured conversion coefficient was taken from ref. [3], however the multipolarity was reinterpreted in this analysis.

The presented level scheme contains 27 new excited states and 43 new transitions which had not been previously identified. The majority of the previously reported states populated in β decay [3] are confirmed, however the previously suggested 3145 keV, 3202 keV, 3535 keV, and 4509 keV states were not observed and thus do not feature in the presented level scheme (note that the new 4508 keV state is based on different γ rays than the previous 4509 keV level). Newly-observed states in this analysis were significantly weighted towards higher energies, with 23 having energies $>$3 MeV, and 11 with energies exceeding 4 MeV. For newly observed transitions, nearly half (49%) have energies $>$1 MeV, however only two new transitions have energies $>$2 MeV. In addition to the expansion of the level scheme with new states and transitions, improvements have been made regarding known levels and ^{208}Po γ rays. Previous beta-decay studies identified a number of transitions which were attributed to ^{208}Po [3], however due to limitations in the dataset and analysis they were unable to place them in the level scheme. Of these unplaced transitions, 33 now feature in the level scheme presented in Figure 5.3, with a further 17 transitions reassigned from their previous positions in the level scheme. This equates to $\sim$45% of unplaced γ rays identified in previous decay studies. It is also worth noting that all previously-observed γ rays with relative intensity $>$0.35% have been placed in this analysis. The remaining unplaced transitions were investigated, but were either unobserved, or lacked sufficient statistics to achieve clean coincidence spectra with which to determine position. For many γ rays this lack of statistics was hindered further by proximity to neighbouring peaks, which obscured gated spectra. These unplaced transitions are expanded upon in Section 5.7.

Experimental log*ft* Values

Through a combination of information regarding the ground state decay of ^{208}At (Q_{EC} = 4999(9) [22], $J^{\pi} = 6^{+}$, $t_{1/2} = 1.63(3)$ *h* [3]), and the measured transition intensities, logft values were calculated for a number of states. These values are listed in Table 5.2, alongside the energy, spin-parity and β-population intensity of each state.

Table 5.2: Full list of levels observed in ^{208}Po in this analysis with newly observed states shown in **bold**. Spin-parity assignments are given alongside measured β population intensity percentages calculated using γ intensity imbalances (positive I_β% values denote states which are populated via β^+/EC decay, negative I_β% values should not occur as this would denote a state which is depopulating more than it is populating. Hence, in each case these intensities are less than their associated error). logft values are also given for all states with positive I_β% values which are not exceeded by their associated error.

Energy/keV	Spin-Parity/J$^\pi$	I_β%	logft
686.6(2)	2^+[3]	0(18)	-
1263.2(3)	2^+[3]	0.03(26)	-
1346.7(3)	4^+[3]	−4(11)	-
1420.3(3)	3^+[3]	−0.94(53)	-
1524.4(3)	6^+[3]	4(6)	-
1528.3(5)	8^+[3]	−1(4)	-
1583.4(3)	4^+[3]	−1(1)	-
1995.2(4)	3^-	0.02(29)	-
2041.6(4)	6^+	3.8(13)	7.75(1)
2149.1(4)	3^+, **4^+**	1.0(4)	-
2160.3(5)	8^+[3]	1.08(50)	-
2222.6(4)	8^+	0.22(89)	-
2280.8(3)	5^+	0.86(13)	8.32(7)
2293.8(4)	6^+[3]	4.13(57)	7.63(6)
2335.7(5)	7^+[3]	6.50(49)	7.41(4)
2369.3(4)	7^-	0.65(165)	-
2402.1(5)	3^-, **4^+**	0.02(28)	-
2415.0(5)	**7^+**, 8^+	0.33(125)	-
2437.6(4)	5^+	0.01(40)	-
2507.7(3)	5^+, **6^+**	5.91(20)	7.39(2)
2526.7(4)	5^+	1.74(21)	7.92(6)
2556.5(5)	7^+[3]	22.9(17)	6.78(13)
2574.8(4)	**6^-**, 7^-[3]	−0.75(155)	-
2863.0(4)	$3^-,4,5,6^+$	−0.01(28)	-
2884.5(3)	5^-	0.13(26)	-
2926.6(4)	5^-	0.62(47)	8.2(4)
3024.2(5)	$6^+,7,8^-$	0.91(13)	7.98(15)
3072.5(4)	$6^-,7^-,8^-$	0.00(11)	-
3103.8(4)	$4^-,5,6,7,8^-$	0.10(3)	8.9(14)
3113.3(5)	$5^-,6^-$	-0.07(71)	-
3163.7(5)	$4^-,5^-,6^-$	−0.05(50)	-
3276.0(5)	$4^-,5,6,7^-$	−0.13(66)	-
3441.8(5)	$4^-,5^-,6^+$	0.65(9)	7.90(7)
3533.6(4)	$5^-,6^-,7^-$	1.39(20)	7.52(7)
3553.9(4)	5^-	5.31(60)	6.95(6)
3564.8(4)	6^-	25.9(15)	6.20(2)

Energy/keV	Spin-Parity/J$^\pi$	I_β%	logft
3610.1(4)	5^-	3.28(43)	7.10(6)
3682.6(4)	$5^-,6^-$	4.46(64)	6.91(7)
3708.0(5)	$5^-,6^-,7^-,8^-$	0.36(10)	7.99(13)
3744.5(5)	$5^-,6,7,8^-$	0.07(1)	8.67(7)
3808.4(4)	$6^-,7^-$	1.80(16)	7.21(5)
3893.9(4)	$4^-,5,6,7^-$	0.79(16)	7.5(1)
3904.3(6)	$4^-,5,6,7,8^-$	0.37(12)	7.82(15)
4018.9(5)	$5,6,7$	1.35(28)	7.10(12)
4046.8(5)	$4^-,5,6,7,8^-$	0.15(4)	8.08(12)
4079.4(4)	$5,6,7$	0.64(10)	7.41(8)
4143.2(5)	$5,6,7$	2.38(33)	6.77(7)
4166.6(5)	7^-	5.43(81)	6.39(8)
4187.2(4)	$4^-,5,6,7,8^-$	0.04(1)	8.50(12)
4196.0(7)	$5^-,6,7,8^-$	0.04(1)	8.49(12)
4209.1(4)	$5^+,6^+$	0.31(4)	7.58(7)
4251(1)	$4^-,5,6,7,8^-$	0.19(8)	7.74(19)
4257.1(4)	$4^-,5,6,7,8^-$	0.09(1)	8.05(6)
4426.9(6)	$5,6,7,8^-$	0.07(3)	7.9(2)
4468.3(7)	$4^-,5,6,7,8^-$	0.10(5)	7.66(23)
4508.2(5)	$4^-,5,6,7$	0.08(2)	7.68(13)
4524.9(6)	$4^-,5,6,7,8^-$	0.03(1)	8.07(16)

logft values were calculated for every instance where the value for β-population intensity exceeded the error bar regardless of degrees of forbiddenness. As forbidden decays are more prevalent in this region of the nuclide chart, this was done to avoid underestimation of population via decays with higher degrees of forbiddenness.

The high proportion of first-forbidden decays mitigates the utility of comparisons with shell model calculations as they are less conclusive due to the difficulties in simulating forbidden decays. Nevertheless, logft values can still provide insight when determining spin-parity, through comparison with known logft ranges [23]. States where the spin-parity has been limited by its logft value are indicated in Table 5.1.

5.5 Establishing States and Transitions

The following sections detail states and transitions of interest including: low energy, new or confirmed states, high intensity reassigned transitions, and additional explanations of atypical and/or anomalous results where appropriate.

5.5.1 Confirmed States

Previous decay spectroscopy experiments tentatively identified three low-lying levels in ^{208}Po at 1995.46 keV, 2149.43 keV and 2280.62 keV [46]. The uncertainty of these states was the result of the limited number of γ rays observed to populate/depopulate each level, making it difficult to generate coincidence spectra to confirm the placement. To verify these states and the transitions relating to them, coincidence spectra were generated for transitions populating and depopulating each level. Figures 5.4, 5.5, and 5.6 show coincidence spectra for 934 keV, 566 keV and the 1460 keV doublet respectively. Through this analysis a number of new γ rays were found to populate the 2149 keV and 2280 keV levels, allowing for the confirmation of these states within the ^{208}Po level scheme.

Due to its 3^- spin-parity assignment, and thus potential octupole collectivity, the 1995 keV state is of particular interest and is thus covered in greater detail in Sections 5.6 and 5.6. A fourth level at 1969 keV was also proposed tentatively in ref. [46], however no evidence of this state or its corresponding γ rays were observed in this analysis.

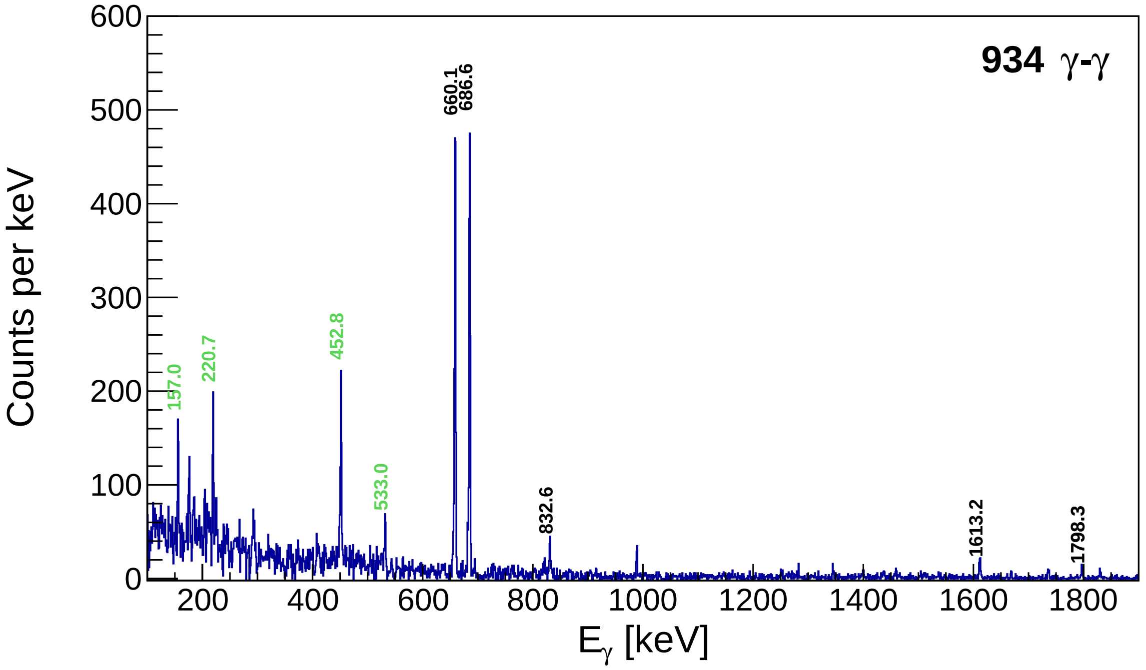

Figure 5.4: Gated $\gamma - \gamma$ spectrum containing counts in coincidence with the 934 keV M1+E2 transition from the 2280 keV $(4^+, 5^+)$ state to the 1346 keV 4^+ state. Visible are the 832.6 keV, 1613.2 keV, and 1798.3 keV transitions which populate the 2280 keV state. As well as the 660.1 keV and 686.6 keV transitions below the 1346 keV state. Peaks at 157.0 keV, 220.7 keV, 452.8 keV, and 533.0 keV are also visible due to a 936.3 keV γ ray in ^{208}Tl (a contaminant in the beam).

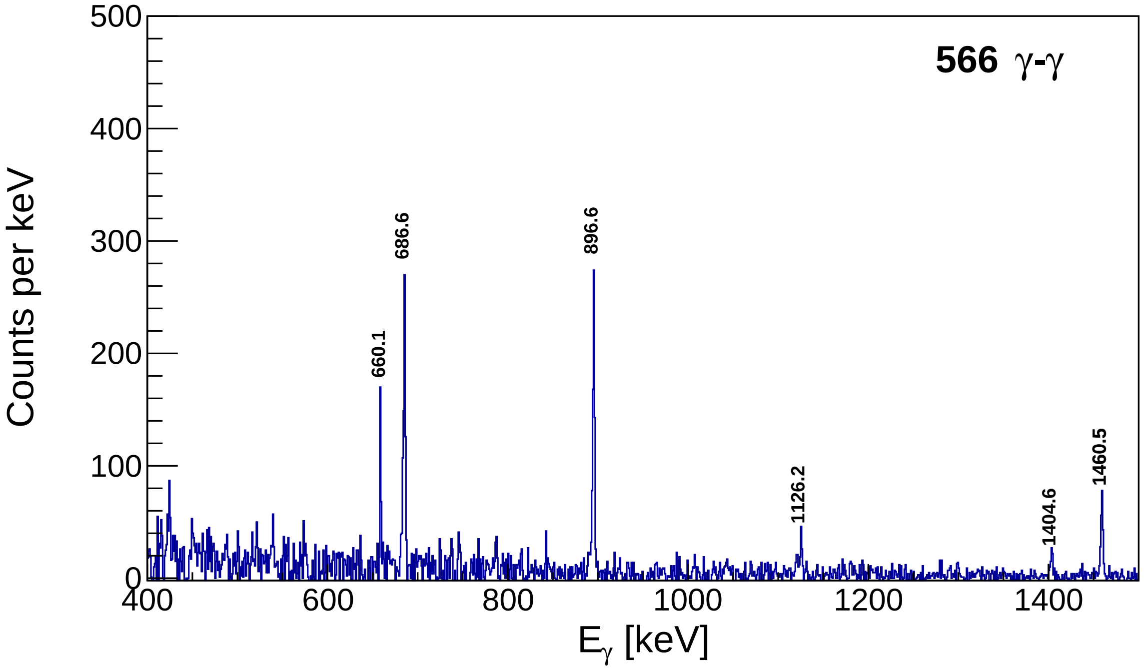

Figure 5.5: Gated $\gamma - \gamma$ spectrum containing counts in coincidence with the 566 keV M1+E2 transition from the 2149 keV $(3^+, 4^+)$ state to the 1583 keV 4^+ state. Visible are the 1126.2 keV, 1404.6 keV, and 1460.5 keV transitions which populate the 2149 keV state. As well as the 660.1 keV, 686.6 keV, and 896.6 keV transition below the 1583 keV state.

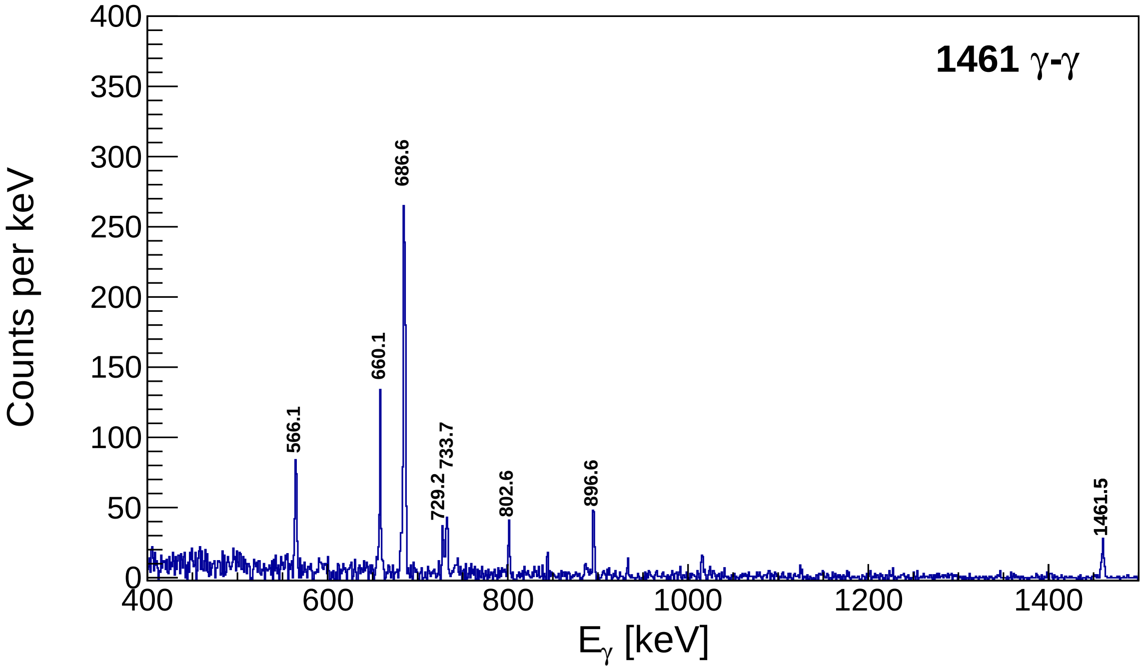

Figure 5.6: Gated $\gamma - \gamma$ spectrum containing counts in coincidence with the 1461 keV M1+E2 transition from the 3610 keV 5^- state to the 2149 keV $3^+,4^+$ state. This coincidence window encompasses the 1461.5 keV transition to the 686 keV first excited state. Visible are the 566.1 keV, 729.2 keV, 802.6 keV, and 1461.5 keV transitions from the 2149 keV state. As well as the 660.1 keV, 686.6 keV, and 896.6 keV transitions resulting predominantly from the coincidences observed in Figure 5.5.

5.5.2 The 2223 keV State

The lowest energy state newly observed in this analysis is the 2223 keV 8^+ state. This state is also notable as it requires the reassigned position of three previously-observed, high-intensity gamma rays, 333.67 keV ($I_{\gamma,rel} = 2.15$), 694.33 keV ($I_{\gamma,rel} = 3.84$), and 697.94 keV ($I_{\gamma,rel} = 1.41$). Throughout this analysis a number of transitions with previously assigned positions in the level scheme were reassigned in this work due to observed coincidence relationships. It is likely that most of these previous incorrect assignments were made due to a lack of statistics, hence most are low-intensity γ rays. The 334 keV, 694 keV, and 697 keV states are notable exceptions to this with relative intensities exceeding 1. Their incorrect placement is therefore most likely due to 334 keV and 694 keV peaks resulting from doublets, which was not known in prior analysis.

Through coincidence spectra, shown in Figures 5.7 and 5.8, the 694 keV peak was found to result from two transitions at 694.3 keV and 694.8 keV. Figure 5.7 shows the 694.8 keV peak in coincidence with the 2125.1 keV transition from the 4167 keV 7^- state. The 694.8 keV γ ray could populate the 4167 keV state, however if this were the case the 694 keV gated spectrum, shown in Figure 5.9 would yield coincidence peaks from other transitions originating from the 4167 keV state such as the strong 1752 keV γ ray, which it does not. Therefore the 694.8 keV transition must depopulate the 2042 keV 6^+ state to the 1347 keV 4^+ state.

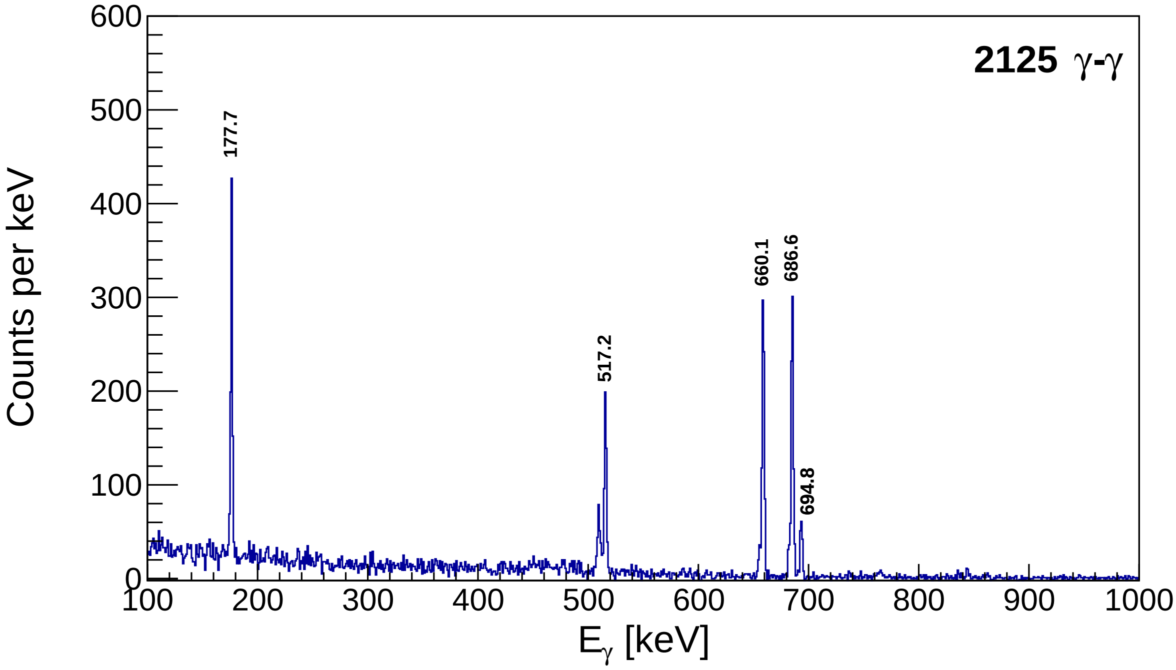

Figure 5.7: Gated $\gamma - \gamma$ spectrum containing counts in coincidence with the 2125 keV E1 transition from the 4167 keV 7^- state to the 2042 keV 6^+ state. Visible are the 517.2 keV and 694.8 keV transitions which transition from the 2042 keV state. As well as the 177.7 keV, 660.1 keV, and 686.6 keV peaks which are transitions to the ground state.

An electron conversion coefficient of α_K=0.026(4) [3, 4, 46] was previously measured for the 694 keV doublet. The multipolarity of the 694.8 keV transition from the 2042 keV 6^+ level must be E2 due to the spin-parity change. Considering these factors, the conversion coefficient of the 694.3 keV transition can be calculated as α_K=0.05(1). This indicates an M1 character, which is in agreement with the spin-parity assignment of the initial and final states.

Figure 5.8 shows a coincidence spectrum gated on the 1008 keV transition which populates the 2556 keV 7^+ state. In addition to the 262 keV, 396 keV, and 1028 keV transitions which are known to depopulate the 2556 keV state, the spectrum features a 188 keV peak which was observed in previous experiments and has now been found to also depopulate the 2556 keV

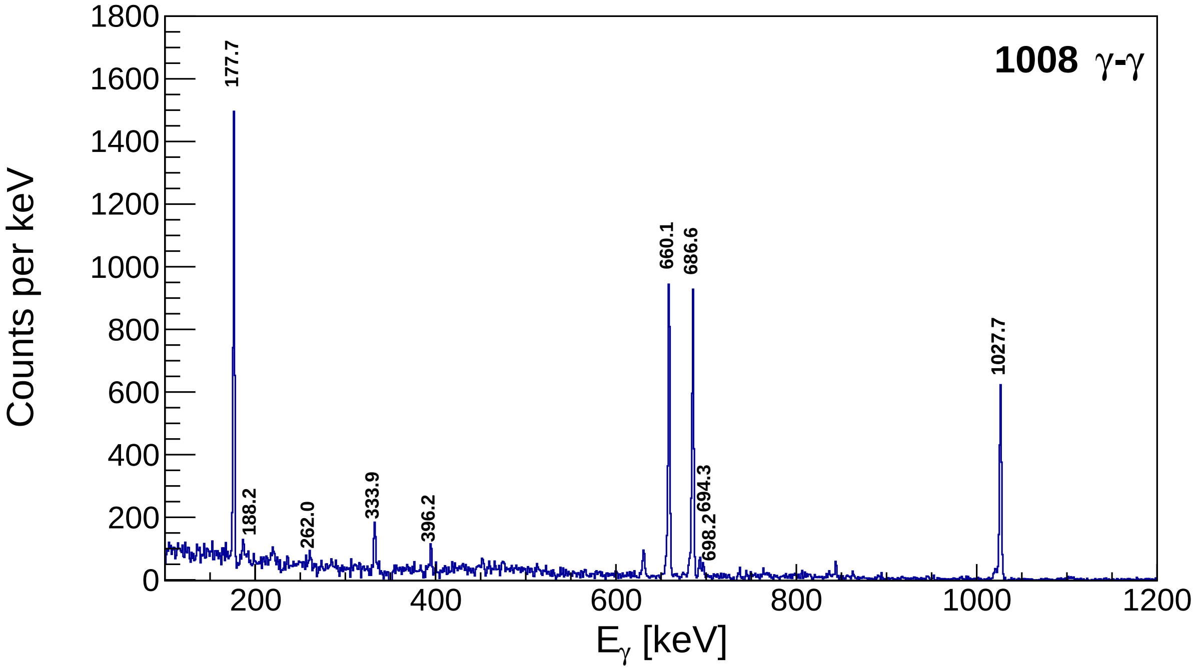

Figure 5.8: Gated $\gamma - \gamma$ spectrum containing counts in coincidence with the 1008 keV E1 transition from the 3565 keV 7^+ state to the 2556 keV 7^+ state. Visible are the 188.2 keV, 262.0 keV, 333.9 keV, 396.2 keV, and 1027.7 keV γ rays which transition from the 2556 keV state. As well as the 694.3 and 698.2 keV transitions from the 2223 keV state and the 177.6 keV, 660.1 keV and 686.6 keV transitions to the ground state.

state. Lastly, based on this spectrum the 334 keV transition has been moved from its original placement such that it also depopulates the 2556 keV state to the newly observed 2223 keV 8^+ state. Which subsequently decays via the 694 keV and 698 keV γ rays also visible in Figure 5.8. In total three transitions were found to populate the 2223 keV state directly, 333.9 keV, 801.6 keV, and 1944.1 keV.

Although the 333.9 keV and 801.6 keV transitions are both higher in intensity than the 1944 keV peak, they are each within 1 keV of another transition in the level scheme. Therefore the 1944 keV gated spectrum was used in Figure 5.10 to demonstrate the transitions from the 2223 keV state with minimal misleading peaks. In addition, the 1944 keV peak is higher in energy thus making the gated spectra less obscured by background counts. Despite lower statistics from the 1944 keV peak, both 694.3 and 698.2 keV are clearly visible in the gated spectrum, with no γ rays peaks to indicate any additional transitions from the 2223 keV state.

4 keV-difference double peaks, like the one seen at 694/698 keV in Figure 5.10, are features which occur at multiple energies in the ^{208}Po γ spectrum. The structure of ^{208}Po features a 6^+

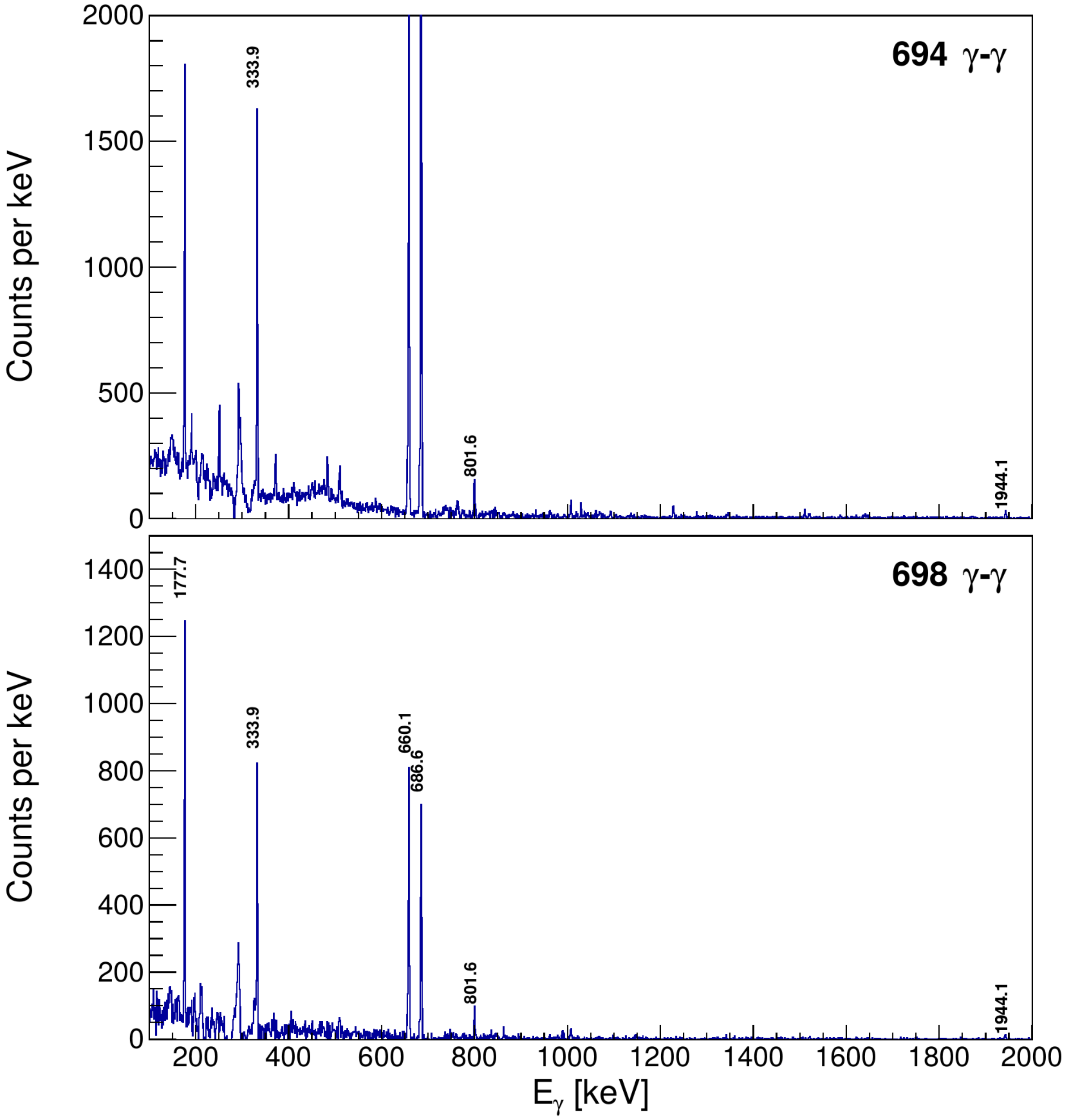

Figure 5.9: Gated $\gamma - \gamma$ spectra containing counts in coincidence with the 694 keV M1+E2 (top) and 698 keV E2 (bottom) transitions from the 2223 keV 8^+ state to the 1528 keV 8^+ and 1524 keV 6^+ states respectively. Visible in both spectra are the 333.9 keV, 801.6 keV and 1944.1 keV transitions which populate the 2223 keV state. As well as the 177.7 keV, 660.1 keV, and 686.6 keV transitions to the ground state. Due to the 694 doublet the above spectrum also features a number of transitions which populate the 2042 keV state.

and an 8^+ state within 4 keV of each other, at 1524 keV and 1528 keV respectively. Consequently, a number of states have spin parities which allow them to decay directly to both of these lower-lying states. This feature becomes more prominent for higher lying states where energy differences cause high energy decays to be substantially favoured. In γ spectra these decays result in a 4 keV-difference double peak. The 1528 keV state decays solely via a 4 keV γ ray

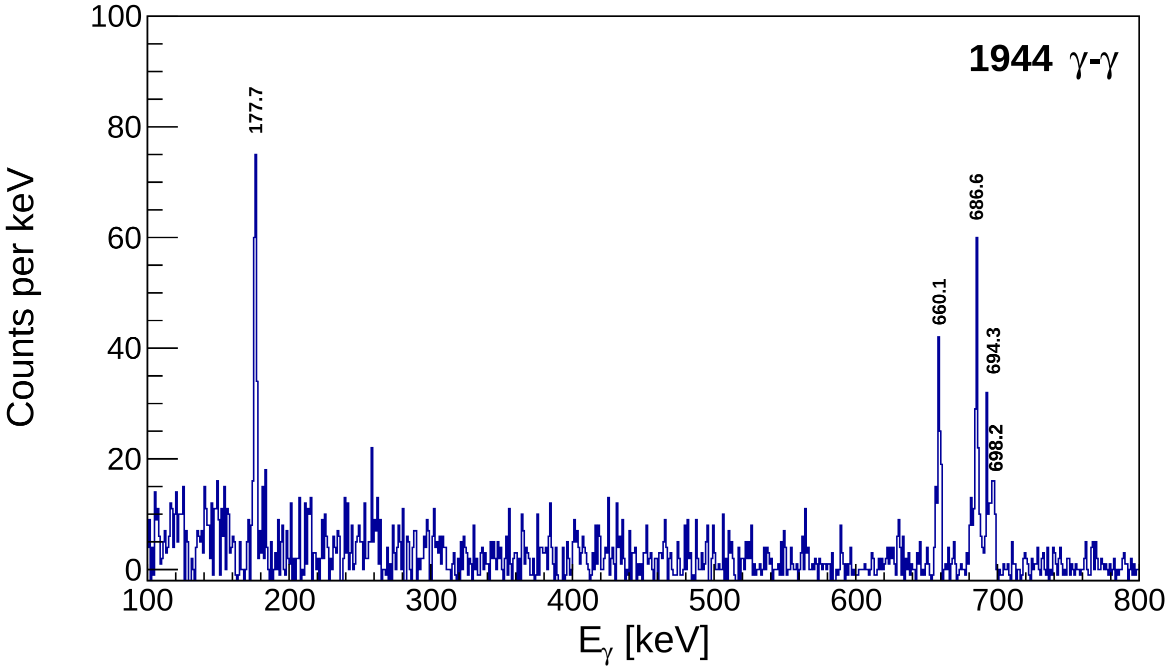

Figure 5.10: Gated $\gamma - \gamma$ spectrum containing counts in coincidence with the 1944 keV E1 transition from the 4167 keV 7^+ state to the 2223 keV 8^+ state. Visible are the 694.3 keV and 698.2 keV transitions from the 2223 keV state and the 177.6 keV, 660.1 keV and 686.6 keV transitions to the ground state.

to the 1524 keV 6^+ state. Consequently, gating on these peaks individually yields near-identical spectra similar to those shown in Figure 5.9 for 694 keV and 698 keV.

In Figure 5.10 a possible peak around 630 keV can be observed. A high intensity 632 keV is known to decay from the 2160 keV state, thus this was initially determined to result from random coincidence. Gating on the 631 keV peak however yielded some notable coincidence relationships, this gated spectrum is given in Figure 5.11.

While the transitions to the ground state and the transitions known to populate the 2160 keV state are clearly visible. The spectrum also features the 333.9 keV, 801.6 keV, and 1008.6 keV transitions which are observed in the 694 keV and 698 keV gated spectra shown in Figure 5.9. As these peaks are not the result of the ^{207}Bi contaminant also observed in the spectrum, they would suggest the existence of an unobserved 62 keV transition between the 2223 keV and 2160 keV states.

Gamma-ray detectors have low efficiency at very low energies, in addition, due to a lack of data points, energy calibrations lose accuracy below ~100 keV. Both of these factors make

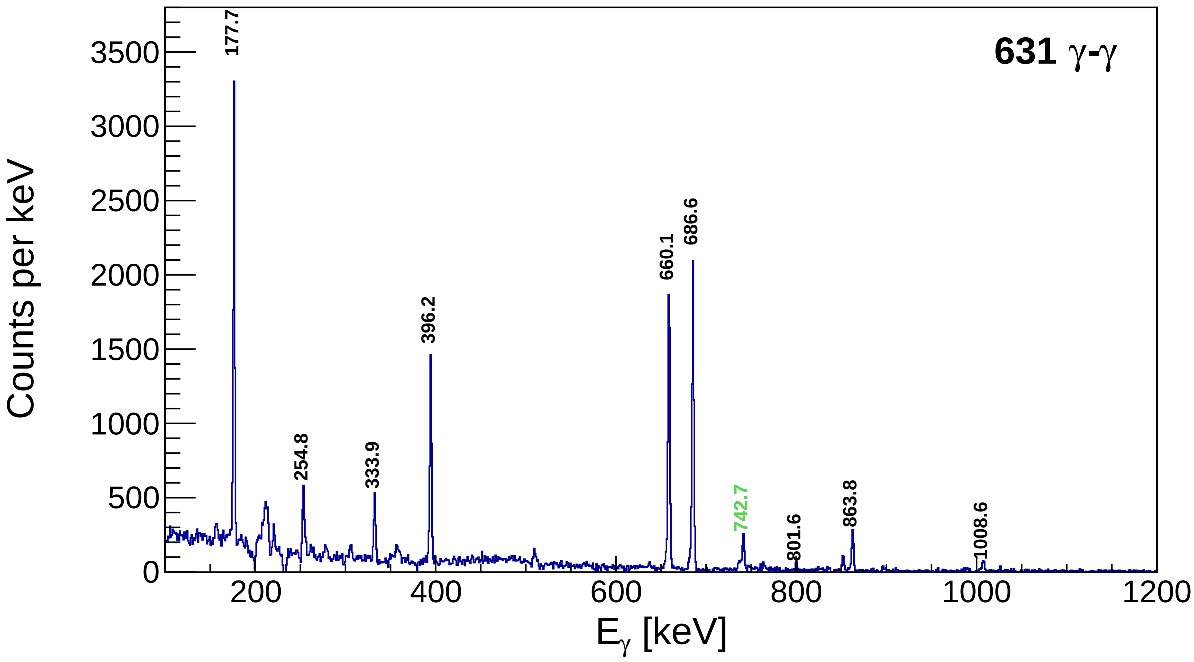

Figure 5.11: Gated $\gamma - \gamma$ spectrum containing counts in coincidence with the 631 keV M1(+E2) transition from the 2160 keV 8^+ state to the 1528 keV 8^+ state. Visible are the 254.8 keV, 396.2 keV, 863.8 keV transitions which populate the 2160 keV state. As well as the 177.7 keV, 660.1 keV, and 686.6 keV transitions to the ground state. In addition a 742.7 keV peak can be seen resulting from the 629.8 keV gamma ray in ^{207}Bi. Lastly the 333.9 keV and 801.6 keV transitions which populate the 2223 keV state are visible, which implies an unobserved, low-energy gamma ray between the two 8^+ states.

it difficult to identify and confirm low energy γ rays such as the 4 keV transition from the isomeric state and the 62 keV transition between the 2223 keV and 2160 keV states. Consequently, low-energy transitions are instead identified through coincidence relationships with higher energy gamma rays, such is the case with both low-energy transitions observed in this analysis. In addition, though it is not possible to measure their energy and intensity directly these values can also be determined through coincidence relationships, and known energy level differences. Using these techniques a relative intensity of 0.45(34) was determined for the 62.3(9) keV transition.

5.5.3 The 2438 keV State

Previously established multipolarities were used to determine the spin-parity for the newly identified 2438 keV 5^+ state. Only one transition was found to decay from the new 2438 keV state. Figure 5.12 shows the coincidence spectrum for this transition: a 1017 keV gamma ray which transitions to the 1420 keV 3^+ state.

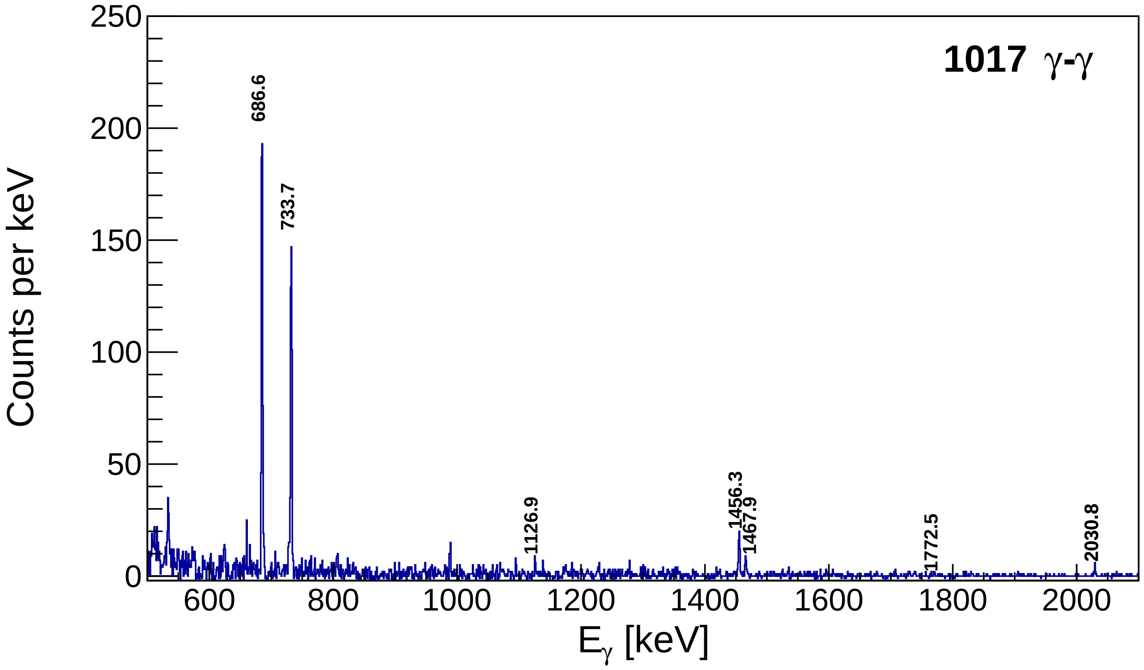

Figure 5.12: Gated $\gamma - \gamma$ spectrum containing counts in coincidence with the 1017 keV transition from the 2438 keV $4, 5, 6^-$ state to the 1420 keV 3^+ state. Visible are the 1126.9 keV, 1456.3 keV, 1467.9 keV, 1772.5 keV, 2030.8 keV transitions which populate the 2438 keV state. As well as the 733.7 and 686.6 keV transitions to the ground state.

The 686.6 keV and 733.7 keV transitions are clearly visible, with no statistically significant peak at 660 keV which is as expected for a transition onto the 1420 keV level. In addition to these, a number of smaller, higher energy peaks are also visible at 1126 keV, 1456 keV, 1467 keV, 1772 keV, and 2030 keV which relate to transitions from higher-lying states. The most significant of these is the 1126 keV peak, which is the result of a decay from the 3565 keV 6^- state. The conversion coefficient of the 1017 keV transition was measured in a prior experiment to be $\alpha_K = 0.010(2)$ [4], limiting the multipolarity to M1+E2. Consequently the 2438 keV state must have positive parity. Prior analysis also measured the conversion coefficient of the 1126 keV γ ray to be $\alpha_K \leq 0.006$ [68], which limits the multipolarity to E1 or E2. The previous assignment of the 1126 keV transition in the level scheme necessitated an E1 assignment as a change in parity was required. This requirement is also applicable in this instance, and thus the 1126 keV transition is E1 as there is no evidence of a second 1126 keV γ ray from the 3683 keV $5^-, 6^-$ state. With these restrictions, the final spin-parity of the 2438 keV state is limited to 5^+, which implies a strong E2 component for the 1017 keV γ ray.

5.5.4 The 3276 keV State

The 3276 keV state features two transitions with conflicting multipolarity; the 1693 keV and 1930 keV γ rays, which both transition to 4^+ states (1583 keV and 1346 keV respectively). Gating on each of these transitions yields the following coincidence spectra, shown in Figure 5.13.

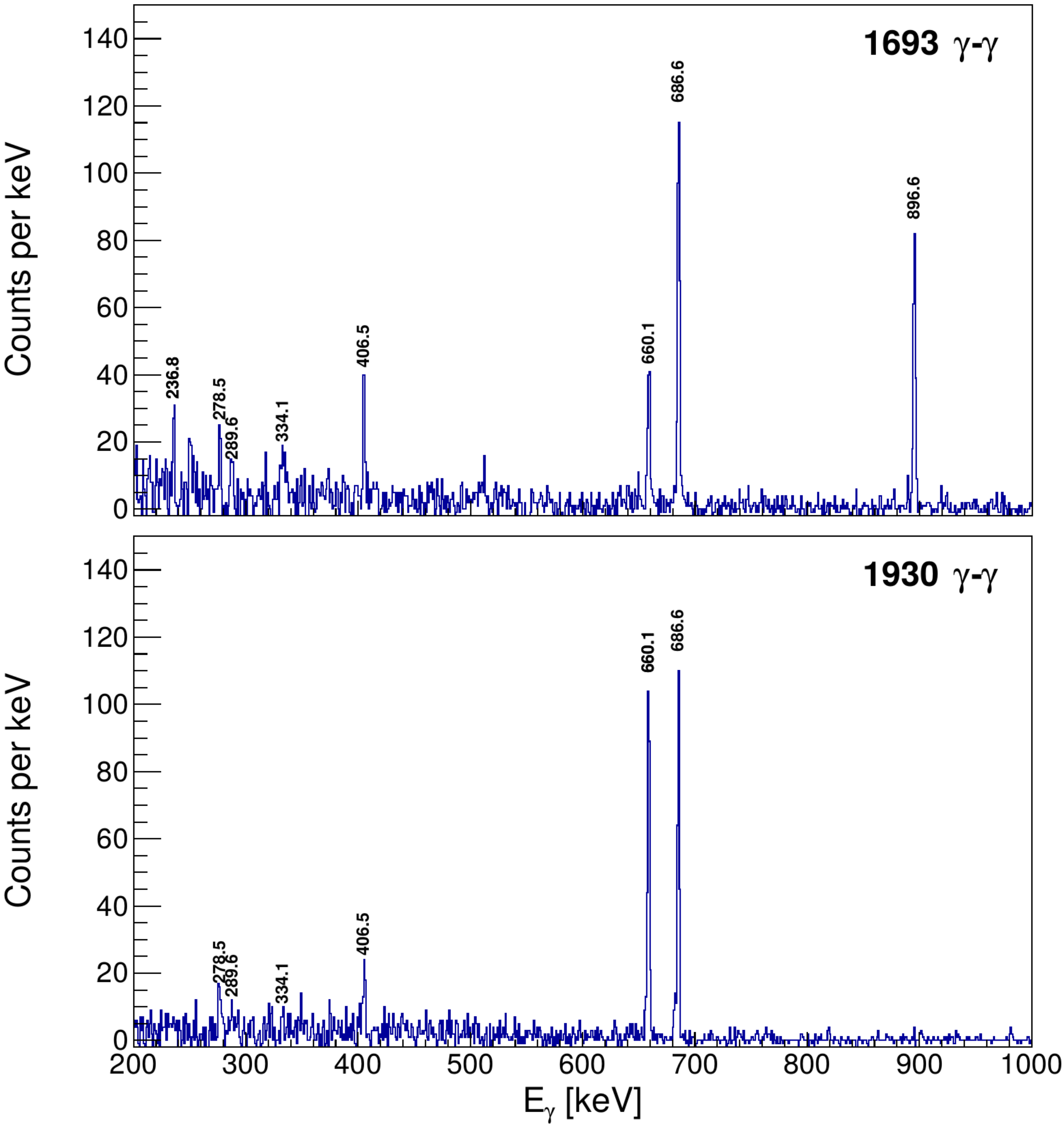

Figure 5.13: Gated $\gamma - \gamma$ spectra containing counts in coincidence with the 1693 keV (top) and 1930 keV (bottom) transitions from the 3276 keV $4^-, 5, 6, 7^-$ state to the 1583 keV 4^+ and 1346 keV 4^+ states respectively. Visible in both spectra are the 278.5 keV, 289.6 keV, 334.1 keV and 406.5 keV transitions which populate the 3276 keV state. As well as the 236.8 and 896.6 keV transitions visible in the top spectrum and 660.1 keV, and 686.6 keV transitions in both spectra which are decays to the ground state.

Each features the expected peaks from transitions to the ground state, in addition to the four peaks (278.5 keV, 289.6 keV, 334.1 keV, and 406.5 keV) from transitions onto the 3276 keV state. Despite the 290 keV and 334 keV peaks being somewhat obscured by the background in the 1930 keV gated spectrum, the 279 keV and 406 keV peaks are clearly visible making it likely that this is due to a lack of statistics and not a misplacement of the 1930 keV transition. Both the 1693 keV and 1930 keV transitions were observed in previous analysis, but neither were placed into the level scheme, likely due to a lack of statistics at higher energies. Despite this, measurements were made of the conversion coefficients which give multipolarities of E1 and M1+E2 for the 1693 keV and 1930 keV transitions respectively. With both transitions decaying to 4^+ states, each require opposite $\Delta\pi$ values, which is unresolvable. The current analysis has no explanation for this disagreement, but there are a number of possible solutions which would require greater statistics to confirm.

The first solution would be a misplacement of one of the transitions as this would mean the parity is solely dependent on the remaining γ ray. Given the agreement of the coincidence spectra in Figure 5.13 this is unlikely, but more statistics may reveal unobserved coincidence relationships. The second solution would be a possible doublet resulting in inaccurate conversion coefficient measurements. This also seems unlikely as the measured intensities are in agreement with the intensities of the unplaced transitions, and there are also no unexplainable peaks in either spectrum to suggest a second transition.

Finally, the conversion coefficient measurements could be inaccurate due to other factors. For the 1930 keV γ ray the conversion coefficient is quoted as $\alpha(K) \approx 0.0026$, this is very approximate and with no error bar it is difficult to rule out other multipolarities with complete certainty. This is the most likely cause of the parity discrepancy, but as with the potential misplacement further analysis with improved statistics will be needed to determine this. For this analysis, both multipolarity assignments have been disregarded, and no restriction on the spin-parity of the 3276 keV state has been made as a result of either transition.

5.6 1995 keV State Spin-Parity Determination

A previous decay study of ^{208}Po identified a possible low-lying state at 1995 keV with spin-parity $2^-, 3^-$, based on a 1308 keV E1(+M2) transition to the 686 keV 2^+ state, and a second transition to the 1420 keV 3^+ state. Further analysis was conducted to identify new transitions above and below the 1995 keV state in order to obtain a single value for the spin-parity. Gating on the 1308 keV peak yielded the coincidence spectrum in Figure 5.14.

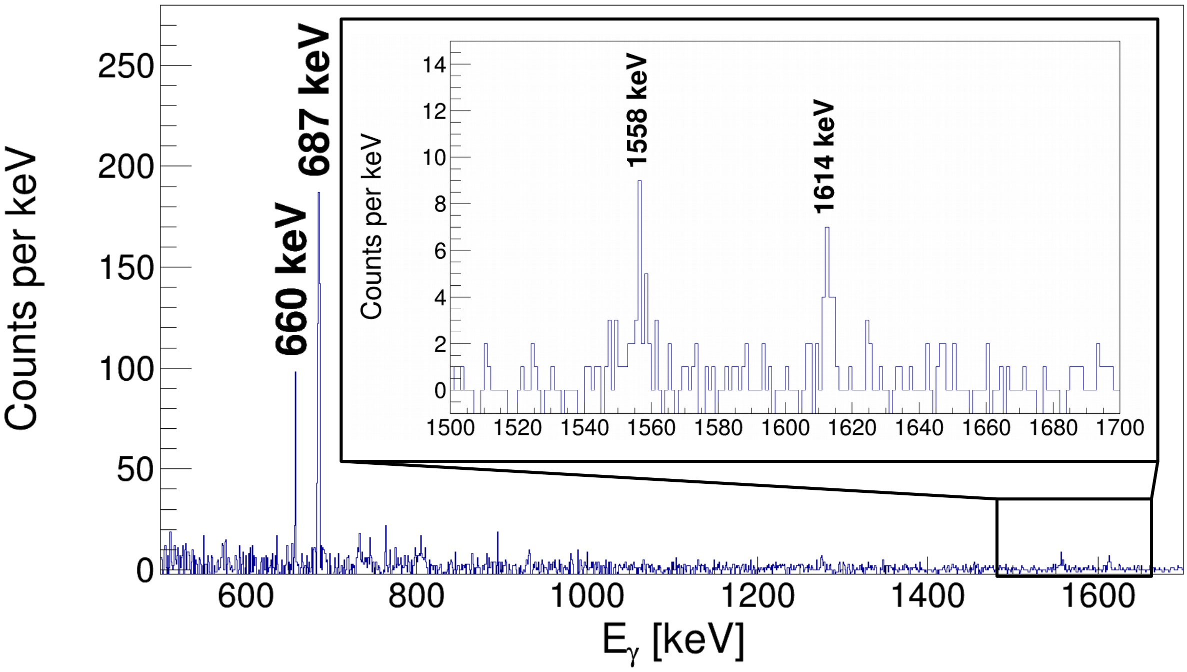

Figure 5.14: Gated $\gamma - \gamma$ spectrum containing counts in coincidence with the 1308 keV E1(+M2) transition from the 1995 keV 3^- state to the 686 keV 2^+ state. Visible are the 1558.2 keV and 1614.4 keV transitions which populate the 1995 keV state.

From this spectrum, two high energy peaks at 1558 keV and 1614 keV were identified. Gating on these peaks produced the spectra shown in Figure 5.15.

Both gated spectra reproduce the 1308 keV peak, as well as the expected 575 keV peak known to also transition from the 1995 keV state. The experiment which initially identified the 1995 keV state also proposed a possible third decay from it to the 1263 keV 2^+ state. Such a decay would have an energy of 732 keV and is thus obscured by the 734 keV decay from the 1420 keV state. Therefore, no conclusive evidence for the 732 keV transition could be found in

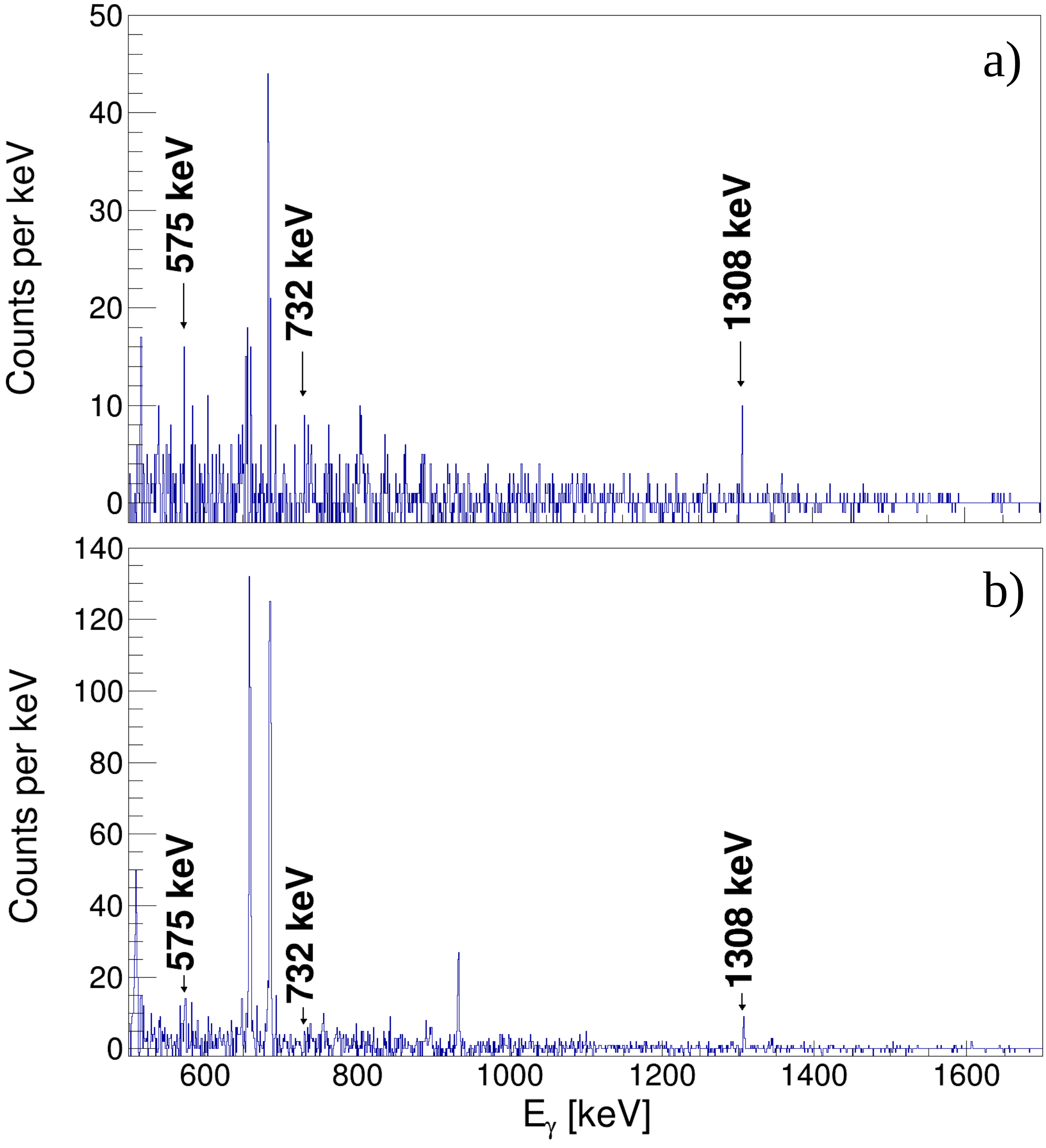

Figure 5.15: a) Gated $\gamma - \gamma$ spectrum containing counts in coincidence with the 1558 keV transition from the 3554 keV 5^- state to the 1995 keV 3^- state, visible in Figure 5.14. Visible are the 575.3 and 1308.2 keV transitions from the 1995 keV state. b) Gated $\gamma - \gamma$ spectrum containing counts in coincidence with the 1614 keV transition from the 3610 keV 5^- state to the 1995 keV 3^- state, visible in Figure 5.14. Visible are the 575.3 keV and 1308.2 keV transitions from the 1995 keV state. Due to a second transition in ^{208}Po at 1613 keV to the 2280 keV state a peak at 934.1 keV is also visible. The position of the postulated 732 keV is also given for both spectra.

this coincidence spectra. It is possible that with greater statistics, comparisons of the 575 keV and 732 keV peak intensities could be conducted to determine the existence of a third transition, however the statistics in this analysis are insufficient for this purpose.

Placing the 1558 keV and 1614 keV transitions into the level scheme above the 1995 keV

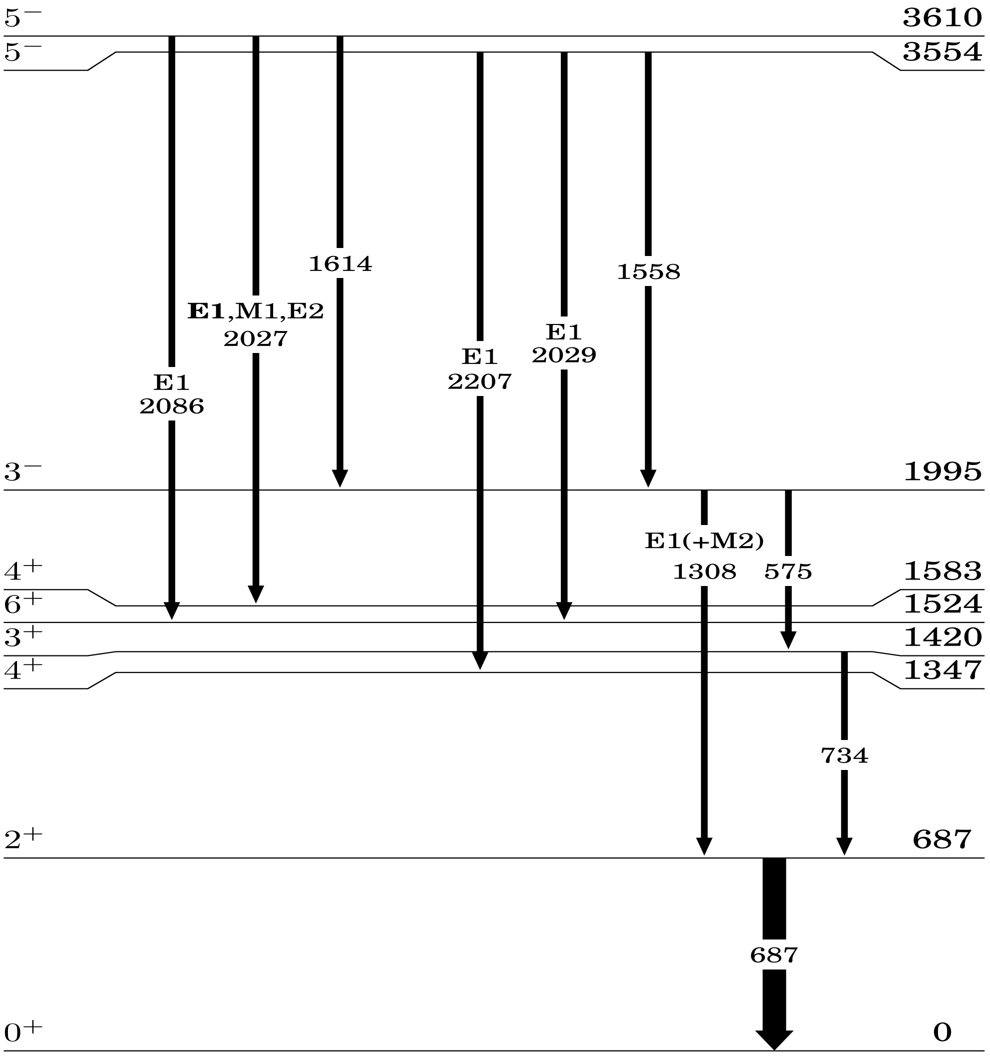

Figure 5.16: Level scheme of levels and transitions relevant to the 1995 keV 3^- state.

state results in them decaying from the 3554 keV and 3610 keV states respectively (shown in Figure 5.16. Both of these levels have spin-parities of 5^-, therefore, for the 1995 keV state to have a J^π value of 2^-, both decays would have to have multipolarity of at least M3. Both the 3554 keV and 3610 keV states have more favourable decay paths than an M3 transition. Thus, although the half-lives of higher multipolaritiy decays are lower for higher energies, given the measurement time used in the experiment it is unlikely the 1558 keV and 1614 keV transitions would be observed if they were M3 transitions. This excludes the possibility of a 2^- assignment for the 1995 keV state. Thus, through a combination of multipolarities determined from prior studies [4, 5, 46, 68], and the two transitions identified in this analysis to populate the 1995 keV state, the spin-parity of the 1995 keV state was determined to be 3^-. All transitions relevant to the 3^- spin-parity assignment of the 1995 keV state, are shown in Figure 5.16. In addition, the transitions necessary to assign 5^- spin-parity to the 3554 and 3610 keV levels are also shown. The transitions to the ground state have also been included in the figure for completeness. Figure 5.16 also demonstrates the coincidence relationship of the 575 keV and 734 keV transitions which obscures the potential 728 keV transition from the 1995 keV state.

5.7 Unplaced Transitions From Prior Analysis

The high density of states in ^{208}Po able to be populated by both β^+ and EC decay, produces a high number of internal decay paths. The resulting γ rays cover a wide range of energies and intensities, thus many feature low intensity and/or peak energies which overlap with other γ peaks in the decay spectrum. Both of these factors make it difficult to determine the position of a given γ ray in the level scheme, even when the γ ray is known to result from the decay of ^{208}At. Prior to this analysis 73 transitions had been observed and attributed to decays in ^{208}Po, but remained unplaced in the previous level scheme[3]. The higher detection efficiency provided by the IDS set-up, offered the opportunity to place a number of these γ rays. In total, 33 of the previously-observed transitions were added into the ^{208}Po level scheme, in addition to the new levels and transitions identified. The top graph in Figure 5.17 shows how these unplaced γ5 rays are distributed with respect to energy and relative intensity.

With the exception of a few transitions, the γ rays placed in this analysis all lie in the high-energy and/or high-intensity region in the top graph of Figure 5.17. This clearly demonstrates how energy and intensity influence the determination of γ-ray position within the level scheme. From this analysis, with respect to intensity, all unplaced transitions with previously-measured relative intensity >0.35 have been placed into the level scheme. Due to a number of high-energy, low-intensity unplaced transitions, a similar statement cannot be made regarding energy. However, the proportion of placed transitions increases from 45% to 54% for energies

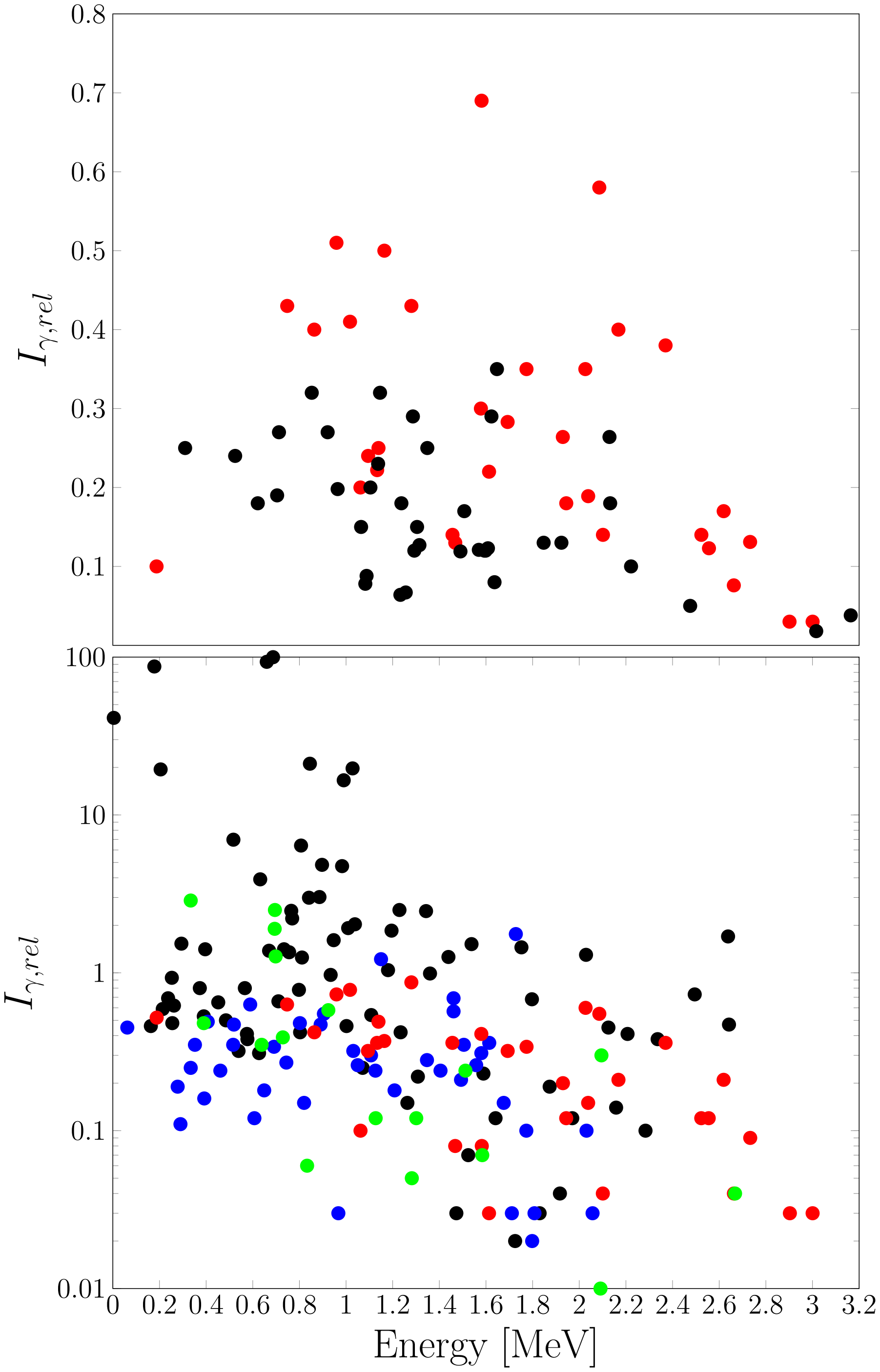

Figure 5.17: Relative intensity and energy of γ rays in ^{208}Po. (Above) Transitions observed in prior decay studies but were not placed in the previous level scheme. With transitions placed in this analysis in red (●), and transitions which remain unplaced in black (●). (Below) All transitions observed in this analysis. With transitions unchanged from prior analysis in black(●), unplaced transitions assigned in the level scheme in red (●), transitions reassigned a position in the level scheme in green (●), and new transitions in blue (●).

>1.5 MeV, and up to 65% for energies >2 MeV.

When this distribution is repeated for all observed γ rays (displayed in the bottom graph of Figure 5.17) new and (re)placed transitions make up the majority of the low-intensity and high-energy data points. This reinforces the role of higher detection efficiency in resolving these γ rays, as it allowed for clearer gated spectra, which in turn facilitated the expansion of the level scheme to include these less discernable γ rays. Another interesting feature of this graph is the distribution of new and previously-placed transitions, occupying predominantly low and high intensities respectively. Similar to the distribution in the top graph of Figure 5.17, this also reflects the role of intensity in γ-ray placement, and highlights the extent to which the detection efficiency has improved between experiments. Similarly, low-energy and/or low-intensity γ rays are more likely to be assigned incorrectly due to obscured coincidence relationships. Furthermore, γ-ray doublets can also be missed during analysis, as gated spectra may not contain sufficient statistics to observe the coincidence peaks necessary to resolve the doublet. Consequently, the reassigned transitions shown in Figure 5.17 predominantly feature low energy and/or low intensity, or are the result of newly observed doublets.

5.8 Measurement of Isomer Half-life

A prominent feature in the structure of ^{208}Po is the isomeric 8^+ state at 1528 keV. The isomer is caused by the lack of favourable decay paths, as possible transitions to lower-lying states have high multipolarity (at least E4). The only exception to this is the transition to the 1524 keV 6^+ state, with E2 multipolarity. As a result, the 1528 keV state decays solely via this 4 keV E2 transition which, given its low energy and thus significant half-life, results in an isomeric state. The half-life of this isomeric state has been measured in prior ^{208}Po studies. Based on these measurements the half-life is currently quoted at 350(20) ns[3]. The 4 keV transition cannot be gated on directly due to low detection efficiency at such low energies. Therefore, other methods must be used to determine the half-life and confirm both the isomeric state and transitions to it.

In this analysis, coincidence times between γ rays were used to confirm the existence of the isomeric state. Coincidence times for γ rays with the 177 keV transition from the 1524 keV state showed a large proportion of high coincidence times which could not be explained by random coincidences. Figure 5.18 shows a comparison of coincidence times between a prompt gamma decay to the 1524 keV state, and a delayed γ decay to the isomeric state.

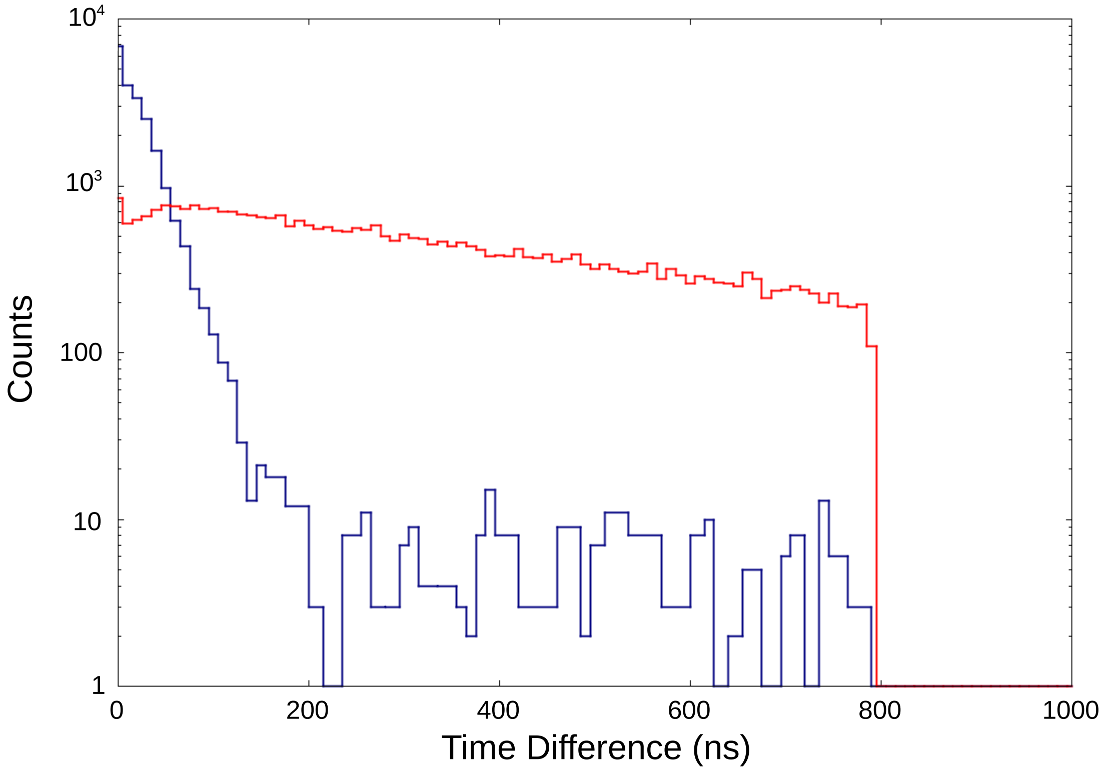

Figure 5.18: gamma-gamma time difference spectrum between coincidences with the 177 keV transition. The blue spectrum shows the time difference for the 517 keV transition to the 1524 keV state (prompt). The red spectrum shows the time difference for the 631 keV transition to the 1528 keV isomeric state (isomer delayed). The graph stops abruptly at 80 ns due to the coincidence window used for this part of the analysis.

Using this relationship, spectra were generated using coincidence time gates on a $\delta t - \gamma - \gamma$ matrix. Figure 5.19 shows the energy spectrum of delayed γ rays with the counts from prompt γ rays subtracted.

As mentioned previously, the similar spin-parities between the 1524 keV and 1528 keV states result in multiple double peaks with 4 keV energy difference due to levels which decay to both lower-lying states. These peaks can be clearly seen in Figure 5.19 as the peaks coincident with the transition to the 1524 keV state are negative, whereas the peaks coincident with the transition to the isomer are positive, the clearest example being the 841/845 keV double

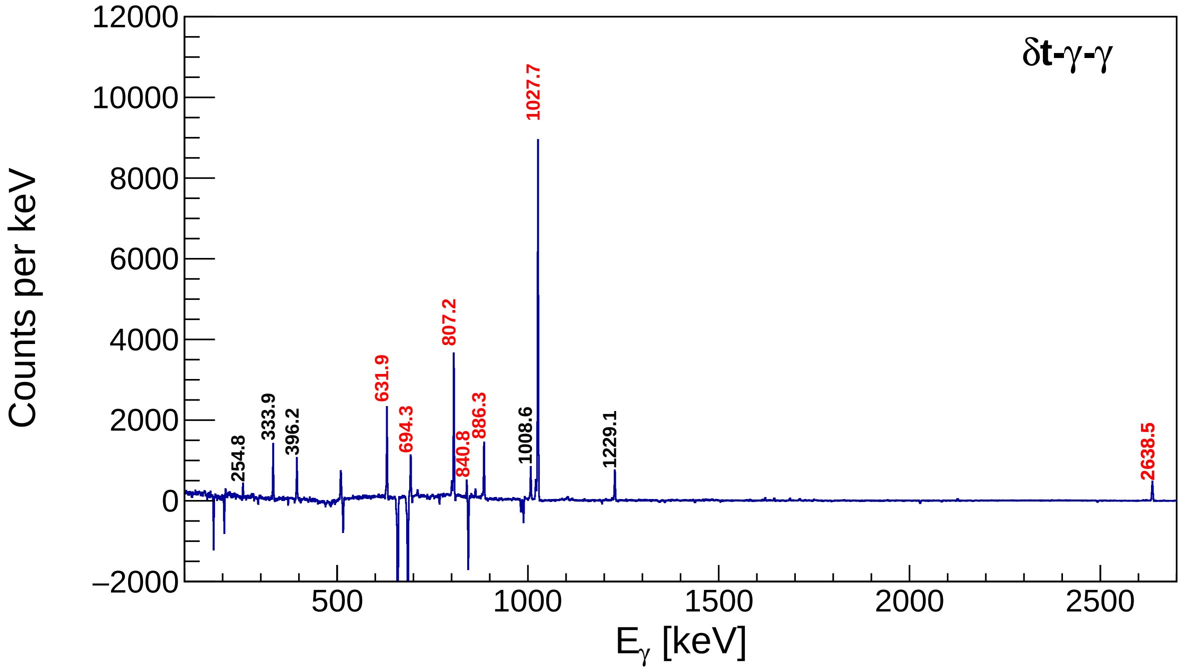

Figure 5.19: Gamma spectrum gated on the 177.7 keV E2 transition from the 1524 keV 6^+ state. A second gate was placed on coincidence time for delayed γ decays; a coincidence time of >100 ns was used, with prompt γs (coincidence time <20 ns) subtracted. Visible are the majority of transitions to the 1528 keV isomeric state (shown in red), as well as a number of peaks which result from indirect delayed coincidence (transitions to states which subsequently decay to the isomeric state) (shown in black).

peak. These double peaks can be particularly challenging for analysis as gating cleanly on the individual peaks can be very difficult. This is compounded when double peaks have similar or drastically different intensities as peaks can be obscured. Therefore, in order to produce a clean coincidence-time spectrum to measure the half-life of the isomer, transitions had to be selected where no transition to the 1524 keV state is visible. Two transitions where this is the case are the 631.9 keV and 1027.7 keV transitions visible in Figure 5.19.

Despite its significantly higher intensity, the 1027.7 keV transition's proximity to other high intensity peaks in the spectrum present challenges to achieving a clean time difference spectrum. Thus the 631.9 keV peak was selected for the measurement of the isomer half-life. Plotting the counts against the coincidence time between the 631.9 keV and 177.7 keV transitions yields the data shown in Figure 5.20. Fitting these data yielded a value for the isomer half-life of 377(9) ns [70]. This is in agreement with both the accepted value and the previous measurement of the half-life obtained from the decay of ^{208}At (380(90) ns [73]). However, the value presented in this analysis has a significantly lower error bar than both previous measurements.

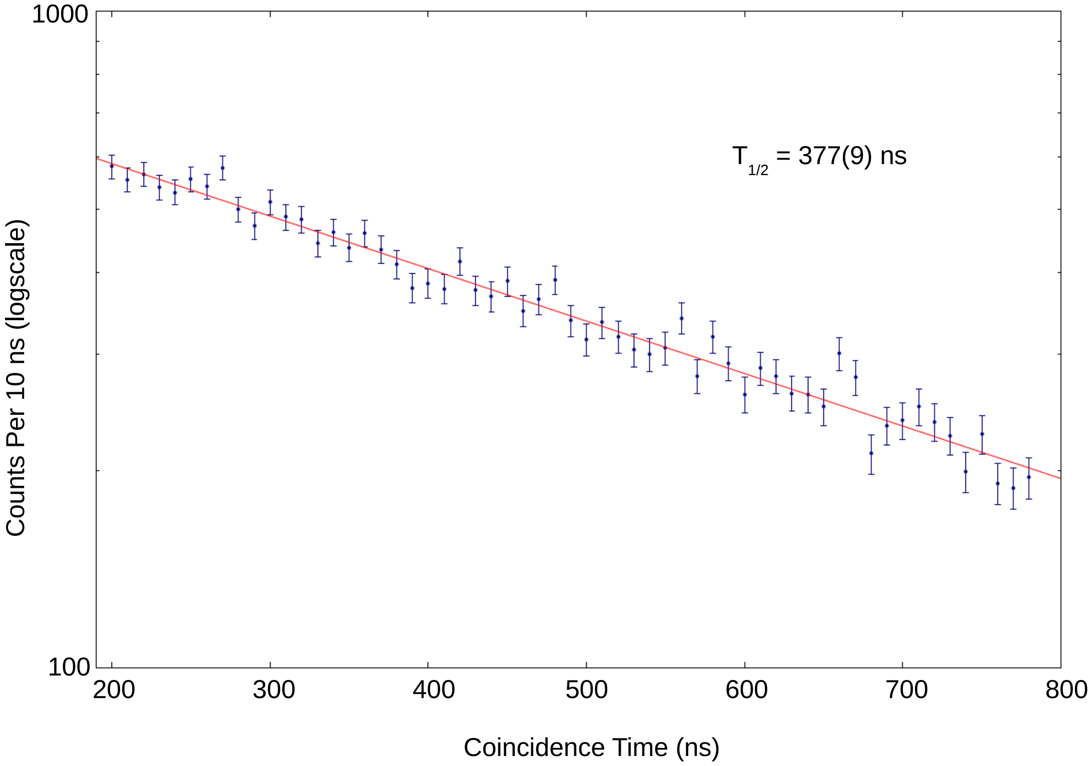

Figure 5.20: Coincidence time spectrum for the 1528 keV isomeric state. The time difference between the 631.9 keV and 177.7 keV transitions is shown.

Chapter 6

Discussion

6.1 Shell Model Calculations

For nuclei with few valence nucleons, the complexity of the system is such that simulations of the structure can be produced. Polonium-208 is in close proximity to the doubly-magic ^{208}Pb nucleus, making shell model calculations both possible and a useful point of comparison for a large number of states. These shell model calculations can offer insight into underlying nuclear structure through comparison with experimental observations. The following sections detail the parameters of the two sets of calculations performed for this analysis, as well as the insights and conclusions drawn from comparisons with experimental results.

6.1.1 Shell Model Calculations (82<Z<114, 100<N<126)

The first set of shell model calculations were carried out using the NuShellX code [74]. The "pbpop" interaction was used (detailed in ref. [75]), which considers only the nucleons in the proton orbitals $h_{9/2}$, $f_{7/2}$, and $i_{13/2}$ above Z=82, as well as the neutron orbitals $f_{5/2}$, $p_{3/2}$, $p_{1/2}$, and $i_{13/2}$ below N=126.

Figure 6.1 shows the energy comparison between the experimentally observed states and the predicted states from the "pbpop" shell model calculations. There is reasonable agreement in energies between the current decay scheme and the corresponding predicted states for the lowest two levels as well as the 1583 keV state. The remaining states however feature an energy disparity of at least 200 keV. Despite this, these calculations successfully reproduce the $\pi h_{9/2}^2$

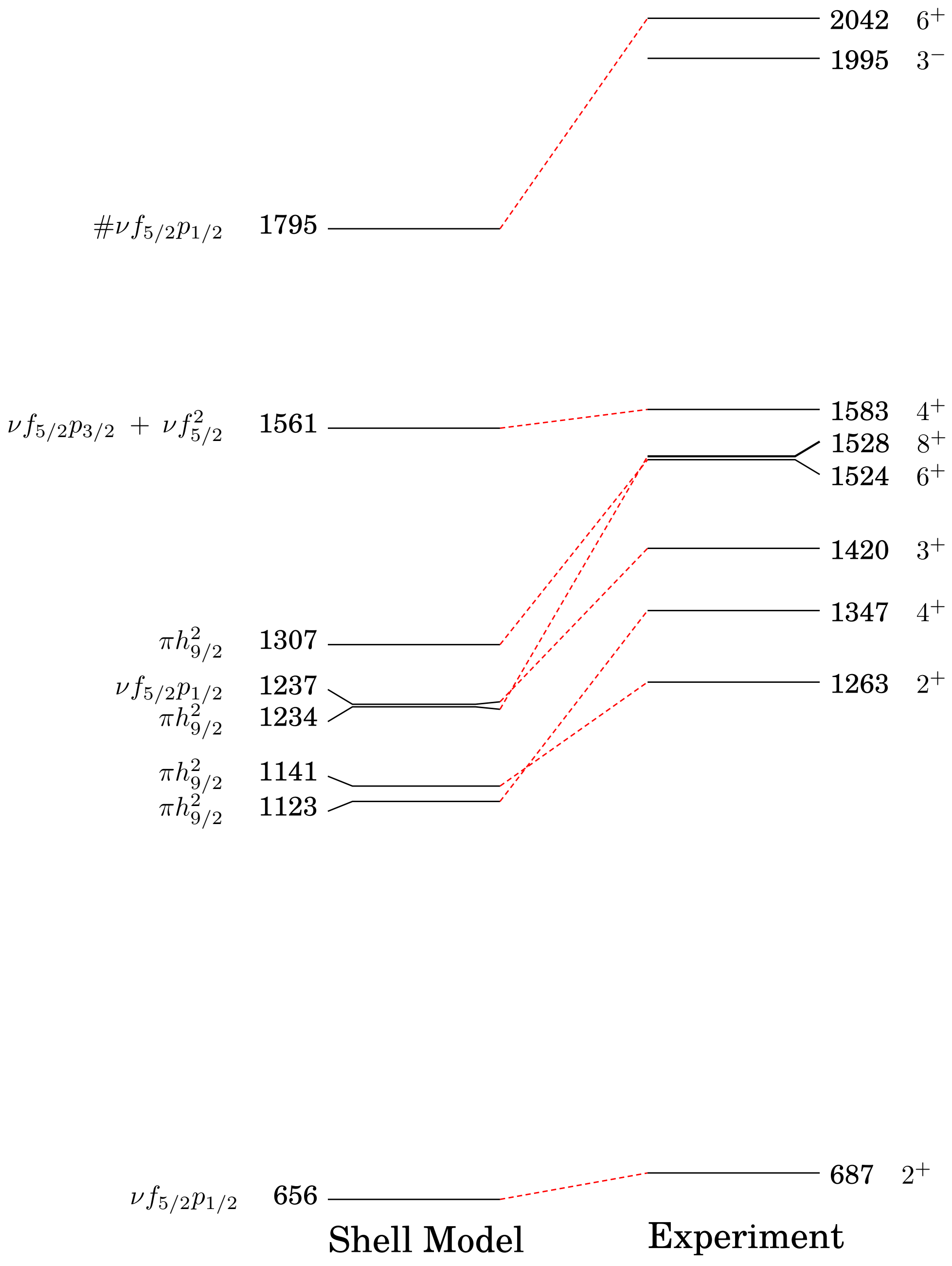

Figure 6.1: Comparison of shell model calculations using the "pbpop" interaction and experimental excited states in ^{208}Po. On the left dominant configurations are given, taken from shell model calculations, with # denoting $\pi h_{9/2}^2$. On the right, spin-parity assignments are given.

seniority scheme, although a large energy disparity is present for each $\pi h_{9/2}^2$ state, and the order of the 2^+ and 4^+ states is reversed. All the predicted levels lie at energies below the experimental state, which would suggest a misestimation in the calculations. This is potentially the result of the narrow model space used.

Another notable discrepancy is the absence of the low-energy 3^- state which contradicts the experimentally observed 1995 keV level. The lowest 3^- state predicted in these shell model calculations is found at 3181 keV. This would suggest a collective nature for the 1995 keV state, as this would not be reproduced in these calculations. In order to gain a better understanding of the shell structure and the nature of the low-energy, 3^- state, the model space should be expanded to include additional orbitals.

6.1.2 Shell Model Calculations (82<Z,N<126)

These shell model calculations were also carried out using the NuShellX code [74]. The Hamiltonian used was the modified Kuo-Herling [76] for the proton-proton and neutron-neutron interactions, with the M3Y potential [77, 78] implemented for the proton-neutron interaction. Single-particle energies were obtained from Figure 1. in [76]. Only the proton and neutron orbitals $h_{9/2}$, $f_{7/2}$, $f_{5/2}$, $p_{3/2}$, $p_{1/2}$, and $i_{13/2}$, were used in the model space which covers $Z > 82$ and $N < 126$. Therefore for ^{208}Po this does not allow for excitations across shell closures but does give two proton-particle and two neutron-holes states. Radial wave functions from the Skx Skyrme Hartree-Fock calculation [79] were used for the E2 matrix elements. The effective charges were e_p = 1.5e and e_n = 0.8e for E2 transitions, taken from [80]. Free nucleon g factors were used for the M1 and M2 matrix elements ($g_{sp} = 5.586$ and $g_{sn} = -3.826$, with $g_{lp} = 1.0$, and $g_{ln} = 0.0$). Matrix elements for E1 are zero in this model space.

A comparison of experimentally observed excited states and their equivalent shell model states, up to $\sim$2.7 MeV, is given in Figure 6.2.

As a consequence of expanding the model space, the number of predicted states substantially increased. In several instances, multiple shell model states could be attributed to the same experimentally observed state due to non-fixed spin-parity assignments. For these cases, in addition to energy similarity, corresponding states were assigned based on comparisons between measured and theoretical branching ratios (shown in Table 6.1 and Appendix B.1), these are indicated by a star in Figure 6.2. Using these techniques a single spin-parity assignment can be made for all states up to 2.6 MeV. Due to the approximate nature of theoretical branching

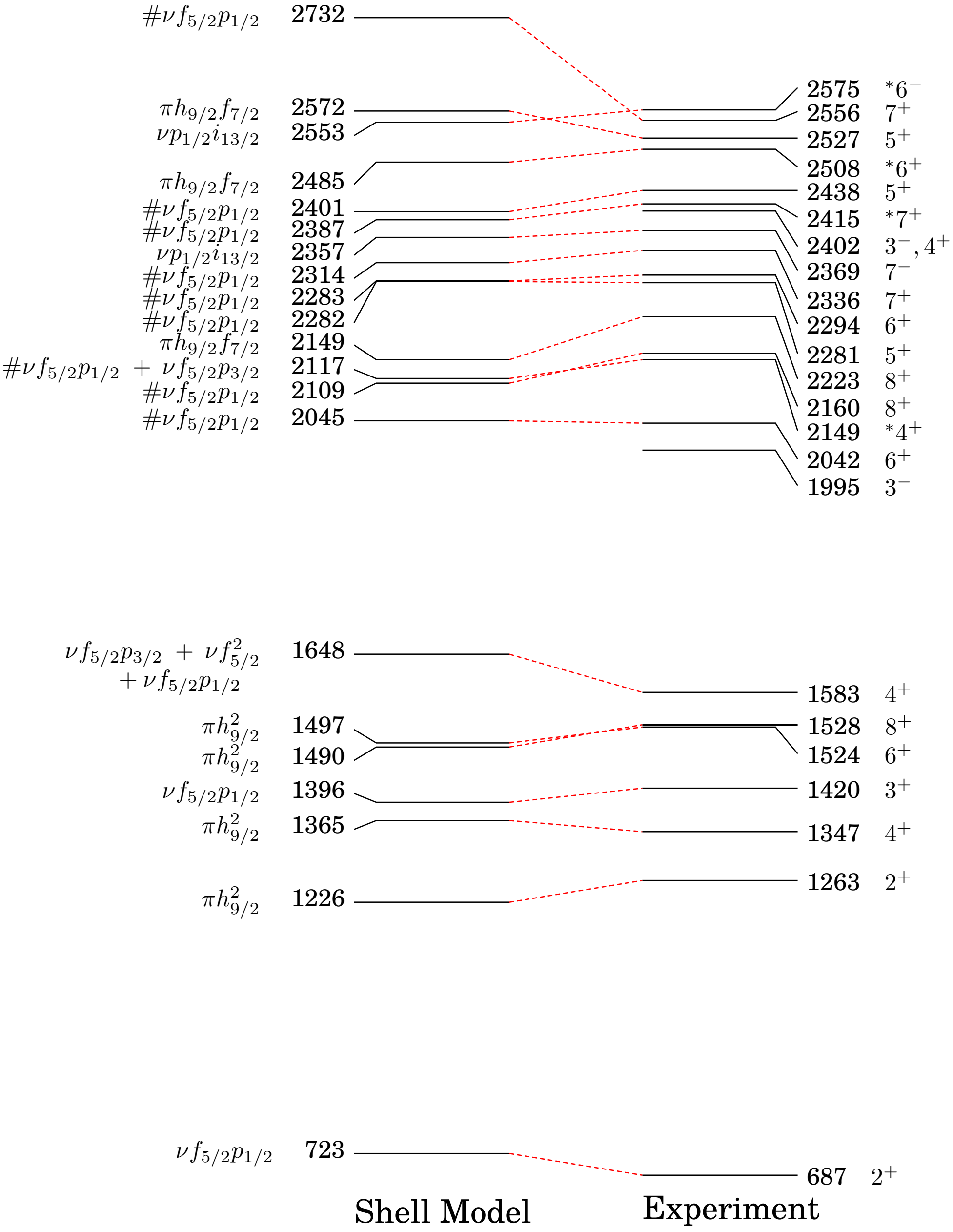

Figure 6.2: Comparison of shell model calculations using the modified Kuo-Herling Hamiltonian with an expanded model space and experimental excited states in ^{208}Po. On the left dominant configurations are given, taken from shell model calculations, with # denoting $\pi h^2_{9/2}$. On the right, spin-parity assignments are given, with * denoting states where assignments have been made using branching ratio comparisons.

ratios they are a weak justification for spin-parity assignments, therefore these values are not included in the final level scheme.

Table 6.1: Comparison between experimental and shell model γ-ray branching ratios. Only transitions with experimental or theoretical $\mathrm{BR}_\gamma > 1\%$. are shown. In some cases no firm experimental spin-parity assignments could be achieved, as shown in Table I. When the proposed spin-parity is based on comparison with theory, as shown in the present table, these are preceded by the star symbol.

Experiment			Shell Model		
E_i (keV) / J_i^π	E_f (keV)/ J_f^π	BR_γ (%)	E_i (keV)	E_f (keV)	BR_γ (%)
687 / 2^+	0	100	723	0	100
1263 / 2^+	687 / 2^+	70	1226	723	30
	0 / 0^+	30		0	70
1347 / 4^+	687 / 2^+	100	1365	723	100
1420 / 3^+	1263 / 2^+	-	1396	1226	1
	687 / 2^+	100		723	99
1524 / 6^+	1347 / 4^+	100	1497	1365	100
1528 / 8^+	1524 / 6^+	100	1490	-	-$^{a)}$
1583 / 4^+	1420 / 3^+	3	1648	1396	13
	1347 / 4^+	7		1365	4
	687 / 2^+	90		723	83
2042 / 6^+	1524 / 6^+	72	2045	1497	61
	1347 / 4^+	28		1365	38
2149 / *4^+	1583 / 4^+	36	2117	1648	26
	1420 / 3^+	18		1396	59
	1347 / 4^+	19		1365	8
	687 / 2^+	27		723	7
2160 / 8^+	1528 / 8^+	100	2109	1490	99
	1524 / 6^+	-		1497	1
2223 / 8^+	2160 / 8^+	$\sim$1	2149	2109	1
	1524 / 6^+	39		1497	70
	1528 / 8^+	61		1490	29
2281 / 5^+	2042 / 6^+	-	2282	2045	6
	1583 / 4^+	-		1648	3
	1524 / 6^+	-		1497	15
	1347 / 4^+	100		1365	75
2294 / 6^+	2042 / 6^+	12	2283	2045	11
	1583 / 4^+	13		1648	10
	1524 / 6^+	41		1497	38
	1528 / 8^+	3		1490	1
	1347 / 4^+	31		1365	41
2336 / 7^+	2160 / 8^+	-	2314	2109	1
	2042 / 6^+	12		2045	14
	1524 / 6^+	15		1497	21
	1528 / 8^+	74		1490	64

Table 6.1 – *Continued.*

Experiment			Shell Model		
E_i (keV) / J_i^π	E_f (keV)/ J_f^π	BR$_\gamma$ (%)	E_i (keV)	E_f (keV)	BR$_\gamma$ (%)
2369 / 7^-	1528 / 8^+	12	2357	1490	0.3
	1524 / 6^+	88		1497	100
2415 / $\ast 7^+$	2223 / 8^+	-	2387	2149	4
	2160 / *8^+	7		2109	6
	2042 / 6^+	16		2045	4
	1524 / 6^+	11		1497	7
	1528 / 8^+	66		1490	79
2438 / 5^+	2042 / 6^+	-	2401	2045	2
	1583 / 4^+	-		1648	3
	1524 / 6^+	-		1497	29
	1420 / 3^+	100		1396	61
	1347 / 4^+	-		1365	3
2508 / *6^+	2415 / $\ast 7^+$	-	2485	2387	1
	2336 / 7^+	-		2314	1
	2294 / 6^+	5		2283	7
	2281 / *5^+	-		2282	1
	2042 / 6^+	-		2045	3
	1583 / 4^+	10		1648	2
	1524 / 6^+	85		1497	83
	1528 / 8^+	-		1490	1
2527 / 5^+	2294 / 6^+	-	2572	2283	5
	2281 / *5^+	-		2282	5
	2149 / *4^+	-		2117	9
	2042 / 6^+	20		2045	23
	- / 4^+	-		2005	4
	1583 / 4^+	-		1648	8
	1524 / 6^+	20		1497	30
	1420 / 3^+	13		1396	2
	1347 / 4^+	47		1365	13
2556 / 7^+	2369 / 7^-	2	$2732^{b)}$	2357	<1
	2336 / 7^+	-		2314	4
	2294 / 6^+	2		2283	<1
	2223 / 8^+	10		2149	45
	2160 / *8^+	5		2109	3
	2042 / 6^+	-		2045	11
	1524 / 6^+	-		1497	5
	1528 / 8^+	81		1490	32

Table 6.1 – *Continued.*

Experiment			Shell Model		
E_i (keV) / J_i^π	E_f (keV)/ J_f^π	BR$_\gamma$ (%)	E_i (keV)	E_f (keV)	BR$_\gamma$ (%)
2575 / *6$^-$	2369 / 7$^-$	97	2553	2357	100
	1524 / 6$^+$	3		1497	<1

[a] Due to the inversion of the 6$^+$ and 8$^+$ states, no branching ratio could be calculated, however the theoretical B(E2) value (∼1 W.u.) indicates the existence of a transition between the two states.
[b] There is a 7$^+$ state predicted at 2618 keV, which is closer to the experimental value. However its decay pattern is very different from that observed experimentally.

Similar to the prior shell model calculations the $\pi h_{9/2}^2$ seniority scheme is again successfully reproduced, with energies closer to those observed experimentally. The energy gap between the 8$^+$ and 6$^+$ $\pi h_{9/2}^2$ states reflects that of the measured 4 keV energy gap, however the ordering of the two states is inverted in the calculations.

For all experimental states below 2.6 MeV, a good agreement between the shell model and experimental level scheme is observed, with energy differences never exceeding 100 keV. The exceptions to this are the 2556 keV 7$^+$ state with an energy difference of 176 keV and the 2402 keV level which has been assigned 3$^-$ or 4$^+$ spin-parity. There is a 4$^+$ state with similar energy predicted by the shell model calculations at 2473 keV, however the decay pattern of this state does not match with what was observed. Furthermore, the closest 3$^-$ state predicted in the present model space is at 2824 keV and is therefore unlikely to correspond to the 2402 keV level. Thus, we do not have a preferred spin-parity assignment or predicted state for the 2402 keV level. Lastly, the 1995 keV 3$^-$ state again has no corresponding predicted state. This again suggests the possibility of a collective octupole state, which is not reproducible with the calculations and model space used.

6.1.3 logft Comparison

Calculations were also carried out to determine theoretical logft values for populated states using intensity imbalances and the NNDC logft calculator (ref. [81]). These could then be used both for comparison with measured values, as well as to identify as-yet-unobserved, highly-populated states. Unfortunately due to the complexity and ambiguity of forbidden decays, these calculations were only performed for allowed decays (populating states with $J^{\pi} = 5^{+}, 6^{+}$, or 7^{+}). Strong configuration mixing for non-yrast states combined with the limited model space results in these calculated values providing little utility for logft comparison. The only state for which meaningful conclusions could be drawn is the 1524 keV 6^{+} state, with theoretical logft=8.15, unfortunately due to the significant intensity error bars no accurate logft could be determined for this state and thus no meaningful comparison could be made.

6.1.4 Unresolved logft Values

For some states, logft values were used in conjunction with expected logft ranges (taken from ref. [23]) to limit spin-parity assignments. The logft values themselves were calculated using γ intensity imbalances, however, in two instances this method yielded logft values inconsistent with prior studies. The following sections detail the logft calculations and analysis for these states.

2160 keV logft Calculation

Prior to this analysis, the 2160 keV state had a spin-parity assignment of 8^{+} and an intensity imbalance (the difference in γ-ray intensity between transitions onto and originating from a given state) of +1.61(35) [3]. Despite this significant imbalance a logft value was not calculated, likely due to it requiring a heavily suppressed second-forbidden decay to populate the state. As a consequence it is more likely inaccuracies in intensity calculations and/or unobserved transitions are responsible for the high imbalance.

Following the analysis conducted for this dataset the intensity imbalance was lowered to +1.08(50). This was due in part to the new 62 keV transition found to populate it. Although significantly lower, this still yields a logft value of 8.26(21) which falls outside of the expected range for second-forbidden decays of 10.6-14.2 [23]. Therefore, a similar conclusion to prior analysis has been made, that the imbalance is more likely the result of inaccuracies in intensity calculations and/or unobserved transitions and thus no logft is quoted in the final results.

2149 keV logft Calculation

The 2149 keV state was assigned a spin-parity of $3^+, 4^+, 5^+$ in prior decay studies, with an intensity imbalance of +1.21(10). Despite the possibility that it could be populated via allowed decay, again a $\log ft$ was not determined in previous decay studies. This is most likely due to the 2149 keV state's position in the level scheme being tentative, as well as the spin-parity assignment not restricting higher order decays.

In this analysis the 2149 keV state was confirmed, and its spin-parity was restricted by new, populating transitions to $3^+, 4^+$ excluding the possibility of population via allowed decay. Therefore, despite the lower intensity imbalance of +1.0(4) reducing to $\log ft$ value to 8.3(2), this again falls outside the $\log ft$ range for second-forbidden decays. Thus, similar to the 2160 keV state, it is not included in these results.

6.2 Beta Decay States

Positive and negative parity states are both fed directly in the β^+/EC decay of ^{208}At. As detailed in Section 2.2.3 lower spin-parity changes result in more favourable decay paths, thus, as ^{208}At decays from a 6^+ ground state, forbidden decays to negative parity states will be less favoured. However, according to the present work, $\sim$44% of the decay proceeds via allowed β decay, and $\sim$46% via first-forbidden, with the remaining $\sim$10% decaying to states of unknown parity. Given that forbidden decays are heavily suppressed this near equivalent population is unusual, but not unexpected.

Section 2.2.3 outlined how the large role of first-forbidden decays can be qualitatively understood through shell model considerations. For ^{208}At, all allowed decay paths are obstructed by fully occupied orbitals, whereas first-forbidden decays are unimpeded by the underlying shell structure. Core-excitation is required for these decays, and as a consequence the populated states have excitation energies around 3-4.5 MeV. Thus, a large number of populated negative parity states are expected in this energy region. Despite these shell model considerations limiting potential allowed decays, first-forbidden decays are still suppressed and thus will predominantly be sparsely populated.

6.2.1 The Pandemonium Effect

The high energy and β-restricted spin-parity of first-forbidden populated states results in them decaying predominantly via high energy transitions due to γ decay selection rules. As gamma detection efficiency decreases with increasing energy, smaller, lower-efficiency detectors will not observe these high-energy decays. These factors can cause issues when considering β decay branches.

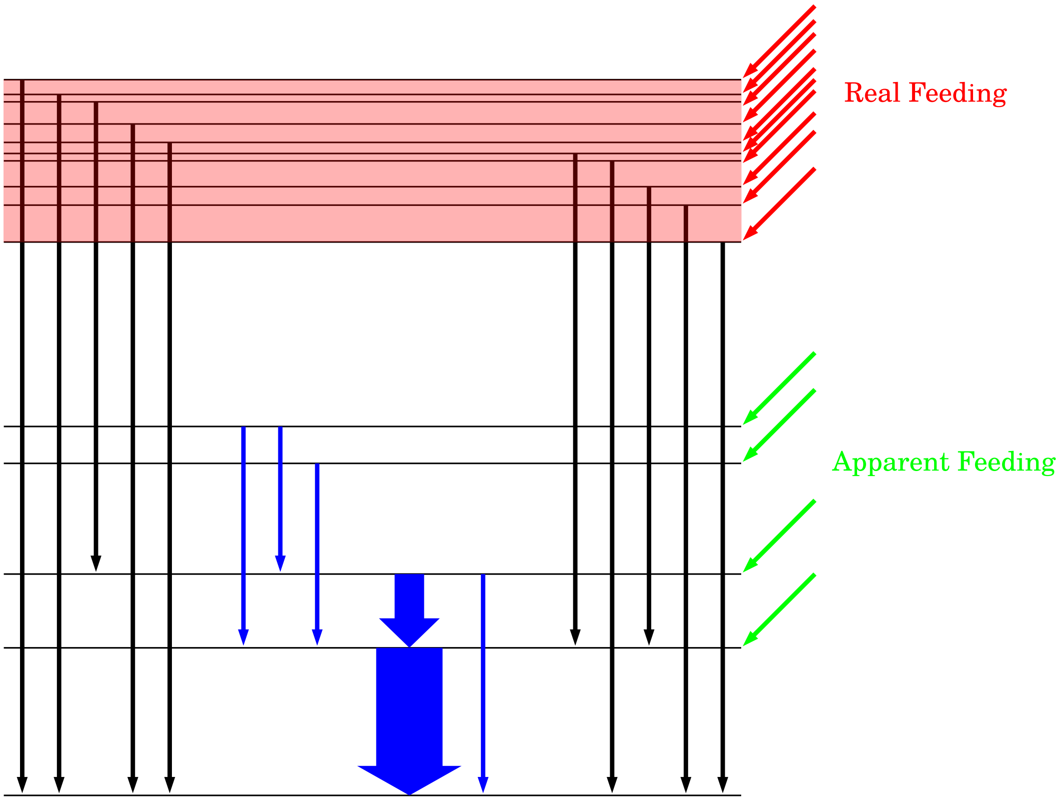

Figure 6.3: Illustration of the pandemonium effect. Observed low-energy gamma rays are shown in blue, unobserved high-energy gamma rays are in black. The "Apparent Feeding" refers to the decays observed when only the blue transitions are measured, and are thus overestimated. The "Real Feeding" refers to decays which are not observed when only the blue transitions are observed and are thus underestimated. The red shaded region represents the high-energy states where beta feeding is underestimated.

Figure 6.3 demonstrates the effect of low γ detection efficiency on β decay experiments. Only the low energy and/or high intensity decays are able to be observed, resulting in a number of high energy transitions left unmeasured. As a consequence, the initial states are not observed, and the intensity imbalances of the low-lying final states are incorrect. The overall effect of this is an overestimation of β feeding to low energy states with high energy states being underestimated or unobserved, this phenomenon is known as the Pandemonium effect [82].

The Pandemonium effect is most easily visualised by comparing previous decay studies of the same nucleus. This is achieved by plotting β feeding intensity as a function of excited state energy for multiple experimental datasets. Figure 6.4 shows these data for ^{208}Po from this analysis and two previous experiments.

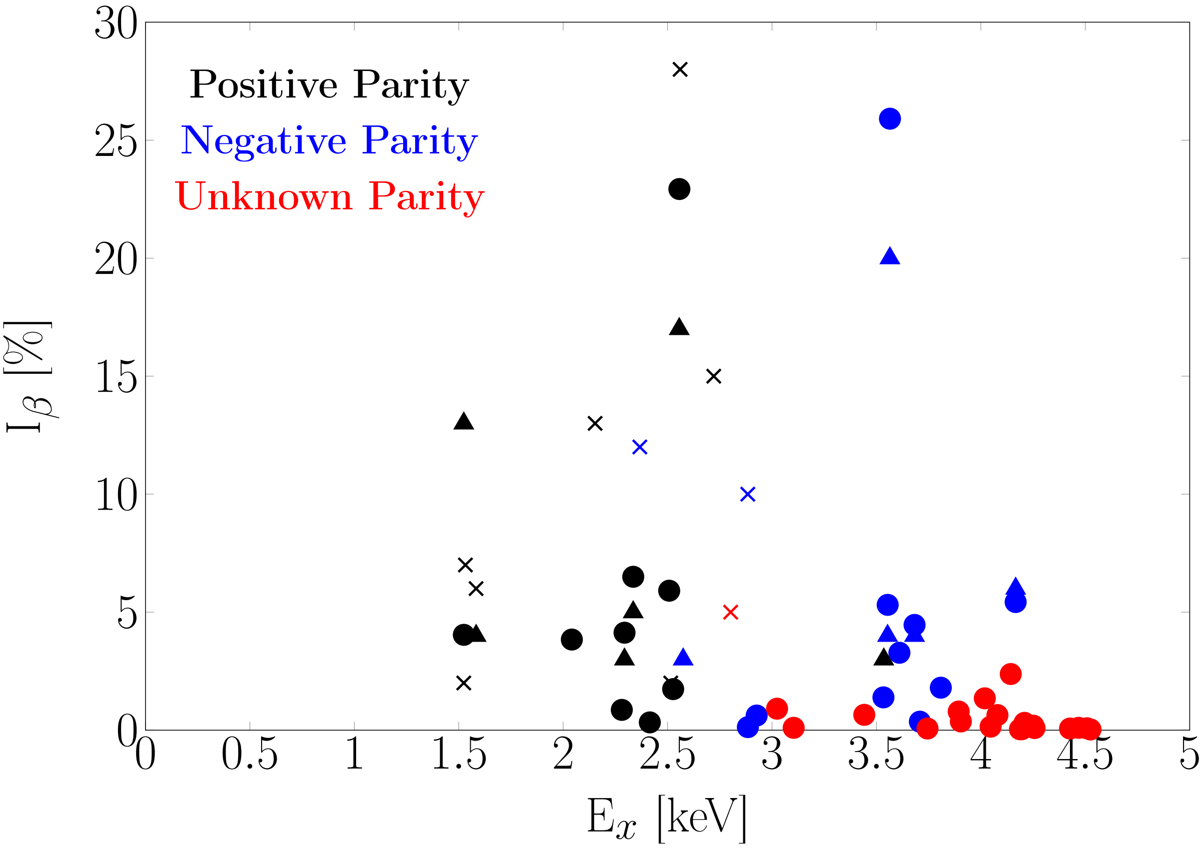

Figure 6.4: beta-population intensity as function of the ^{208}Po excitation energy. The present results are indicated with filled circles (•) These are compared with result obtained from experiments performed in the 1960s [73] (×) and the the 1980s [3] (▲). The parity of the excited states is indicated by the colour of the symbol.

Naturally, older experiments were performed with much smaller, less efficient detectors, and hence the Pandemonium effect can be seen most clearly by comparison to the 1968 experiment. The largest detector used by Treytl et al [73] in the 1960s was a 32 cm^3 Ge(Li) detector. Consequently no excited states above 2.9 MeV were observed, and the amount of feeding to negative parity states via first-forbidden decay was only $\sim$ 22% (with $\sim$5% to unknown parity).

Subsequent experiments in the 1980s were performed with slightly larger Ge(Li) detectors, with volumes of up to 50 cm^3 [4, 68] and 13% relative efficiency [46]. Using these detectors, a greater proportion of high energy γ rays could be observed and placed within the level scheme, which allowed for more high-energy states to be identified. The structure of ^{208}Po (mentioned previously), results in the majority of these states having negative parity, thus the fraction of observed first-forbidden β decays increased to $\sim$37% [3].

By comparison the large crystal size of the HPGe detectors at the IDS ,$\sim$250 cm^3 [83], allowed for the identification of yet more weak, high-energy transitions, with the weakest at the level of 10^{-2} per 100 β decays. It would be expected that this improvement in detection efficiency would result in another significant increase in the proportion of first-forbidden decays, similar to the 15% increase seen between the 1968 and 1980s experiments. Although a change is observed it is smaller than the previous increase as the proportion of first-forbidden decays only increases by 9% to 46%. Although several new, high-energy states were observed (see Figure 6.4) most have low β intensity reducing their impact on the first-forbidden proportion. However, several new, beta-populated states of unknown parity were observed in the expected energy region for levels populated via first-forbidden decay. Therefore, it is likely they are predominantly negative parity states which would increase the proportion of first-forbidden decays even more. Further analysis would be required to confirm the spin-parity of these states however, as the dataset presented has insufficient statistics for this.

6.2.2 Proportion of First-Forbidden Decays

As explored in Section 3.1.2 the proportion of first-forbidden decays is significant for heavy nuclei. Figures 2.14a and 2.14b and Section 2.2.3 showed that this is due to the structure around the Z=82 and N=126 shell closures which suppresses allowed decay paths.

As this phenomenon is dependent on shell structure and not a unique characteristic of ^{208}At or its daughter nucleus, we can observe this competition in many nuclei around ^{208}At. Figure 6.5 shows first-forbidden decay systematics for the region surrounding ^{208}At relative to all decays.

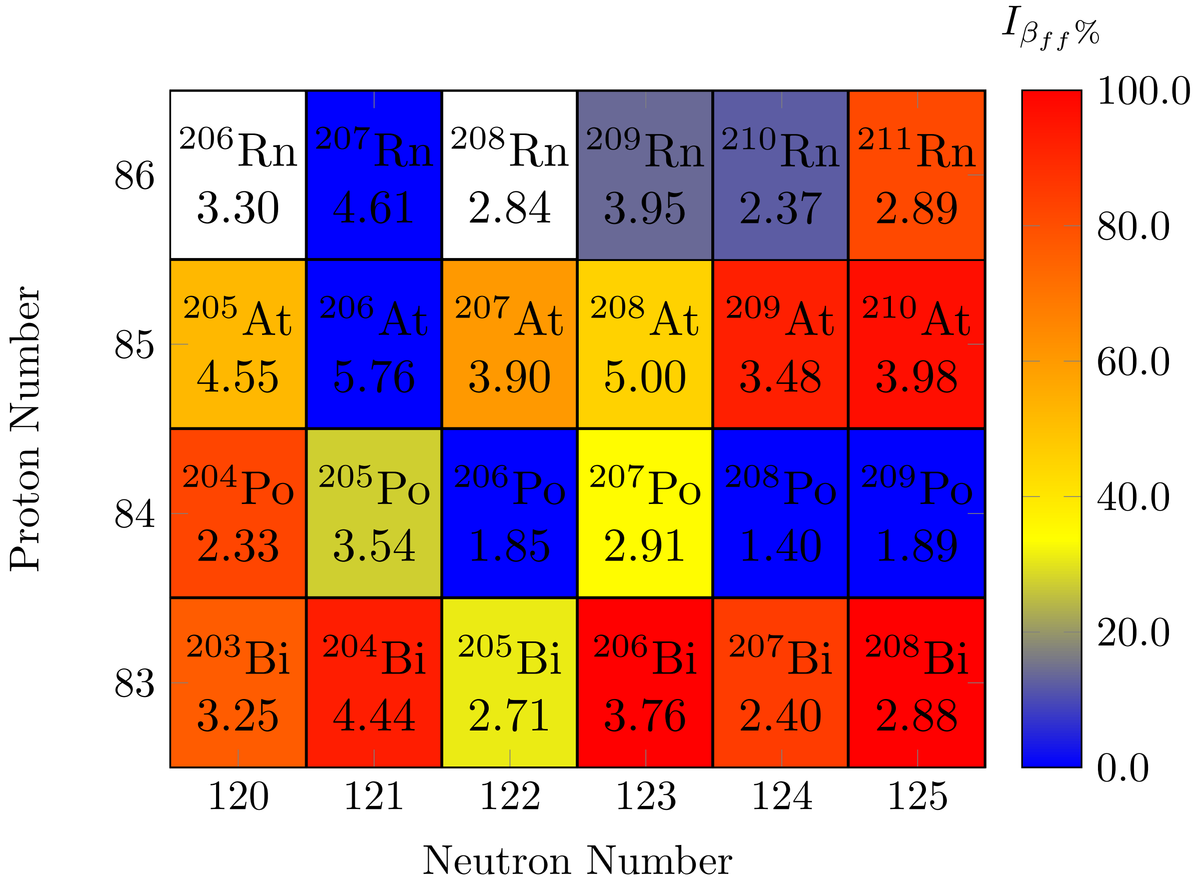

Figure 6.5: Intensity of first-forbidden decays ($I_{\beta_{ff}}\%$) for proton rich A∼208 nuclei [3, 25–27, 84–88]. The percentage of first-forbidden decays ($I_{\beta_{ff}}\%$) is given by $I_{\beta_{ff}}/I_{\beta_{tot.}}$. The parent nuclei are indicated. Q_{EC} values, in MeV, are also given. In the majority of nuclei competition between first-forbidden and allowed β decay is expected. For details, see the text.

Immediately clear from Figure 6.5 is that, as expected, prior decay studies have concluded that the vast majority of nuclei in the region decay with a strong first-forbidden component (most $>$ 40%). There are however some notable exceptions, namely ^{206,208,209}Po, ^{206}At and $^{206-210}$Rn. The following sections give further detail into these nuclei and why they deviate from the typical levels expected for the region, as well as other nuclei featured in Figure 6.5 with notable characteristics.

^{206,208,209}Po

For ^{206,208,209}Po each nucleus features a low Q_{EC} value which limits the possible decays to low energy states. Bismuth-206 features a large number of states below the Q_{EC} value, and as such ^{206}Po can decay predominantly via allowed decays. By contrast ^{208}Bi and ^{209}Bi have very few low energy states and thus the decays proceed via the lowest order decay path, which is second-forbidden in both cases.

^{209}Rn

The low first-forbidden proportion of ^{209}Rn is due in part to insufficient data. The most recent investigation of ^{209}Rn utilised three small Ge(Li) detectors with volumes 0.5, 8.2 and 3.7 cm^3 [89]. Given their small size, and thus low detection efficiency, it is very likely that first-forbidden decays to ^{209}At are currently being underestimated as a result of the Pandemonium effect. Of the states in ^{209}At which have been observed to be populated via β^+/EC decay, over 40% have no parity assignment and were thus not included in determining $I_{\beta_{ff}\%}$. With most of the unknown-parity states having energies >2.5 MeV, it seems likely that further investigation would yield more as-yet-undetermined higher order decays.

^{210}Rn

Similar to ^{206,208,209}Po the low $I_{\beta_{ff}}\%$ value for ^{210}Rn is also the result of its Q_{EC} value. The observed negative parity states in ^{210}At which can be populated via β^+/EC decay (1967 keV and 2281 keV) lie just below the Q_{EC} value of ^{210}Rn (2367 keV [87]) and are therefore energetically unfavourable. Unlike ^{209}Rn, the lower Q_{EC} value of ^{210}Rn makes the discovery of many more higher order decays unlikely.

^{208}Bi

Although the $I_{\beta_{ff}\%}$ for ^{208}Bi is 100%, it is notable as it is also the result of low Q_{EC} values in the parent nucleus. Lead-208 has a limited number of excited states within the Q_{EC} window, thus its parent nucleus decays via the lowest degree of forbiddeness which for ^{208}Bi is at least first-forbidden. Thus ^{208}Bi has a high $I_{\beta_{ff}\%}$ value compared to ^{205}Bi which has a comparable Q_{EC} value.

^{206}At

The current level scheme for ^{206}Po features only one confirmed negative parity state (9^- [27]) below the Q_{EC} value which, given the 5^+ spin-parity of the decaying ^{206}At ground state, is heavily suppressed. However, as with the decay of ^{209}Rn, the level scheme also features a number of high-lying states which have yet to be assigned a spin-parity. Further analysis with improved detection methods may yield more information, and increase the proportion of first-forbidden decays.

^{206,207,208}Rn

The isotopes of ^{206,207,208}Rn are some of the least stable featured in Figure 6.5, and as such data on their respective decays is scarce. However the high Q_{EC} value of ^{207}Rn and moderate Q_{EC} value of ^{206}Rn would suggest that a notable proportion of first-forbidden decays could be observed for these nuclei.

The exceptions listed above can be placed into two categories: low Q_{EC} value (210Rn, ^{206,208}Po), or insufficient data and/or a lack unsuppressed decay paths (^{206,207,208,209}Rn, ^{206}At, ^{208,209}Po). For the latter case in some instances (e.g. ^{209}Po) it is unlikely further study will significantly alter the results presented in Figure 6.5. Most however, namely ^{206}At and ^{207}Rn, have Q_{EC} values which would suggest a number of unobserved and/or underestimated decay paths. For the low Q_{EC} isotopes, it is notable that in each instance an even-even parent nucleus is decaying to an odd-odd daughter. It the Q-value staggering between odd-odd and even-even nuclei (explored in Section 2.2.3) which results in the low Q_{EC} values observed. This limits the potential decay paths for these isotopes to low energy states which, for this mass region, will exclude many first forbidden decays.

For all other nuclei in the region, as expected first-forbidden decay competes strongly with allowed transitions. Many decays have not been studied with modern, high detection efficiency and are therefore susceptible to the Pandemonium effect obscuring these conclusions. These data strongly suggest that high-yield decay studies of nuclei in the N$\sim$126 region can expand the understanding of the structure of the daughter nucleus, through population of high-lying, negative parity states. This in turn, allows for a clearer picture of the proportion of first-forbidden decays. The high Q_{EC} values and data scarcity for a number of Rn and At nuclei would make them prime candidates for these future studies.

6.2.3 Implications for r-process Nucleosynthesis

First-forbidden decays are becoming increasingly relevant with respect to r-process nucleosynthesis simulations (as was explained in Section 3.1.2). As decay data for the N$\sim$126 region remains scarce for β^--decaying nuclei, half-life measurements for the region are limited and do not stray far from stability. Consequently there is a heavy reliance on half-life estimates which, for the N$\sim$126 region, require an understanding of first-forbidden decays. The high first-forbidden proportion of nuclei above the valley of stability around the ^{208}At region, is similar to that of *r*-process nuclei. Consequently, experimental data on these nuclei, such as the results presented here, can be used to broaden the understanding of first-forbidden decays more generally. These conclusions can then be utilised to corroborate and improve theoretical calculations which consider the effects of higher order decays. Thus, by broadening understanding of first-forbidden decay proportion for nuclei in the Z>82, N<126 region, it can provide insight into the decay paths of *r*-process nuclei, *r*-process nucleosynthesis, and nuclear structure more generally.

6.3 3$^-$ State Implications

The abundance of $\Delta l = \Delta j = 3$ single particle excitations around the Z = 82 and N = 126 shell gaps gives rise to collective octupole excitations, and hence low-lying 3$^-$ states, in the mass region. The most notable example of this is the 2614.5 keV [3] first, excited state of the doubly-magic ^{208}Pb nucleus (see Section 3.1.1). Consequently, low-lying 3^- states are not uncommon for A∼208 nuclei. Therefore, insight into the nature of the 1995 keV 3^- state identified in this analysis, can be acquired through comparison to low-lying 3^- states in surrounding nuclei. Figure 6.6 shows how the measured energies of the lowest 3^- states change with proton and neutron number for Hg, Pb, and Po nuclei.

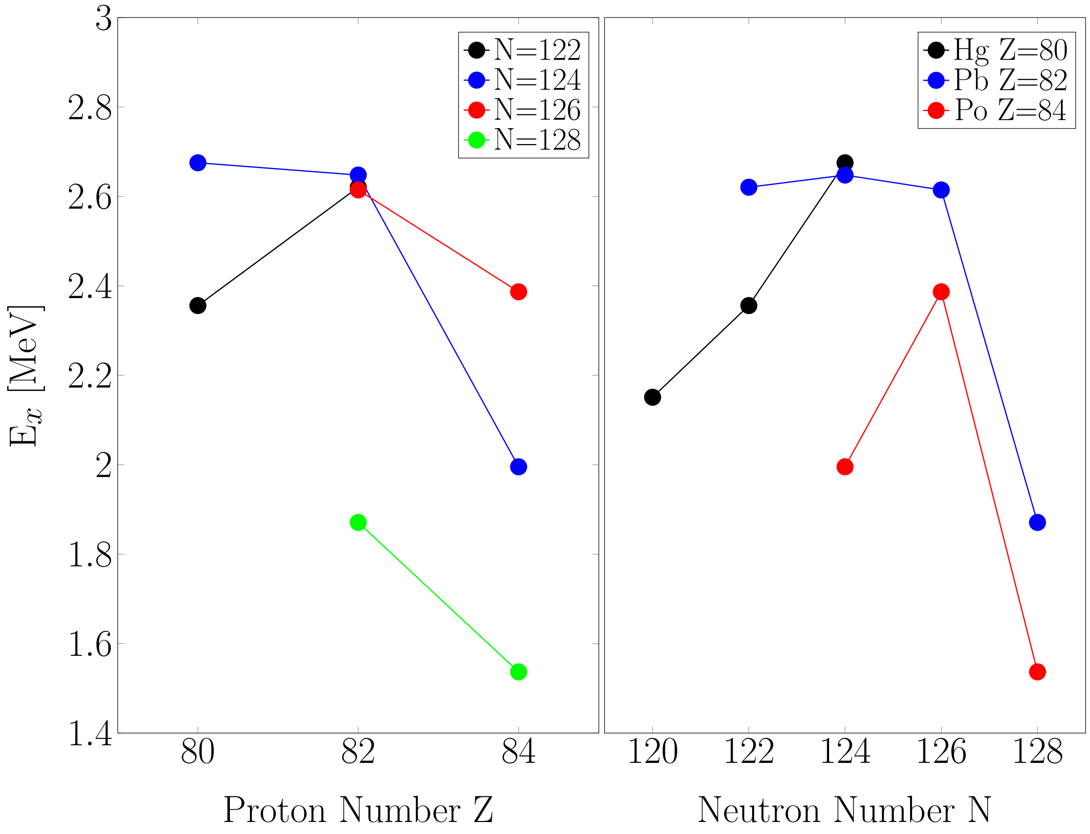

1

Figure 6.6: Systematics of the lowest energy 3^- states in even-even nuclei around the Z = 82 shell closure as a function of neutron and proton number. Values aggregated from Nuclear Data Sheets (Pt[90–93], Hg[85, 93–95], Pb[3, 27, 85, 87], and Po[3, 87, 96, 97]).

It is clear from these graphs that there is a disparity between the energy shifts of valence particle nuclei and valence hole nuclei. A significant energy shift is observed for all Z = 84 and N = 128 nuclei, by contrast, energy shifts are only observed in N = 124 and Z = 80 nuclei when more than two valence nucleons are present. This trend can be understood by examining the proton and neutron orbitals involved. Figure 6.7 gives the energies and quantum numbers for the single particle excitations around the Z = 82 and N = 126 shell gaps.

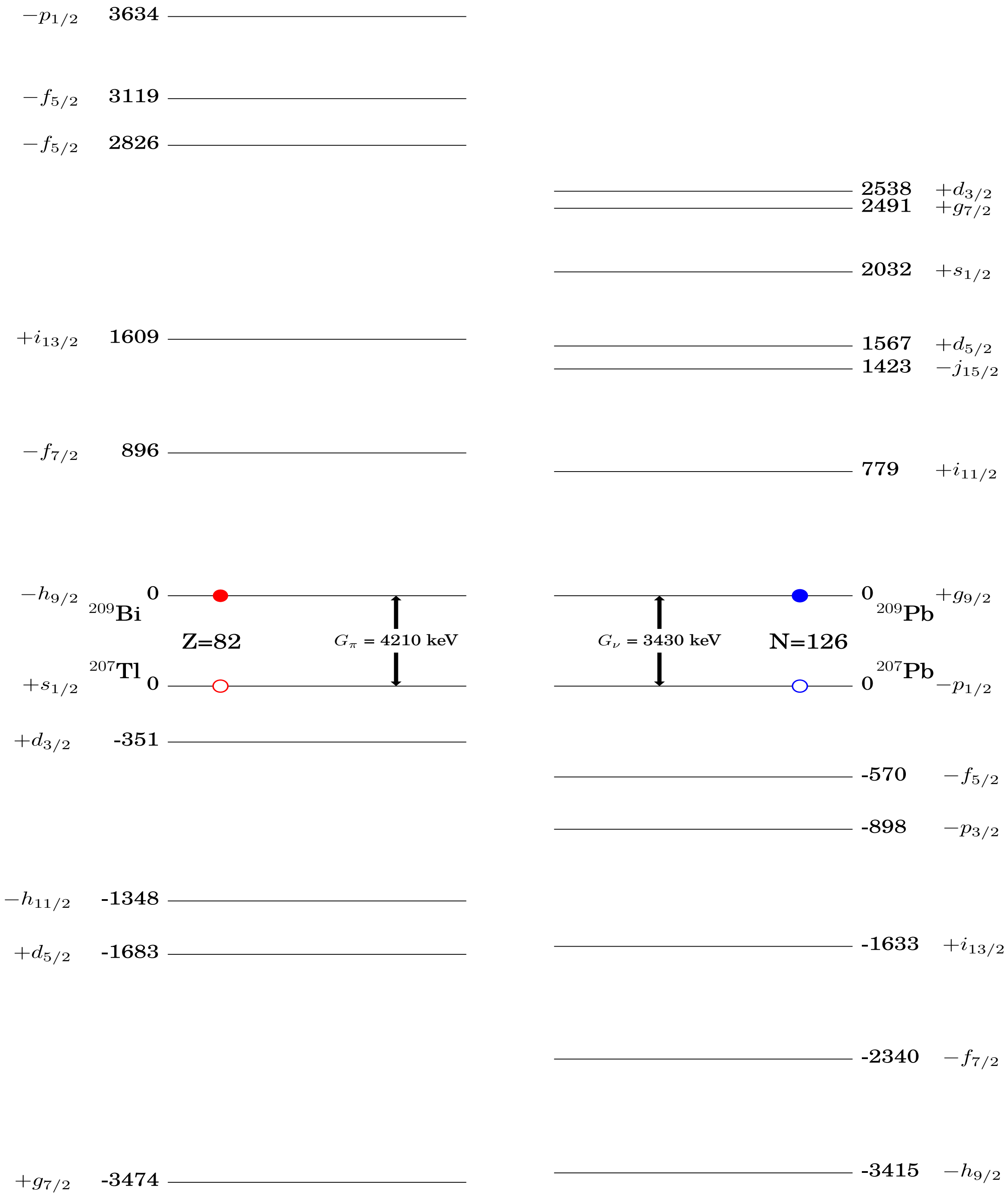

Figure 6.7: Single particle excitation energies around the Z = 82 and N = 126 shell gaps. Values taken from ^{207}Tl, ^{209}Bi, ^{207}Pb, and ^{209}Pb [25–27].

Particle and hole excitations for both protons and neutrons feature a wide range of spins, as well as both positive and negative parities. The key difference between them is how these spins and parities are distributed by energy. For particle excitations the low-lying orbitals are all high spin, whereas low-lying hole excitations are not. As a consequence, valence particle nuclei in this region are able to form lower-energy 3^- states with configurations such as $\pi h_{9/2} i_{13/2}$ and $\nu g_{9/2} j_{15/2}$. These excitations form with energies comparable to the 3^- core excitation which results in strong mixing between these states, and the energy of the core excited state splitting and shifting. Further discussion of this effect on the low-lying 3^- states in ^{210}Po and ^{210}Pb can be found in refs. [98] and [99], with detailed discussion of configuration mixing in ref. [100]. Conversely the low-lying orbitals in valence hole nuclei form 3^- states with significantly higher energies, and thus the core excited states remain mostly unperturbed.

In addition, valence-hole pairs increase the energy of certain $\Delta l = \Delta j = 3$ excitations, specifically $\pi s_{1/2} f_{7/2}$ and $\nu p_{1/2} g_{7/2}$, resulting in an increase in energy of the core excited state. This shift will mitigate some of the effect of mixing with hole excitations. An estimation of the energy shift of the $\nu p_{1/2} g_{7/2}$ excitation in ^{208}Po is given in Table 6.5. For ^{208}Po the energy of the lowest 3^- state is $\sim$400 keV lower than that observed in ^{210}Po, thus attributing this solely to the effect of proton particle excitations is likely oversimplified. For a more complete description of this behaviour we must consider the impact of the valence neutron holes in combination with valence proton particles, as well as the composition of the core-excited state itself.

States with 3^- spin-parity in ^{208}Po cannot be populated directly through β^+/EC decay due to their low spin. Likewise, internal γ population is unlikely due to their comparably high energy. It is unsurprising therefore that no evidence of other 3^- states was observed in this analysis. Therefore, to further investigate the effect of the neutron hole pair and overall 3^- state density of ^{208}Po, theoretical calculations were conducted. Once again these calculations were performed with the NuShellX code [74], using the same parameters described in Section 6.1.2, and as such do not consider core excitations. Similar calculations were also carried out for ^{206}Pb and ^{210}Po to explore the configurations of 3^- states formed in valence-neutron-hole-pair and valence-proton-particle-pair nuclei respectively. Tables 6.2 and 6.3 give the energies and dominant proton and neutron hole configurations for predicted 3^- states in ^{206}Pb and ^{210}Po. Table 6.4 gives the ten lowest energy predicted 3^- states in ^{208}Po, as well as the higher energy states with dominant configurations corresponding to the neutron-hole excitations of ^{206}Pb.

Table 6.2: Dominant neutron-hole configurations for all 3^- states predicted in ^{206}Pb below 5.5 MeV.

		^{206}Pb		
State Number	Energy (keV)	Proton Config	Neutron Config	%
1	4180	-	$f_{7/2}i_{13/2}$	~100
2	5478	-	$h_{9/2}i_{13/2}$	~100

Table 6.3: Dominant proton configurations for all 3^- states predicted in ^{210}Po below 5.5 MeV.

		^{210}Po		
State Number	Energy (keV)	Proton Config.	Neutron Config.	%
1	2998	$h_{9/2}i_{13/2}$	-	~100
2	3577	$f_{7/2}i_{13/2}$	-	~100

Table 6.2 reaffirms the high energy of neutron-hole 3^- excitations in this region, and thus their reduced mixing with lower-energy, core-excited states. Examining the predicted 3^- states in ^{208}Po, as expected both the low energy proton particle and high energy neutron hole configurations of ^{210}Po and ^{206}Pb respectively, feature in ^{208}Po at comparable energies (shown in **bold** in Table 6.4).

Immediately apparent by comparison of the three tables, is the abundance and density of 3^- states in ^{208}Po, with eight states between 2.8 MeV and 4 MeV. Study into the configurations of these states shows that they predominantly result from excitations which require both a proton particle pair and neutron hole pair component and as such, cannot be formed in either ^{206}Pb or ^{210}Po. Furthermore, as with the proton particle states in ^{210}Po, the valence nucleons in ^{208}Po are excited to low-lying proton and neutron orbitals, resulting in the high density of low energy states.

Mixing between 3^- states and the octupole excitation is dependent on both energy difference and the contribution of given $\Delta l = \Delta j = 3$ excitations to the core-excited state. Table 6.5 shows the energies and forward amplitudes of $\Delta l = \Delta j = 3$ excitations in ^{208}Pb, ^{208}Po, with energies calculated from single-particle excitations and forward amplitudes taken from ref. [101].

As ^{208}Po does not require excitations across the Z = 82 or N = 126 shell gaps for $f_{7/2}i_{13/2}$

Table 6.4: Dominant proton and neutron-hole configurations for the first ten predicted 3^- states in ^{208}Po. States which correspond to two-proton or two-neutron-hole states in ^{210}Po and ^{206}Pb respectively are shown in bold. Due to their higher energy, three additional states are shown for comparison to the neutron-hole states in ^{206}Pb.

^{208}Po

State Number	Energy (keV)	Proton Config.	Neutron Config.	%
1	**2834**	$\mathbf{h_{9/2}i_{13/2}}$	-	**44**
2	3505	$h_{9/2}i_{13/2}$	$f_{5/2}p_{1/2}$	40
3	**3588**	$\mathbf{f_{7/2}i_{13/2}}$	-	**20**
		$h_{9/2}i_{13/2}$	$f_{5/2}p_{1/2}$	18
4	**3617**	$h_{9/2}i_{13/2}$	$f_{5/2}p_{1/2}$	24
		$\mathbf{f_{7/2}i_{13/2}}$	-	**22**
5	3824	$h_{9/2}^2$	$p_{1/2}i_{13/2}$	54
6	3901	$h_{9/2}i_{13/2}$	$f_{5/2}p_{1/2}$	18
		$h_{9/2}i_{13/2}$	$f_{5/2}p_{1/2}$	14
7	3946	$h_{9/2}^2$	$p_{1/2}i_{13/2}$	33
8	3975	$h_{9/2}i_{13/2}$	$f_{5/2}p_{1/2}$	27
		$h_{9/2}^2$	$p_{1/2}i_{13/2}$	23
9	4042	$h_{9/2}i_{13/2}$	-	18
		$h_{9/2}i_{13/2}$	$p_{3/2}p_{1/2}$	16
10	4075	$h_{9/2}^2$	$p_{1/2}i_{13/2}$	35
		$h_{9/2}i_{13/2}$	$f_{5/2}p_{1/2}$	20
		$h_{9/2}^2$	$p_{1/2}i_{13/2}$	15

Neutron-hole states at higher energies

13	**4158**	$h_{9/2}^2$	$p_{1/2}i_{13/2}$	23
		$h_{9/2}^2$	$f_{5/2}i_{13/2}$	16
		-	$\mathbf{f_{7/2}i_{13/2}}$	**11**
25	**4503**	$h_{9/2}^2$	$f_{5/2}p_{1/2}$	24
		-	$\mathbf{f_{7/2}i_{13/2}}$	**16**
129	**5763**	-	$\mathbf{h_{9/2}i_{13/2}}$	**28**

states, the energy of these excitations is drastically lower. As a consequence, the contributions of these excitations to the octupole state will be much greater, resulting in strong configuration mixing between $f_{7/2}i_{13/2}$ states and the octupole.

In addition, for ^{208}Po the $f_{7/2}i_{13/2}$ proton and neutron-hole configurations are dominant in multiple states below 5 MeV, including a 4464 keV state not listed in Table 6.4. Although mixing will be weaker than that of the states in ^{206}Pb and ^{210}Po which are 100% $f_{7/2}i_{13/2}$, the quantity of states which strongly feature this configuration will still result in a significant energy shift. Furthermore, ^{208}Po is unique in that both the proton and neutron-hole $f_{7/2}i_{13/2}$ configurations

Table 6.5: Energies and amplitudes for $\Delta l = \Delta j = 3$ excitations in ^{208}Pb and ^{208}Po. Amplitudes for ^{208}Pb are taken from ref. [101]. Differences in energy between ^{208}Pb and ^{208}Po are shown in red.

Configuration	^{208}Pb Energy (keV)	^{208}Po Energy (keV)	^{208}Pb Amplitude
$\nu p_{3/2} g_{9/2}$	4328	4328	0.44
$\pi d_{3/2} h_{9/2}$	4561	4561	0.36
$\nu f_{5/2} i_{11/2}$	4779	4779	0.37
$\pi s_{1/2} f_{7/2}$	5106	5106	0.26
$\nu p_{1/2} g_{7/2}$	5921	**7061**	-
$\nu f_{7/2} s_{1/2}$	7802	7802	-
$\nu h_{9/2} d_{3/2}$	9383	9383	-
$\nu f_{7/2} i_{13/2}$	10,833	**3973**	-
$\pi f_{7/2} i_{13/2}$	10,925	**2505**	-
$\pi g_{7/2} p_{1/2}$	11,318	11,318	-

will feature strongly in the core-excited state, which will further amplify mixing effects.

Configuration mixing can be approximated using predicted 3^- states from shell model calculations, an additional state to represent the octupole, and estimations of interaction matrix elements. These first two factors can be easily determined, with 3^- states listed in Table 6.4 (plus the unlisted 4464 keV state), and the core-excited state can be equated to the ^{208}Pb octupole phonon at 2614.5 keV.

The interaction matrix elements are more challenging to determine, due to the lack of comparable data in the $A \sim 208$ mass region. Instead, comparisons were made with lower mass nuclei around ^{146}Gd, detailed in ref. [102]. The number of possible $\Delta l = \Delta j = 3$ states is much lower for these nuclei, which causes the octupole to be highly dominated by the low energy $\pi d_{5/2} h_{11/2}$ configuration. Thus, the interaction matrix element for this configuration is very high at 1.13 MeV [102]. By comparison, the octupole state for ^{208}Po is more fragmented as shown in Table 6.5, however the low energies of the $\pi f_{7/2} i_{13/2}$ and $\nu f^{-1}_{7/2} i^{-1}_{13/2}$ excitations are expected to feature prominently. Consequently, $f_{7/2} i_{13/2}$ states will mix strongly with both components, and as such it is estimated that the interaction matrix elements will be comparable to that of $\pi d_{5/2} h_{11/2}$ in A∼146 nuclei. It is expected that the interaction matrix element will be slightly lower than 1.13 MeV as the octupole is more fragmented, thus a value of 0.8 MeV was selected for mixing calculations.

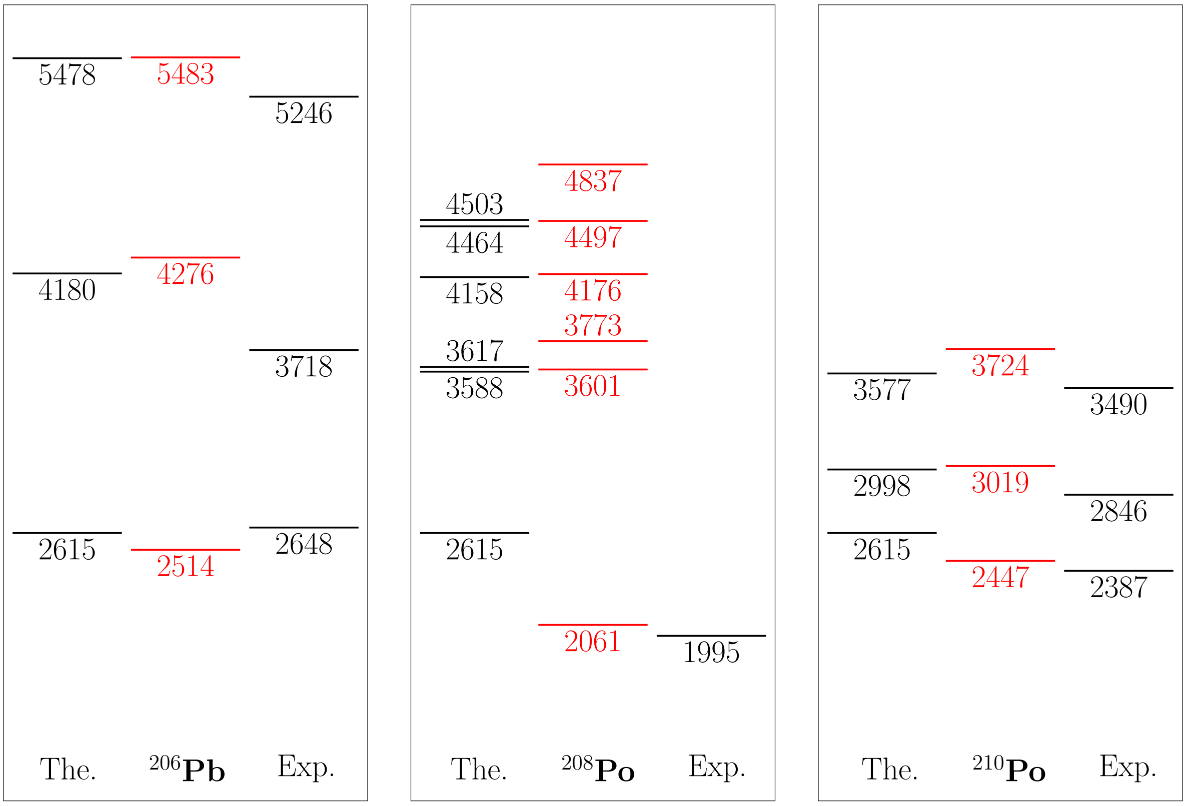

Figure 6.8: Level structures of ^{206}Pb, ^{208}Po, and ^{210}Po produced through configuration mixing. For each nucleus, "The." is the level structure based on shell model calculations of states used for configuration mixing, with an additional state included with energy equal to the ^{208}Pb octupole. Centre (red): Level structure resulting from simulation of configuration mixing of the "The." structure. Interaction matrix elements taken from ref. [101, 102]. "Exp." shows the experimentally observed 3^- states.

Mixing calculations were performed for ^{206}Pb, ^{208}Po, and ^{210}Po using the interaction matrix elements for $f_{7/2}i_{13/2}$ (0.8 MeV determined from ref. [102]) and $\Delta l \neq \Delta j \neq 3$ states (0.12 MeV taken from ref. [101]). These values were adjusted based on configuration percentages provided by shell model calculations, as well as the estimated amplitude of $f_{7/2}i_{13/2}$ configurations in the octupole. The interaction matrices used for each nucleus are given below, and the level structures produced are shown in Figure 6.8.

$$\begin{pmatrix} 2615 & 400 & 120 \\ 400 & 4180 & 0 \\ 120 & 0 & 5478 \end{pmatrix} \qquad \begin{pmatrix} 2615 & 426 & 448 & 242 & 761 & 303 \\ 426 & 3588 & 0 & 0 & 0 & 0 \\ 448 & 0 & 3617 & 0 & 0 & 0 \\ 242 & 0 & 0 & 4158 & 0 & 0 \\ 761 & 0 & 0 & 0 & 4464 & 0 \\ 303 & 0 & 0 & 0 & 0 & 4503 \end{pmatrix} \qquad \begin{pmatrix} 2615 & 120 & 400 \\ 120 & 2988 & 0 \\ 400 & 0 & 3577 \end{pmatrix}$$

^{206}Pb ^{208}Po ^{210}Po

The lowest 3^- state generated by the configuration mixing calculations is within 100 keV of the experimentally observed level for both polonium isotopes. For ^{208}Po this energy difference could be resolved by considering the weaker mixing effects of $\Delta l \neq \Delta j \neq 3$, 3^- states. The energy disparities could also result from the assumptions and estimations made in these calculations. These include the interaction matrix elements, the accuracy of the energies and configurations from the shell model calculations, and the energy of the core excited state. For ^{206}Pb, the larger energy difference of the lowest 3^- states is most likely due to an underestimation of the octupole energy. As with ^{208}Po, the $\nu p_{1/2}g_{7/2}$ excitation is higher in energy, which will affect the octupole and increase the energy of the lowest 3^- state. Increasing the energy of the octupole in the simulations to 2715 keV shifts the lowest energy state to 2608 keV which is considerably closer to the experimentally observed value.

While there are inaccuracies in these calculations, the factors listed are insufficient to invalidate the strong energy shift observed. We can therefore conclude that the low-lying nature of the 1995 keV 3^- state is the result of configuration mixing, consisting of both strong mixing with $f_{7/2}i_{13/2}$ states and weaker effects resulting from the abundance of other 3^- states in ^{208}Po. This can easily account for the $\sim$400 keV difference between the lowest ^{208}Po and ^{210}Po 3^- states.

6.3.1 Octupole Collectivity

Collective excitations are not considered in the majority of shell model calculations, including those conducted as part of this work. This is due to the complexity of simulating multiple particle excitations. In recent years some large-scale simulations of nuclei in this region have been able to successfully reproduce octupole states [76, 103], however the scope of these calculations remains limited with many featuring significant energy disparities. Due to this absence of theoretical data, experimental investigations of octupole collectivity remain the primary source of information for improving understanding.

Despite the prevalence of octupole collectivity in the region, beyond the 3^- spin-parity assignment, no indication of octupole collectivity was observed for the 1995 keV state in this analysis. It is worth noting however, that the position of the 1995 keV resembles that of the 1537 keV and 1870 keV 3^- states in ^{212}Po and ^{210}Pb respectively. The latter of which has a measured B(E3)=26(6) W. u. [104].

Further analysis of ^{208}Po is necessary to fully characterise the 1995 keV 3^- state, as well as to potentially observe higher-energy 3^- states predicted by shell model calculations which are unobserved in this analysis. Furthermore, a high statistics Coulomb excitation experiment would be beneficial for reaffirming the spin-parity of the 1995 keV state, as well as providing a measurement of the B(E3) value potentially confirming its collectivity.

Chapter 7

Conclusion

Through the analysis presented in this work, the level scheme of ^{208}Po has been greatly expanded and developed. A large number of states and transitions have been newly identified and a significant proportion of levels and γ rays observed in previous analysis have been firmly established within the level scheme for the first time. Measured intensity imbalances, using calculated internal conversion coefficients, were used to determine $\log ft$ values for all β^+/EC-populated states. Through a combination of, γ coincidence analysis; α_K values measured in prior decay studies; and $\log ft$ limits from ref. [23], restrictions on spin-parity were made for all observed states. A good agreement with shell model calculations was achieved for almost all low-lying states, and comparisons with expected branching ratios strengthened many spin-parity assignments. In addition, a new measurement of the 1528 keV isomer half-life was made, which was both in agreement with prior measurements whilst notably reducing the associated error.

A previously observed 1995 keV state was confirmed to be a low-lying 3^- state, which could not be successfully reproduced in standard shell model calculations. Through comparisons with other 3^- states in the region, and theoretical calculations and estimations, the low-lying nature of the state was found to result from significant configuration mixing. This predominantly consisted of strong configuration mixing with $f_{7/2}i_{13/2}$ states as well as weaker interactions with the other $\Delta l \neq \Delta j \neq 3$, 3^- states abundant in ^{208}Po. No evidence of octupole collectivity was observed in this analysis however, comparisons to neighbouring nuclei, specifically ^{210}Pb and ^{212}Po, would suggest some degree of collectivity.

Improvements in detector efficiency and beam production have allowed for the measurement and placement of many high energy and/or low intensity γ rays. As a consequence, high-lying β^{+}/EC populated states have been identified for the first time in this analysis. This has led to a reduction of the Pandemonium effect which obscures these states in lower-efficiency decay studies. For ^{208}At, many of these high-lying states have negative-parity thus, obscuring the decays to these states has the added effect of diminishing the observed proportion of forbidden decays. Improving understanding of these decays, particularly in the N$\sim$126 region where they are more prevalent, is crucial for refining theoretical models which require the simulation of β decay. In recent years, simulations of r-process nucleosynthesis have begun to recognise the influence of forbidden decays [37]. Despite decaying via β^{+}/EC decay, the current inaccessibility of many neutron-rich nuclei necessitates investigation of the decays of proton-rich nuclei to provide a broader picture of forbidden decays. In this respect, the data presented in this analysis can be adapted and implemented to improve large-scale decay studies of the region such as those investigating the *r*-process.

In conclusion, this analysis has substantially improved the understanding of states in ^{208}Po populated via β^{+}/EC decay. The valence nucleons and position of ^{208}Po in the nuclide chart offer a key testing ground of both collective and shell model states and their interactions within a nucleus. In addition, the observation of a low-lying 3^{-} state could provide insight for studies of octupole collectivity in the region, particularly for nuclei with more valence nucleons. Finally, the decay of ^{208}At and other nuclei in the region, offer an opportunity to study forbidden decay paths, an area that remains a topic of significant debate which can provide clarity for global decay studies in the region. Although large-scale calculations remain constrained by current computational limitations, the data presented here will contribute to their continuing development and future success.

Bibliography

[1] M. Goeppert-Mayer Phys. Rev., vol. 75, no. 12, p. 1969, 1949.

[2] Z. Podolyák et al. J. Phys. Conf. Ser., vol. 580, p. 012010, 2015.

[3] M. J. Martin Nucl. Data Sheets, vol. 108, p. 1583, 2007.

[4] V. M. Vakhtel et al. Izv. Akad. Nauk, vol. SSSR, pp. Ser. Fiz. 45, 1841 *[Engl. transl.: Bull. Acad. Sci. USSR, Phys. Ser.* ***45*** *no. 10, 29 (1981)*], 1981.

[5] B. S. Dzhelepov et al. Izv. Akad. Nauk, vol. SSSR, pp. Ser. Fiz. 47, 2 *[Engl. transl.: Bull. Acad. Sci. USSR, Phys. Ser.* ***47*** *no. 1, 1 (1983)*], 1983.

[6] D. Ivanenko Nature, vol. 129, p. 798, 1932.

[7] E. Gapon and D. Ivanenko Naturwissenschaften, vol. 20, no. 43, p. 792, 1932.

[8] M. Goeppert-Mayer Phys. Rev., vol. 78, no. 1, p. 16, 1950.

[9] M. Goeppert-Mayer Phys. Rev., vol. 78, no. 1, p. 22, 1950.

[10] B. L. Cohen, *Concepts of Nuclear Physics*. Tata McGraw-Hill Education, 1971.

[11] P. A. Tipler and R. Llewellyn, *Modern Physics*. Macmillan, 2003.

[12] R. F. Casten, *Nuclear Structure from a Simple Perspective*, vol. 23. Oxford University Press, 2000.

[13] K. Heyde, *Basic Ideas and Concepts in Nuclear Physics: An Introductory Approach*. CRC Press, 2004.

[14] K. S. Krane, D. Halliday, et al., *Introductory Nuclear Physics*. 1987.

[15] R. D. Woods and D. S. Saxon Phys. Rev., vol. 95, no. 2, p. 577, 1954.

[16] J. Dudek et al. J. Phys. G, vol. 5, no. 10, p. 1359, 1979.

[17] B. Povh et al., *Particles and Nuclei*, vol. 1. Springer, 1995.

[18] S. G. Nilsson Dan. Mat. Fys. Medd., vol. 29, no. CERN-55-30, p. 1, 1955.

[19] B. Singh et al. Nucl. Data Sheets, vol. 97, p. 241, 2002.

[20] R. Firestone et al., The 8th edition of the Table of Isotopes. Springer, 1997.

[21] K. Zuber, Neutrino Physics. CRC Press, 2020.

[22] M. Wang et al. Chinese Physics C, vol. 45, no. 3, 2021.

[23] B. Singh et al. Nucl. Data Sheets, vol. 84, no. 3, p. 487, 1998.

[24] B. Singh et al. Nucl. Data Sheets, vol. 84, p. 487, 1998.

[25] F. G. Kondev and S. Lalkovski Nucl. Data Sheets, vol. 112, p. 707, 2011.

[26] J. Chen and F. G. Kondev Nucl. Data Sheets, vol. 126, p. 373, 2015.

[27] F. G. Kondev Nucl. Data Sheets, vol. 109, p. 1527, 2008.

[28] G. F. Knoll, *Radiation Detection and Measurement*. John Wiley & Sons, 2010.

[29] A. Beriso Energy, vol. 77, 2019.

[30] J. L. Dobson. PhD thesis, University of Liverpool, 2005.

[31] H. Wollersheim Il Nuovo Cimento A, vol. 111, no. 6-7, p. 691, 1998.

[32] J. Blomqvist et al. Nucl. Phys. A, vol. 554, no. 1, p. 45, 1993.

[33] R. Broda et al. Eur. Phys. J. A, vol. 20, no. 1, p. 145, 2003.

[34] H. Grawe et al. Rep. Prog. Phys., vol. 70, p. 1525, 2007.

[35] P. Möller et al. Phys. Rev. C, vol. 67, no. 5, p. 055802, 2003.

[36] D. L. Fang et al. Phys. Rev. C, vol. 88, no. 3, p. 034304, 2013.

[37] N. Nishimura et al. Phys. Lett. B, vol. 756, p. 273, 2016.

[38] R. Caballero-Folch et al. Phys. Rev. Lett., vol. 117, p. 012501, 2016.

[39] A. I. Morales et al. Phys. Rev. Lett., vol. 113, p. 022702, 2014.

[40] E. M. Ney et al. Phys. Rev. C, vol. 102, p. 034326, 2020.

[41] H. Koura et al. Progr. Theor. Phys., vol. 113, no. 2, p. 305, 2005.

[42] I. N. Borzov Nucl. Phys. A, vol. 777, p. 645, 2006.

[43] T. Suzuki et al. Phys. Rev. C, vol. 85, no. 1, p. 015802, 2012.

[44] Q. Zhi et al. Phys. Rev. C, vol. 87, no. 2, p. 025803, 2013.

[45] T. Marketin et al. Phys. Rev. C, vol. 93, no. 2, p. 025805, 2016.

[46] V. Rahkonen and T. Lonnroth Z. Phys. A., vol. 322, p. 333, 1985.

[47] E. W. A. Lingeman. PhD thesis, Univ. Amsterdam, 1975.

[48] M. Benedikt et al., "The PS complex produces the nominal LHC beam," tech. rep., 2000.

[49] M. J. G. Borge and B. Jonson J. Phys. G: Nuclear and Particle Physics, vol. 44, no. 4, p. 044011, 2017.

[50] R. Bailey (Geneva), CERN, CERN, 2013.

[51] N. E. Rev. Acc. Sci. Tech., vol. 6, p. 237, 2013.

[52] M. J. G. Borge in EPJ Web of Conferences, vol. 117, p. 10002, EDP Sciences, 2016.

[53] R. J. Carroll et al. Phys. Rev. Lett., vol. 125, p. 192501, 2020.

[54] I. Bergstrom et al. Z. Phys., vol. A287, p. 219, 1978.

[55] T. Yamazaki Phys. Rev. C, vol. 1, p. 290, 1970.

[56] A. R. Poletti et al. Nucl. Phys. A, vol. 615, no. 1, p. 95, 1997.

[57] Y. Tall et al. Inter. Conf. on Nucl. Data for Sci. and Tech. 2007, 2008.

[58] L. Zanini et al. Nucl. Data Sheets, vol. 119, p. 292, 2014.

[59] G. Duchêne et al. Nucl. Instr. and Meth. in Phys. Res. Sec. A, vol. 432, no. 1, p. 90, 1999.

[60] C. E. Svensson, P. Amaudruz, et al. J. Phys. G, vol. 31, no. 10, p. S1663, 2005.

[61] I. Lazarus et al. IEEE Transactions on Nuclear Science, vol. 48, no. 3, p. 567, 2001.

[62] P. Rahkila Nucl. Instr. Meth. Phys. Res. A, vol. 595, no. 3, p. 637, 2008.

[63] T. A. Berry. PhD thesis, Univ. of Surrey, 2019.

[64] C. R. Alvarez Nucl. Phys. News, vol. 3, no. 3, p. 10, 1993.

[65] M. J. Martin Nucl. Data Sheets, vol. 114, no. 11, p. 1497, 2013.

[66] Z. Kis and B. Fazekas Nuclear Instruments and Methods in Physics Research Section A: Accelerators, Spectrometers, Detectors and Associated Equipment, vol. 418, no. 2-3, pp. 374–386, 1998.

[67] G. R. Gilmore Practical γ-ray spectrometry. John Wiley & Sons Ltd, Chichester, p. 361, 2008.

[68] B. S. Dzhelepov et al. in Program and Theses, 33rd Ann. Conf. Nucl. Spectrosc. Struct. At. Nuclei, p. 152, 1983.

[69] T. Kibédi, T. Burrows, et al. Nucl. Instr. and Meth. in Phys. Res. Sec. A, vol. 589, no. 2, p. 202, 2008.

[70] M. Brunet et al. J. Phys. Conf. Ser., vol. 1643, p. 012116, 2020.

[71] O. Dragoun et al. Czech. J. Phys., vol. B32, p. 711, 1982.

[72] O. Dragoun et al. Nucl. Phys. A, vol. 391, no. 1, p. 29, 1982.

[73] W. J. Treytl, E. K. Hyde, and T. Yamazaki Nucl. Phys. A, vol. 117, no. 3, p. 481, 1968.

[74] B. A. Brown and W. D. M. Rae Nucl. Data Sheets, vol. 120, p. 115, 2014.

[75] N. A. F. M. Poppelier and P. W. M. Glaudemans Z. Phys. A, Atomic Nuclei, vol. 329, p. 275, 1988.

[76] E. K. Warburton and B. A. Brown Phys. Rev. C, vol. 43, p. 602, 1991.

[77] W. G. Love, *The (p, n) Reaction and the Nucleon-Nucleon Force*. Plenum, New York, 1980.

[78] G. Bertsch et al. Nucl. Phys. A, vol. 284, no. 3, p. 399, 1977.

[79] B. A. Brown Phys. Rev. C, vol. 58, no. 1, p. 220, 1998.

[80] G. Astner et al. Nucl. Phys. A, vol. 182, no. 1, p. 219, 1972.

[81] M. Emeric and A. Sonzogni, "The isolde facility," 2021.

[82] J. C. Hardy et al. Phys. Lett. B, vol. 71, p. 307, 1977.

[83] H. C. Scraggs et al. Nucl. Instr. and Meth. in Phys. Res. Sec. A, vol. 543, no. 2-3, p. 431, 2005.

[84] F. G. Kondev Nucl. Data Sheets, vol. 105, p. 1, 2005.

[85] C. J. Chiara and F. G. Kondev Nucl. Data Sheets, vol. 111, p. 141, 2010.

[86] F. G. Kondev Nucl. Data Sheets, vol. 166, p. 1, 2020.

[87] M. Shamsuzzoha Basunia Nucl. Data Sheets, vol. 121, p. 561, 2014.

[88] B. Singh et al. Nucl. Data Sheets, vol. 114, p. 661, 2013.

[89] T. Vylov et al. Izv. Akad. Nauk, vol. SSSR, pp. Ser.Fiz. 38, 701 *[Engl. transl.: Bull. Acad. Sci. USSR, Phys. Ser.* ***38*** *no. 4, 31 (1974)*], 1974.

[90] C. M. Baglin Nucl. Data Sheets, vol. 113, p. 1871, 2012.

[91] B. Singh Nucl. Data Sheets, vol. 107, p. 1531, 2006.

[92] H. Xiaolong Nucl. Data Sheets, vol. 108, p. 1093, 2007.

[93] H. Xiaolong and K. Mengxiao Nucl. Data Sheets, vol. 133, p. 221, 2016.

[94] F. G. Kondev and S. Lalkovski Nucl. Data Sheets, vol. 108, p. 1471, 2007.

[95] S. Zhu and F. G. Kondev Nucl. Data Sheets, vol. 109, p. 699, 2008.

[96] A. Astier et al. Eur. Phys. J. A, vol. 46, no. 2, p. 165, 2010.

[97] A. Astier et al. Phys. Rev. Lett., vol. 104, p. 042701, 2010.

[98] C. Ellegaard et al. Nucl. Phys. A, vol. 206, no. 1, p. 83, 1973.

[99] C. Ellegaard et al. Nucl. Phys. A, vol. 162, no. 1, p. 1, 1971.

[100] I. Hamamoto Nucl. Phys. A, vol. 155, no. 2, p. 362, 1970.

[101] I. Hamamoto Physics Reports, vol. 10, no. 2, p. 63, 1974.

[102] P. Kleinheinz Progress in Particle and Nucl. Phys., vol. 28, p. 369, 1992.

[103] B. A. Brown Phys. Rev. Lett., vol. 85, no. 25, p. 5300, 2000.

[104] C. Ellegaard et al. Nucl. Phys. A, vol. 162, no. 1, p. 1, 1971.

Appendix A

^{208}Po Transitions Table

Table A.1: Full list of levels and transitions observed in ^{208}Po in this analysis. New and (re)assigned transitions/levels are shown in bold. $E_{i/f}$ and $J^{\pi}_{i/f}$ are energies and spin-parities of initial and final states. E_γ is the measured energy of the transition. Multipolarities based on previous conversion electron coefficient measurements are indicated. When spin-parities are not firmly established from experimental considerations, the assignment favoured by shell model calculations is shown in bold. References to Nucl. Data Sheet compilations (ref. [3]) are provided for the spin-parities of states which have been observed in non-beta-decay studies. For instances where levels have only been observed previously in beta-decay studies, all information relevant to their spin-parity assignments is provided in this table. The relative intensity of each γ ray ($I_\gamma, rel.$ and $I_\gamma + IC, rel.$) are given both with and without internal electron conversion, with respect to 100 for the combined intensities of γs to the ground state (with IC). log*ft* values were calculated using the measured transition intensity imbalances. The last column contains additional information needed for the spin-parity assignments.

E_i/keV	J_i^π	E_f/keV	J_f^π	E_γ/keV	σL	$I_{\gamma,rel.}$	$I_{\gamma+IC,rel.}$	log*ft*	Comment
686.6(2)	2^+[3]	0.0	0^+	686.6(2)	E2[3]	98(10)	100(10)	-	-
1263.2(3)	2^+[3]	686.6(2)	2^+	576.7(3)	M1(+E2)[3]	0.35(9)	0.38(9)	-	-
		0.0	0^+	1263.0(2)	E2[3]	0.15(1)	0.15(1)		
1346.7(3)	4^+[3]	686.6(2)	2^+	660.1(2)	E2[3]	92(8)	93(8)	-	-
1420.3(3)	3^+[3]	686.6(2)	2^+	733.7(3)	M1+E2[3]	1.4(3)	1.4(3)	-	-
1524.4(3)	6^+[3]	1346.7(3)	4^+	177.7(2)	E2[3]	50(3)	87(4)	-	-
1528.3(5)	8^+[3]	1524.4(3)	6^+	3.9(4)$^{a)}$	E2[71, 72]	-	40(2)$^{a)}$	-	-
1583.4(3)	4^+[3]	1420.3(3)	3^+	163.3(3)	-	0.16(4)	0.46(21)	-	-
		1346.7(3)	4^+	236.8(2)	M1(+E2)[3]	0.35(5)	0.69(10)		
		686.6(2)	2^+	896.6(2)	E2[3]	4.8(2)	4.8(2)		
1995.2(4)	3^-	1420.3(3)	3^+	575.3(3)	-	0.40(7)	0.41(8)	-	Populated from 3554 and 3610 keV 5^- states
		686.6(2)	2^+	1308.2(2)	E1(+M2)[3]	0.22(1)	0.22(1)		
2041.6(4)	6^+[3]	1524.4(3)	6^+	517.2(2)	M1(+E2)[3]	6.3(4)	7.0(4)	3.8(12) 7.75(1)	Populated by M1[3] 294 keV transition from 2336 keV 7^+ state
		1346.7(3)	4^+	^{z}694.8(3)	-	2.5(4)	2.5(4)		
2149.1(4)	3^+, $\mathbf{4^+}$	1583.4(3)	4^+	566.1(2)	M1+E2[3]	0.75(3)	0.80(4)	See text	-
		1420.3(3)	3^+	^{z}729.2(3)	-	0.38(6)	0.39(6)		
		1346.7(3)	4^+	802.6(2)	-	0.40(6)	0.42(6)		
		686.6(2)	2^+	^{x}1461.5(3)	-	0.57(5)	0.57(5)		
2160.3(5)	8^+[3]	1528.3(5)	8^+	631.9(2)	M1(+E2)[3]	3.7(4)	3.9(4)	See text	-
2222.6(4)	8^+	2160.3(5)	8^+	^{x}62.3(9)$^{a)}$	-	-	0.45(34)$^{a)}$	-	See text
		1528.3(5)	8^+	^{z}694.3(2)	M1*	1.9(2)	2.0(2)		

Table A.1 – *Continued.*

E_i/keV	J_i^π	E_f/keV	J_f^π	$E_{\gamma/keV}$	σL	$I_{\gamma,rel.}$	$I_{\gamma+IC,rel.}$	log*ft*	Comment
		1524.4(3)	6^+	^{z}698.2(2)	E2[3]	1.24(7)	1.27(9)		
2280.8(3)	5^+	1346.7(3)	4^+	934.1(2)	M1+E2[3]	0.95(6)	0.97(6)	0.86(13) 8.32(7)	Populated from 3113 keV $5^-,6^-$ state, J^π values limited by β^+ population
2293.8(4)	6^+[3]	2041.6(4)	6^+	252.5(2)	-	0.62(6)	0.93(24)	4.13(57) 7.63(6)	-
		1583.4(3)	4^+	710.5(2)	-	0.65(2)	0.66(2)		
		1528.3(5)	8^+	765.2(3)	-	0.13(7)	0.14(7)		
		1524.4(3)	6^+	769.5(2)	M1(+E2)[3]	2.1(2)	2.2(2)		
		1346.7(3)	4^+	947.0(2)	E2[3]	1.60(4)	1.61(4)		
2335.7(5)	7^+[3]	2041.6(4)	6^+	294.2(2)	M1[3]	0.99(7)	1.53(11)	6.50(49) 7.42(4)	-
		1528.3(5)	8^+	807.2(2)	M1(+E2)[3]	6.2(2)	6.4(2)		
		1524.4(3)	6^+	811.4(2)	M1+E2[3]	1.22(7)	1.25(7)		
2369.3(4)	7^-[3]	1528.3(5)	8^+	840.8(4)	E1[3]	3.0(3)	3.0(3)	-	-
		1524.4(3)	6^+	845.1(2)	E1[3]	21.1(7)	21.1(7)		
2402.1(5)	$3^-,4^+$	1263.2(3)	2^+	^{y}1139.0(4)	E1,E2[3]	0.5(2)	0.5(2)	-	Populated from 3610 keV 5^- state and 3683 $5^-,6^-$ state
2415.0(5)	$\mathbf{7^+}, 8^+$	2160.3(5)	8^+	254.8(3)	-	0.32(4)	0.48(14)	-	Populated from 3565 keV 6^- state
		2041.6(4)	6^+	373.4(2)	-	0.71(4)	0.80(12)		
		1528.3(5)	8^+	886.3(2)	M1+E2[3]	2.95(9)	3.02(9)		
		1524.4(3)	6^+	^{x}890.8(3)	-	0.47(4)	0.47(4)		
2437.6(4)	5^+	1420.3(3)	3^+	^{y}1017.2(2)	E2*	0.77(6)	0.78(6)	-	See text
2507.7(3)	$5^+, \mathbf{6^+}$	2293.8(4)	6^+	214.1(3)	M1+E2[3]	0.28(5)	0.59(12)	5.91(20) 7.39(2)	-
		1583.4(3)	4^+	^{z}924.2(2)	-	0.57(5)	0.58(6)		
		1524.4(3)	6^+	983.2(2)	M1+E2[3]	4.7(2)	4.7(2)		
2526.7(4)	5^+	2041.6(4)	6^+	485.0(2)	M1[3]	0.44(5)	0.50(6)	1.74(21) 7.92(6)	-
		1524.4(3)	6^+	1002.2(2)	M1(+E2)[3]	0.45(2)	0.46(2)		
		1420.3(3)	3^+	^{x}1106.9(3)	-	0.30(3)	0.30(3)		
		1346.7(3)	4^+	1179.6(2)	M1(+E2)[3]	1.05(4)	1.05(4)		
2556.5(5)	7^+[3]	2369.3(4)	7^-	^{y}188.2(2)	-	0.5(2)	0.5(2)	22.9(16) 6.8(2)	-
		2293.8(4)	6^+	262.0(3)	M1(+E2)[3]	0.38(6)	0.62(13)		
		2222.6(4)	8^+	^{z}333.9(3)	M1(+E2)[3]	2.5(5)	2.9(9)		
		2160.3(5)	8^+	396.2(3)	M1+E2[3]	1.16(2)	1.41(4)		
		1528.3(5)	8^+	1027.7(2)	M1+E2[3]	19.4(7)	19.7(7)		
2574.8(4)	$\mathbf{6^-}, 7^-$[3]	2369.3(4)	7^-	205.5(2)	M1(+E2)[3]	7.9(4)	19.4(9)	-	-
		1524.4(3)	6^+	^{x}1050.3(2)	-	0.26(3)	0.26(3)		
2863.0(4)	$3^-,4,5,6^+$	2402.1(5)	$3^-,4^+$	^{x}460.9(3)	-	0.23(7)	0.24(8)	-	Populated from 3553 and 3610 keV 5^- states
		1583.4(3)	4^+	^{y}1279.62(2)	-	0.87(7)	0.87(7)		
2884.5(3)	5^-	1583.4(3)	4^+	^{z}1301.2(3)	-	0.12(3)	0.12(3)	-	-
		1524.4(3)	6^+	1360.0(2)	E1[3]	0.99(1)	0.99(1)		
		1346.7(3)	4^+	1537.6(2)	E1[3]	1.52(5)	1.52(5)		

Table A.1 – *Continued.*

E_i/keV	J_i^π	E_f/keV	J_f^π	$E_{\gamma/keV}$	σL	$I_{\gamma,rel.}$	$I_{\gamma+IC,rel.}$	log*ft*	Comment
2926.6(4)	5^-	2574.8(4)	$6^-,7^-$	^{x}351.7(4)	-	0.31(7)	0.35(11)	0.62(47) 8.2(4)	M1+E2 [3] (638 keV) transition from 3565 keV 6^- state
		1583.4(3)	4^+	1343.4(2)	E1[3]	2.46(8)	2.46(8)		
		1346.7(3)	4^+	^{x}1579.9(4)	-	0.4(2)	0.4(2)		
3024.2(5)	$6^+,7,8^-$	2222.6(4)	8^+	^{x}801.6(3)	-	0.48(8)	0.48(9)	0.91(13) 8.0(2)	J^π values limited by β^+ population
		2160.3(5)	8^+	^{y}863.8(2)	-	0.42(4)	0.42(4)		
3072.5(4)	$6^-,7^-,8^-$	2041.6(4)	6^+	^{x}1030.9(3)	-	0.32(5)	0.32(5)	-	M1(+E2)[3] transition from 4167 keV 7^- state
3103.8(4)	$4^-,5,6,7,8^-$	2041.6(4)	6^+	^{y}1062.2(3)	-	0.10(3)	0.10(3)	0.10(3) 8.9(2)	J^π values limited by β^+ population
3113.3(5)	$5^-,6^-$	2574.8(4)	$6^-,7^-$	538.6(3)	M1+E2[3]	0.30(7)	0.32(7)	-	-
		2369.3(4)	7^-	^{x}744.0(3)	-	0.26(7)	0.27(7)		
		2280.8(3)	5^+	^{z}832.6(7)	-	0.06(6)	0.06(6)		
		2041.6(4)	6^+	1071.4(3)	-	0.25(4)	0.25(4)		
		1524.4(3)	6^+	1588.8(2)	-	0.24(1)	0.24(1)		
3163.7(5)	$4^-,5^-,6^-$	2574.8(4)	$6^-,7^-$	^{x}588.9(4)	-	0.6(2)	0.6(2)	-	M1(+E2)[3] from 3554 keV 5^- state
		1583.4(3)	4^+	^{y}1580.3(4)	-	0.31(8)	0.31(8)		
3276.0(5)	$4^-,5,6,7^-$	2884.5(3)	5^-	^{x}391.6(3)	-	0.14(4)	0.16(5)	-	See text
		2149.1(4)	$3^+,4^+$	^{x}1126.2(5)	-	0.24(8)	0.24(8)		
		1583.4(3)	4^+	^{y}1692.8(3)	-	0.32(5)	0.32(5)		
		1346.7(3)	4^+	^{y}1929.8(4)	-	0.20(4)	0.20(4)		
3441.8(5)	$4^-,5^-,6^+$	2926.6(4)	5^-	^{x}515.5(4)	-	0.33(5)	0.35(7)	0.65(9) 7.9(7)	J^π values limited by β^+ population
		1346.7(3)	4^+	^{z}2094.8(2)	E1,E2[3]	0.30(4)	0.30(4)		
3533.6(4)	$5^-,6^-,7^-$	2926.6(4)	5^-	^{x}606.7(3)	-	0.12(3)	0.12(3)	1.39(20) 7.52(7)	-
		2884.5(3)	5^-	^{x}649.4(3)	-	0.17(3)	0.18(4)		
		2574.8(4)	$6^-,7^-$	^{y}958.9(2)	M1(+E2)[3]	0.71(8)	0.73(9)		
		2369.3(4)	7^-	^{y}1164.2(3)	-	0.37(6)	0.37(6)		
3553.9(4)	5^-	3276.0(5)	$4^-,5,6,7^-$	^{x}278.5(4)	-	0.15(7)	0.19(11)	5.31(60) 6.94(6)	-
		3163.7(5)	$4^-,5^-,6^-$	^{z}390.3(2)	M1(+E2)[3]	0.48(9)	0.53(13)		
		2926.6(4)	5^-	627.1(2)	M1(+E2)[3]	0.29(4)	0.31(4)		
		2884.5(3)	5^-	669.5(2)	M1(+E2)[3]	1.32(3)	1.38(5)		
		2863.0(4)	$3^-,4,5,6^+$	^{x}691.2(1)	-	0.34(2)	0.34(3)		
		2149.1(4)	$3^+,4^+$	^{x}1404.6(4)	-	0.24(6)	0.24(6)		
		2041.6(4)	6^+	^{z}1512.4(3)	E1[3]	0.24(3)	0.24(3)		
		1995.2(4)	3^-	^{x}1558.2(5)	-	0.3(2)	0.3(2)		
		1583.4(3)	4^+	1970.3(2)	-	0.12(1)	0.12(1)		
		1524.4(3)	6^+	2029.4(2)	E1[3]	1.30(6)	1.30(6)		
		1346.7(3)	4^+	2207.0(2)	E1[3]	0.41(3)	0.41(3)		
3564.8(4)	6^-	3276.0(5)	$4^-,5,6,7^-$	^{x}289.6(10)	-	0.1(1)	0.1(1)	25.9(15) 6.24(1)	-
		3113.3(5)	$5^-,6^-$	451.7(4)	M1(+E2)[3]	0.6(3)	0.7(3)		
		2926.6(4)	5^-	^{z}638.1(2)	M1+E2[3]	0.34(4)	0.35(5)		
		2574.8(4)	$6^-,7^-$	990.0(2)	M1(+E2)[3]	16.3(5)	16.6(5)		
		2556.5(5)	7^+	1008.6(2)	E1[3]	1.92(6)	1.92(6)		
		2526.7(4)	5^+	1038.1(3)	(E1+M2)[3]	0.52(3)	0.52(3)		
		2437.6(4)	5^+	^{z}1126.9(4)	E1*	0.12(5)	0.12(5)		
		2415.0(5)	$7^+,8^+$	^{x}1149.5(3)	-	1.2(3)	1.2(3)		
		2369.3(4)	7^-	1195.2(2)	M1+E2[3]	1.86(4)	1.86(4)		

Table A.1 – *Continued.*

E_i/keV	J_i^π	E_f/keV	J_f^π	$E_{\gamma/keV}$	σL	$I_{\gamma,rel.}$	$I_{\gamma+IC,rel.}$	log*ft*	Comment
		2335.7(5)	7^+	1229.1(2)	E1[3]	2.5(2)	2.5(2)		
		2041.6(4)	6^+	1523.5(3)	-	0.07(2)	0.07(2)		
3610.1(4)	5^-	3276.0(5)	$4^-,5,6,7^-$	^{x}334.1(7)	-	0.2(2)	0.3(2)	3.28(43) 7.10(6)	-
		2863.0(4)	$3^-,4,5,6^+$	^{y}747.4(1)	-	0.62(6)	0.63(7)		
		2402.1(5)	$3^-,4^+$	^{x}1208.3(2)	-	0.21(3)	0.21(3)		
		2149.1(4)	$3^+,4^+$	^{x}1460.6(2)	-	0.70(6)	0.70(6)		
		1995.2(4)	3^-	^{x}1614.4(3)	-	0.37(9)	0.37(9)		
		1583.4(3)	4^+	^{y}2026.7(2)	E1*	0.61(4)	0.61(4)		
		1524.4(3)	6^+	^{y}2085.9(2)	E1[3]	0.55(4)	0.55(4)		
3682.6(4)	$5^-,6^-$	3276.0(5)	$4^-,5,6,7^-$	^{x}406.5(3)	-	0.4(2)	0.5(2)	4.46(64) 6.91(7)	-
		3163.7(5)	$4^-,5^-,6^-$	^{x}518.9(4)	-	0.4(2)	0.5(2)		
		2926.6(4)	5^-	755.5(2)	M1(+E2)[3]	1.30(2)	1.35(2)		
		2884.5(3)	5^-	798.2(2)	M1(+E2)[3]	0.75(6)	0.78(6)		
		2863.0(4)	$3^-,4,5,6^+$	^{x}820.0(4)	-	0.15(4)	0.15(4)		
		2574.8(4)	$6^-,7^-$	1107.9(3)	M1+E2[3]	0.54(8)	0.54(8)		
		2402.1(5)	$3^-,4^+$	^{z}1281.7(3)	-	0.19(3)	0.19(3)		
		2041.6(4)	6^+	1640.6(5)	E1[3]	0.12(4)	0.12(4)		
		1524.4(3)	6^+	2157.8(6)	-	0.14(5)	0.14(5)		
		1346.7(3)	4^+	2336.0(3)	-	0.38(4)	0.38(4)		
3708.0(5)	$5^-,6^-,7^-,8^-$	2574.8(4)	$6^-,7^-$	^{y}1133.2(4)	M1+E2[3]	0.36(10)	0.36(10)	0.36(10) 8.0(2)	-
3744.5(5)	$5^-,6,7,8^-$	2160.3(5)	8^+	^{z}1584.2(2)	-	0.07(1)	0.07(1)	0.07(1) 8.67(7)	J^π values limited by β^+ population
3808.4(4)	$6^-,7^-$	2574.8(4)	$6^-,7^-$	1233.9(3)	-	0.42(6)	0.42(6)	1.80(16) 7.21(5)	J^π values limited by β^+ population and logft
		2369.3(4)	7^-	1438.9(2)	M1+E2[3]	1.26(7)	1.26(7)		
		2335.7(5)	7^+	1472.7(6)	-	0.03(2)	0.03(2)		
		1524.4(3)	6^+	2283.8(3)	-	0.10(2)	0.10(2)		
3893.9(4)	$4^-,5,6,7^-$	2926.6(4)	5^-	^{x}967.0(4)	-	0.03(2)	0.03(2)	0.79(16) 7.5(1)	J^π values limited by β^+ population
		2437.6(4)	5^+	^{y}1456.3(4)	-	0.4(2)	0.4(2)		
		2280.8(3)	5^+	^{y}1613.2(3)	-	0.03(1)	0.03(1)		
		1524.4(3)	6^+	^{y}2369.8(2)	-	0.36(2)	0.36(2)		
3904.3(6)	$4^-,5,6,7,8^-$	2556.5(5)	7^+	^{x}1346.7(2)	-	0.28(2)	0.28(2)	0.37(12) 7.8(2)	-
		2437.6(4)	5^+	^{y}1467.9(10)	-	0.08(4)	0.08(4)		
4018.9(5)	$5,6,7$	3113.3(5)	$5^-,6^-$	^{x}905.2(4)	-	0.5(3)	0.6(3)	1.35(28) 7.17(9)	J^π values limited by β^+ population and logft
		2526.7(4)	5^+	^{x}1492.8(8)	-	0.05(4)	0.05(4)		
		2293.8(4)	6^+	1725.0(2)	-	0.02(1)	0.02(1)		
		1524.4(3)	6^+	2494.6(2)	-	0.73(3)	0.73(3)		
4046.8(5)	$4^-,5,6,7,8^-$	2335.7(5)	7^+	^{x}1710.8(4)	-	0.03(1)	0.03(1)	0.15(4) 8.1(2)	J^π values limited by β^+ population
		1524.4(3)	6^+	^{y}2522.8(4)	-	0.12(3)	0.12(3)		
4079.4(4)	$5,6,7$	2574.8(4)	$6^-,7^-$	^{x}1504.8(3)	-	0.35(6)	0.35(6)	0.64(10) 7.41(8)	J^π values limited by β^+ population and logft
		2280.8(3)	5^+	^{x}1798.3(4)	-	0.02(1)	0.02(1)		
		2041.6(4)	6^+	^{y}2037.8(2)	-	0.15(1)	0.15(1)		
		1524.4(3)	6^+	^{y}2555.2(4)	-	0.12(2)	0.12(2)		

Table A.1 – *Continued.*

E_i/keV	J_i^π	E_f/keV	J_f^π	$E_{\gamma/keV}$	σL	$I_{\gamma,rel.}$	$I_{\gamma+IC,rel.}$	log*ft*	Comment
4143.2(5)	$5,6,7$	2415.0(5)	$7^+,8^+$	^{x}1728.0(3)	-	1.8(3)	1.8(3)	2.38(33) 6.77(7)	J^π values limited by β^+ population and logft
		2369.3(4)	7^-	^{y}1773.5(3)	-	0.34(4)	0.34(4)		
		2335.7(5)	7^+	^{x}1807.9(4)	-	0.03(1)	0.03(1)		
		2041.6(4)	6^+	^{y}2101.3(3)	-	0.04(1)	0.04(1)		
		1524.4(3)	6^+	^{y}2619.3(4)	-	0.21(3)	0.21(3)		
4166.6(5)	7^-	3072.5(4)	$6^-,7^-,8^-$	^{y}1094.4(3)	M1(+E2)[3]	0.32(5)	0.32(5)	5.43(81) 6.39(8)	-
		2415.0(5)	$7^+,8^+$	1751.7(4)	E1[3]	1.5(5)	1.5(5)		
		2369.3(4)	7^-	1796.9(2)	M1(+E2)[3]	0.69(1)	0.69(1)		
		2335.7(5)	7^+	1830.4(4)	-	0.03(1)	0.03(1)		
		2293.8(4)	6^+	1872.6(3)	E1[3]	0.19(3)	0.19(3)		
		2222.6(4)	8^+	^{y}1944.1(3)	-	0.12(3)	0.12(3)		
		2041.6(4)	6^+	2125.1(3)	E1[3]	0.46(5)	0.46(5)		
		1528.3(5)	8^+	2638.5(3)	-	1.70(9)	1.70(9)		
		1524.4(3)	6^+	2642.4(5)	-	0.47(4)	0.47(4)		
4187.2(4)	$4^-,5,6,7,8^-$	1524.4(3)	6^+	^{y}2662.7(3)	-	0.04(1)	0.04(1)	0.04(1) 8.5(2)	J^π values limited by β^+ population
4196.0(7)	$5^-,6,7,8^-$	1528.3(5)	8^+	^{z}2667.7(5)	-	0.04(1)	0.04(1)	0.04(1) 8.5(2)	J^π values limited by β^+ population
4209.1(4)	$5^+,6^+,7^+$	2437.6(4)	5^+	^{x}1772.5(4)	-	0.10(2)	0.10(2)	0.31(4) 7.58(7)	J^π values limited by β^+ population
		2041.6(4)	6^+	^{y}2168.2(2)	E2,M1[3]	0.21(1)	0.21(1)		
4251(1)	$4^-,5,6,7,8^-$	2574.8(4)	$6^-,7^-$	^{x}1675.8(5)	-	0.15(6)	0.15(6)	0.19(8) 7.7(2)	J^π values limited by β^+ population
		2335.7(5)	7^+	1916.8(3)	-	0.04(2)	0.04(2)		
4257.1(4)	$4^-,5,6,7,8^-$	1524.4(3)	6^+	^{y}2732.7(3)	-	0.09(1)	0.09(1)	0.09(1) 8.05(6)	J^π values limited by β^+ population
4426.9(6)	$5,6,7,8^-$	2369.3(4)	7^-	^{x}2057.4(6)	-	0.03(1)	0.03(1)	0.07(3) 7.9(2)	J^π values limited by β^+ population
		2335.7(5)	7^+	^{z}2091.3(6)	-	0.01(1)	0.01(1)		
		1524.4(3)	6^+	^{y}2902.6(4)	-	0.03(1)	0.03(1)		
4468.3(7)	$4^-,5,6,7,8^-$	2437.6(4)	5^+	^{x}2030.8(6)	-	0.10(5)	0.10(5)	0.10(5) 7.7(3)	J^π values limited by β^+ population
4508.2(5)	$4^-,5,6,7$	2926.6(4)	5^-	^{y}1581.5(4)	-	0.08(2)	0.08(2)	0.08(2) 7.7(2)	J^π values limited by β^+ population
4524.9(6)	$4^-,5,6,7,8^-$	1524.4(3)	6^+	^{y}3000.5(5)	-	0.03(1)	0.03(1)	0.03(1) 8.1(2)	J^π values limited by β^+ population

$^{a)}$ This low energy γ ray was not observed directly. Its energy and intensity were determined from coincidence relationships.

^{x} The gamma ray has been newly identified from this analysis.

^{y} The gamma ray was observed in previous decay studies [3], and has been placed into the level scheme in this analysis.

^{z} The gamma ray has been reassigned from its position in prior analysis [3].

* Measured conversion coefficient was taken from ref. [3], however the multipolarity was reinterpreted in this analysis.

Appendix B

Table of Branching Ratios

Table B.1: Comparison between experimental and shell model γ-ray branching ratios. Only transitions with experimental or theoretical $\mathrm{BR}_\gamma > 1\%$. are shown. In some cases no firm experimental spin-parity assignments could be achieved, as shown in Table I. When the proposed spin-parity is based on comparison with theory, as shown in the present table, these are preceded by the star symbol.

	Experiment			Shell Model	
E_i (keV) / J_i^π	E_f (keV)/ J_f^π	BR_γ (%)	E_i (keV)	E_f (keV)	BR_γ (%)
687 / 2^+	0	100	723	0	100
1263 / 2^+	687 / 2^+	70	1226	723	30
	0 / 0^+	30		0	70
1347 / 4^+	687 / 2^+	100	1365	723	100
1420 / 3^+	1263 / 2^+	-	1396	1226	1
	687 / 2^+	100		723	99
1524 / 6^+	1347 / 4^+	100	1497	1365	100
1528 / 8^+	1524 / 6^+	100	1490	-	-a)
1583 / 4^+	1420 / 3^+	3	1648	1396	13
	1347 / 4^+	7		1365	4
	687 / 2^+	90		723	83
2042 / 6^+	1524 / 6^+	72	2045	1497	61
	1347 / 4^+	28		1365	38
2149 / *4^+	1583 / 4^+	36	2117	1648	26
	1420 / 3^+	18		1396	59
	1347 / 4^+	19		1365	8
	687 / 2^+	27		723	7
2160 / 8^+	1528 / 8^+	100	2109	1490	99
	1524 / 6^+	-		1497	1
2223 / 8^+	2160 / 8^+	$\sim$1	2149	2109	1
	1524 / 6^+	39		1497	70
	1528 / 8^+	61		1490	29
2281 / 5^+	2042 / 6^+	-	2282	2045	6
	1583 / 4^+	-		1648	3
	1524 / 6^+	-		1497	15
	1347 / 4^+	100		1365	75
2294 / 6^+	2042 / 6^+	12	2283	2045	11
	1583 / 4^+	13		1648	10
	1524 / 6^+	41		1497	38

Table B.1 – *Continued.*

	Experiment		Shell Model		
E_i (keV) / J_i^π	E_f (keV)/ J_f^π	BR$_\gamma$ (%)	E_i (keV)	E_f (keV)	BR$_\gamma$ (%)
	1528 / 8^+	3		1490	1
	1347 / 4^+	31		1365	41
2336 / 7^+	2160 / 8^+	-	2314	2109	1
	2042 / 6^+	12		2045	14
	1524 / 6^+	15		1497	21
	1528 / 8^+	74		1490	64
2369 / 7^-	1528 / 8^+	12	2357	1490	0.3
	1524 / 6^+	88		1497	100
2415 / $*7^+$	2223 / 8^+	-	2387	2149	4
	2160 / $*8^+$	7		2109	6
	2042 / 6^+	16		2045	4
	1524 / 6^+	11		1497	7
	1528 / 8^+	66		1490	79
2438 / 5^+	2042 / 6^+	-	2401	2045	2
	1583 / 4^+	-		1648	3
	1524 / 6^+	-		1497	29
	1420 / 3^+	100		1396	61
	1347 / 4^+	-		1365	3
2508 / $*6^+$	2415 / $*7^+$	-	2485	2387	1
	2336 / 7^+	-		2314	1
	2294 / 6^+	5		2283	7
	2281 / $*5^+$	-		2282	1
	2042 / 6^+	-		2045	3
	1583 / 4^+	10		1648	2
	1524 / 6^+	85		1497	83
	1528 / 8^+	-		1490	1
2527 / 5^+	2294 / 6^+	-	2572	2283	5
	2281 / $*5^+$	-		2282	5
	2149 / $*4^+$	-		2117	9
	2042 / 6^+	20		2045	23
	- / 4^+	-		2005	4
	1583 / 4^+	-		1648	8
	1524 / 6^+	20		1497	30
	1420 / 3^+	13		1396	2
	1347 / 4^+	47		1365	13
2556 / 7^+	2369 / 7^-	2	2732[b]	2357	<1
	2336 / 7^+	-		2314	4
	2294 / 6^+	2		2283	<1
	2223 / 8^+	10		2149	45
	2160 / $*8^+$	5		2109	3
	2042 / 6^+	-		2045	11
	1524 / 6^+	-		1497	5
	1528 / 8^+	81		1490	32
2575 / $*6^-$	2369 / 7^-	97	2553	2357	100
	1524 / 6^+	3		1497	<1

[a] Due to the inversion of the 6^+ and 8^+ states, no branching ratio could be calculated, however the theoretical B(E2) value (~1 W.u.) indicates the existence of a transition between the two states.

[b] There is a 7^+ state predicted at 2618 keV, which is closer to the experimental value. However its decay pattern is very different from that observed experimentally.

Appendix C

List of Publications & Conference Talks

Publications

B. García *et al.*
Half-life measurements in ^{164}*Dy,* ^{166}*Dy using* γ*-* γ *fast-timing spectroscopy with the* ν*-Ball spectrometer*
Phys. Rev. C, **101**, 2, 2020, APS

R. L. Canavan *et al.*
Half-life measurements in ^{164,166}*Dy using* γ*-* γ *fast-timing spectroscopy with the* ν*-Ball spectrometer*
Phys. Rev. C, **101**, 2, 024313, 2020, APS

M. Rudigier *et al.*
Isomer spectroscopy and sub-nanosecond half-live determination in ^{178}*W using the NuBall array*
Acta Physica Polonica B, **50**, 3, 661–667, 2019, Jagiellonian University

M. Rudigier *et al.*
Multi-quasiparticle sub-nanosecond isomers in ^{178}*W*
Phys. Lett. B, **801**, 135140, 2020, Elsevier

T. A. Berry *et al.*
Octupole states in ^{207}*Tl studied through* β *decay*
Phys. Rev. C, **101**, 5, 054311, 2020, APS

L. Morrison *et al.*
Quadrupole deformation of ^{130}*Xe measured in a Coulomb-excitation experiment*
Phys. Rev. C, **102**, 5, 054304, 2020, APS

R. J. Carroll *et al.*
Competition between Allowed and First-Forbidden β *Decay: The Case of* ^{208}*Hg*$\rightarrow$^{208}*Tl*
Phys. Rev. Lett., **125**, 19, 192501, 2020, APS

N. Marchini *et al.*
Low-energy Coulomb Excitation of ^{94}*Zr*
IL NUOVO CIMENTO, **100**, 143, 42, 2019

P. M. Walker *et al.*
Properties of ^{187}*Ta Revealed through Isomeric Decay*
Phys. Rev. Lett., **125**, 19, 192505, 2020, APS

M. Brunet *et al.*
^{208}*Po populated through EC/*β^+ *decay*
Jour. of Phys.: Conf. Ser., **1643**, 1, 012116, 2020, IOP Publishing

R. L. Canavan *et al.*
Reaction Channel selection techniques and γ–γ *fast-timing spectroscopy using the* ν*-Ball Spectrometer*
Jour. of Phys.: Conf. Ser., **1643**, 1, 012117, 2020, IOP Publishing

L. Morrison *et al.*
Dealing with contaminants in Coulomb excitation of radioactive beams
Jour. of Phys.: Conf. Ser., **1643**, 1, 012146, 2020, IOP Publishing

Conference Talks

DESPEC Data Analysis and Event Building
NUSTAR Week 2018 (Milan)

Structure of ^{208}*Po populated through* β^+ */ EC decay*
International Nuclear Physics Conference 2019 (Glasgow)

Competition of allowed and first-forbidden β^+ */ EC decays of* ^{208}*At*
ISOLDE Workshop and Users meeting 2020